Raman Gain and Lasing from Cold Potassium Atoms in a Ring Cavity

by

Graeme John Harvie

A thesis submitted to
The University of Birmingham
for the degree of
DOCTOR OF PHILOSOPHY

Ultracold Atoms Group
School of Physics and Astronomy
College of Engineering and Physical Sciences
The University of Birmingham

January 2020

Abstract

This thesis describes an experiment with a cloud of magneto-optically trapped Potassium-39 spatially overlapped with the modes of a high-finesse ring cavity. Optical gain was observed with the system in steady state, without any beams additional to the normal cooling and repump beams in a potassium-39 magneto-optical trap. This was found to operate on a Raman gain mechanism between atomic hyperfine ground states, which has not been seen under similar conditions with other atomic species. Lasing into the cavity modes was then studied, with a particular focus on effects specific to the ring cavity geometry. This showed a directional bistability and non-reciprocity. The bistability can be described by existing theory, but the mechanism of the non-reciprocity is unknown, despite a detailed investigation. The second order coherence time of the system was explored below threshold, and demonstrates a strong dependence on gain, which may have applications in the detection of extremely small gains.

ACKNOWLEDGEMENTS

I would firstly like to thank my supervisor Jon Goldwin for his indispensable advice and expertise, for giving me the chance to work on your experiment, and for generally having an open door approach to my endless questions. Thanks also to Andreas and Rob for introducing me to the lab and teaching me how to use the experiment in my first year.

Balazs and Adam, thanks for being my co-students during my time here. I'm sure you'll both go on to generate interesting results in Sussex and Birmingham respectively. Adam, I hope the diodes live long and healthy lives, and the air-con stays nice and cold for you!

Thanks also to Carol and my (other) housemates, for your support and encouragement throughout my PhD. Without your moral support, table tennis games, and tasty meals I would have given up a long time ago!

A final thanks goes to my family for raising me so well and putting me in a position where I can take three years out to mess about with lasers. Without the loving and stable upbringing I had, I wouldn't be here, and I don't take that for granted.

CONTENTS

LIST OF FIGURES

LIST OF TABLES

LIST OF PUBLICATIONS AND CONFERENCE CONTRIBUTIONS

B. Megyeri, G Harvie, A Lampis, and J. Goldwin. Directional bistability and nonreciprocal lasing with cold atoms in a ring cavity. *Phys. Rev. Lett, 121:163003, Oct 2018*

Graeme Harvie, Adam Butcher, and Jon Goldwin. In-situ raman gain between hyperfine ground states in a potassium magneto-optical trap. *Phys. Rev. A, 100:033408*, Sep 2019

Graeme Harvie. Bistable and nonreciprocal lasing using cold potassium-39 atoms in a ring cavity. Talk delivered at *Quantum, Atomic, and Molecular Physics 2019*, Sep 2019

LIST OF ABBREVIATIONS

AOM - Acousto-optic modulator

APD - Avalanche photodiode

BOL - Beat offset lock

CCW - Counterclockwise

CW - Clockwise

ECDL - External cavity diode laser

FMS - Frequency modulation spectroscopy

FWHM - Full width at half maximum

HBTI - Hanbury Brown-Twiss interferometer

HPF - High pass filter

HWHM - Half width at half maximum

LPF - Low pass filter

MIDL - Magnetically induced dichroism lock

MOT - Magneto-optical trap

PBS - Polarising beam splitter

PDH - Pound Drever Hall

RPAOM - Repump acousto-optic modulator

SMF - Single mode fibre

SPCM - Single photon counting module

TA - Tapered amplifier

TEM - Transverse electromagnetic

VCO - Voltage controlled oscillator

CHAPTER 1

INTRODUCTION

Since the invention of lasers in 1958 by Schawlow and Townes [1], and the first construction of a laser in 1960 by Maiman [2], lasers have become ubiquitous in modern society. They are used in a wide range of applications including communications, surveying, medicine, consumer electronics and many more. The usefulness of lasers is due to their high spatial and temporal coherence when compared to classical light. Spatial coherence can be considered as the degree to which the phase of the light is predictable across the beam cross section. A highly spatially coherent light source can be focused down to a point or collimated, whereas a spatially incoherent source cannot be well focused or collimated. This property means that laser light is useful in applications that require light to be focused in a very specific area, e.g. corrective laser eye surgery, laser cutting, and optical data storage or applications where a well defined beam is required, e.g. LIDAR and bar code scanners. Temporal coherence is the degree to which the phase of light is predictable over time. This allows narrow linewidth light to be produced[1], which is crucial in spectroscopy and atomic physics. The highly coherent light produced from lasers is a consequence of the qualitative difference in the light production mechanism compared to a thermal source, such as a light bulb. If the light from a bulb were filtered such that it had similar coherence properties[2] to a laser, only about 1 part in 10^{51}

[1] However, temporal coherence and linewidth are not equivalent. For example, a mode-locked laser has a high temporal coherence but a broad linewidth

[2] Included in this factor is an extra filtering term to account for the number of photons per coherence length, which is not discussed here in order to keep the discussion non-technical.

would remain [3].

A laser has two key components[1]: A gain medium and a feedback mechanism. The feedback mechanism is typically an optical cavity. Lasing occurs when the single pass gain is higher than the loss on a round trip of the feedback mechanism. In this regime the power of the light circulating in the cavity grows exponentially until some non-linear effect reduces the gain such that the round trip gain is equal to the losses, and steady state power is achieved. Due to the frequency dependence of the gain medium and cavity reflection, in general there will be one frequency that has a higher round net trip gain than all other frequencies. In the steady state, this frequency will have a net round-trip gain of 1, and all other frequencies will have round-trip gains of less than one, meaning that only one frequency can exist in steady state, leading to the temporal coherence of the laser. This frequency will be associated with a spatial mode of the optical cavity, which has a well defined spatial profile. This spatial mode ensures that the laser emission is spatially coherent.

A huge variety of gain mediums are used in lasers, each with different benefits and applications. For example, dye lasers [4], which use an optically pumped liquid dye as a gain mechanism are typically widely tunable [5], but the dye can decompose, and the liquid state requires a technically complex laser with moving parts [6]. Semiconductor lasers, which are used in this experiment, tend to be tunable over a narrow frequency range, but are technically very simple, small, cheap, and easy to use [7]. The gain medium chosen has a large effect on the properties of the laser, so finding new, exotic gain media is a useful and productive research area [8, 9].

Optical gain in Magneto-Optical Traps (MOTs) has been a topic of interest for physicists since the early days of MOTs. In 1991, the first observations in optical gain in MOTs was reported almost simultaneously by two different groups [10, 11]. Both of these groups reported gain in a steady state MOT. Two gain features were identified: The first was based on a Mollow process [12, 13], and the second was based on a Raman transition between

[1]This explanation is for a generic, single mode laser. Due to the large variety of lasers that exist, exceptions can be found for most statements here.

different Zeeman levels in the ground state. The Raman gain feature was first used to make a laser shortly afterwards in 1992 [14]. More recent work has involved using different gain mechanisms to produce lasing [15, 16], and using the properties of cold atomic gases to produce more exotic lasers. For example, random lasing [17], superradiant lasing [18], and lasing with a bistable threshold [19] have all been observed in the past few years. Collective atomic recoil lasing has been observed in ring cavities using cold atoms [20] when the cavity is unidirectionally pumped, but missing from the literature is a bidirectional cold atom ring laser.

However, bidirectional lasers have been well studied with other gain media, from the 1970's, and show rich dynamics. For example, optical bistability [21] and a myriad of non-reciprocal effects [22] are unique to the ring cavity geometry. Ring laser gyroscopes [23] are a particularly useful application of the non-reciprocity possible in ring lasers. These are currently the best rotation detectors available, with state-of-the-art devices able to achieve sensitivities of 0.001 °/h [24], and are in widespread use in the aerospace industry. Ring cavities are able to show these properties, because they have two degenerate, spatially overlapped, travelling wave modes. This allows interaction between the two modes in a way that would not be possible with a Fabry-Perot cavity.

The unique properties of cold atoms, in particular the narrow-linewidth, coherence effects, and sensitivity to magnetic fields have the potential to affect the dynamics of the ring laser system in useful ways. For example, enhancing the sensitivity of a ring laser gyroscope could be achieved by using a gain medium with fast light, which is achievable using cold atoms [25, 26]. A bidirectional cold atom ring laser is therefore an important step to producing a new type of ring laser gyroscope with dispersion enhanced sensitivity.

1.1 Outline

This thesis describes a bidirectional ring laser created by overlapping a potassium-39 MOT with a high finesse ring cavity. The same apparatus has previously been used to study strong coupling between cold atoms and a cavity mode [27], but this thesis focuses on the interaction between the gain from the atoms and the cavity. This system was studied in detail, and novel results relating to the lasing, gain mechanism, and coupled atom-cavity system below threshold were found.

Chapter 2 describes the main experimental apparatus used for all measurements in this thesis. In particular an overview of the vacuum system, B-field coils, laser systems, and the ring cavity are given.

Chapter 3 discusses the lasing produced from overlapping a MOT with the ring cavity modes. Lasing is proven using a variety of techniques, and theory and results particular to the ring cavity geometry, namely bistability and non-reciprocity, are presented.

Chapter 4 investigates the gain mechanism responsible for the observed lasing. Theory relating to Mollow gain and hyperfine Raman gain are presented, and this is compared to experimental results. The gain is shown conclusively to be due to the hyperfine Raman gain mechanism.

Chapter 5 discusses the modification of the cavity decay rate when gain is present in the cavity mode. In particular, the second order coherence time is shown to be strongly dependent on very small changes in gain. This has potential applications in detecting small gain, without perturbing the atoms with a probe.

Chapter 6 gives an overview of the work completed, and discusses the possible avenues for further investigation.

CHAPTER 2

EXPERIMENTAL APPARATUS

This chapter will give an overview of the experimental apparatus used for all following chapters. The aim of the chapter is to provide a brief overview of the apparatus, such that the rest of the work can be understood. Only the parts of the experiment which are new will be described in detail. A detailed description of other parts of the apparatus can be found in the theses of previous PhD students. [28, 29, 30, 31, 32]

The experiment is mostly controlled by a commercial control board (National Instruments PCI-6733). This board has 8 analogue channels and 8 digital channels. The analogue channels are mostly used to set the frequency of voltage controlled oscillators (VCOs). The VCOs are used to control AOMs and beat offset locks, which control the frequency of each beam in the experiment. The digital channels are used for the switching of RF switches, coils, and triggering the oscilloscope.

The experiment can be split into roughly four parts: The MOT laser system, the probe and cavity laser system, the vacuum chamber and B-field coils, and the ring cavity and detection apparatus.

2.1 Vacuum chamber

The vacuum system has two main chambers, made of stainless steel, that are connected by a steel nipple containing a thin graphite tube. One chamber contains a 2D-MOT and a

potassium ampoule. This chamber is heated to around 60°C in order to raise the vapour pressure of the potassium. The second chamber contains a 3D-MOT and is pumped by an ion pump. The 3D-MOT chamber is at room temperature. This apparatus keeps the pressure of the 3D-MOT chamber below 10^{-8} mbar, as measured by the ion pump current. The pressure of the 2D-MOT chamber is not directly measurable, but is expected to be approximately 2 orders of magnitude higher than in the 3D-MOT chamber. The 2D-MOT is loaded from the background vapour. A push beam pushes atoms from the 2D-MOT through the graphite into the other chamber. The push beam passes through the 2D-MOT and close to the 3D-MOT, such that the 3D-MOT loads from the pushed atoms. To stop the cavity from blocking the push beam, the cavity is tilted at 45° to the optical bench. This setup allows the 3D-MOT to be in a much lower pressure than would be possible if the system was loaded directly from the background. If the pressure is high, some of the material adsorbs onto the surface of the ring cavity mirrors, which lowers their reflectively. This causes the finesse of the cavity to degrade over time. A two chamber design avoids this problem, evidenced by the cavity finesse being stable for several years. A diagram of the vacuum chamber is shown in Figure 2.1 and a photo of the vacuum chamber is shown in Figure 2.2.

The 3D-MOT operates in a standard geometry with 3 retro-reflected MOT beams with a $1/e^2$ beam diameter of 1 inch and a pair of circular coils. The 2D-MOT uses 2 retro-reflected MOT beams and 2 pairs of rectangular MOT coils, and the beams also have a $1/e^2$ diameter of 1 inch.

The 3D MOT can be imaged from two different angles. The primary way of imaging the MOT is with a AVT Pike F145B camera, which faces perpendicular to the cavity axis. This camera allows the MOT number to be measured and allows the MOT position and size to be determined along the cavity axis and the vertical direction. To allow the MOT position to be measured in the third direction, a webcam looks vertically down on the MOT through the top window. Between the two cameras, the MOT position and diameter can be measured in all three directions. The 2D-MOT is imaged from the push beam direction through a

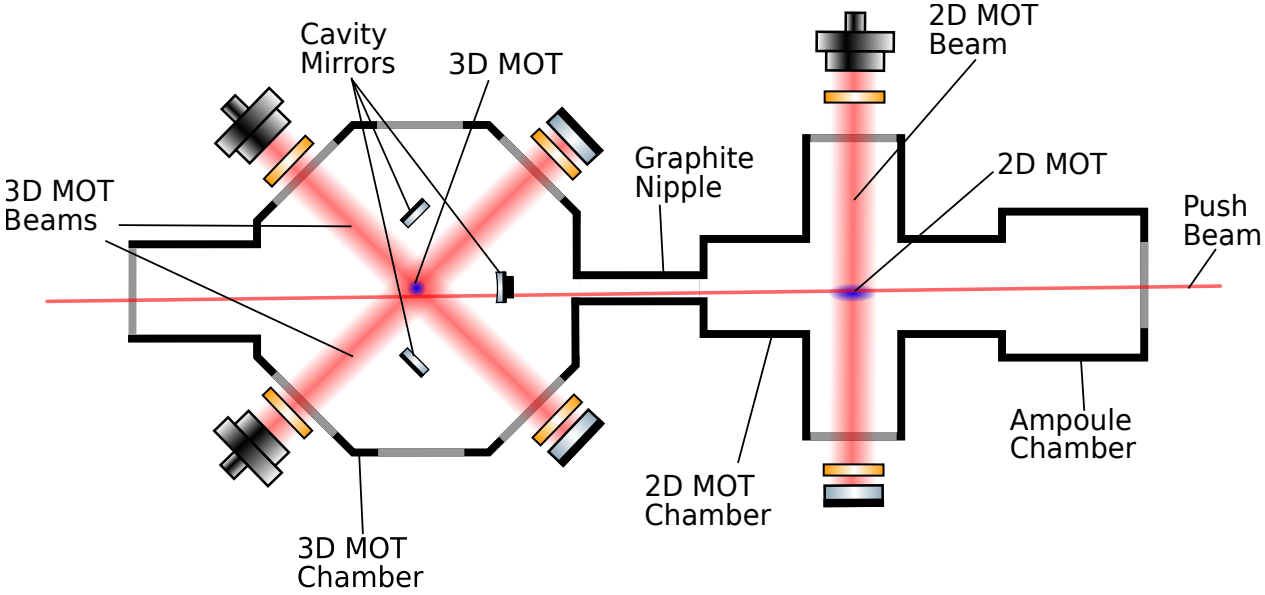

Figure 2.1: Top down view of the vacuum chamber. The push beam passes underneath the curved cavity mirror.

polarising beam splitter, using a webcam. This camera is only used for diagnostics, and no pictures from it are ever saved.

In previous versions of the apparatus, the top 3D-MOT coil, as well as imaging optics and the top MOT beam fibre coupler were mounted directly onto the 3D MOT chamber. One issue with this was that switching the MOT coils would give an impulse to the chamber which would vibrate the ring cavity. In addition, the optics mounts were mounted on the ends of long 1/2 inch diameter steel posts. When excited, these poles would vibrate for several seconds, which meant that the chamber was being perturbed for a long time after the MOT coils were switched. In order to address this problem, a Rexroth frame was built around the cavity, which was mounted directly onto the optical table. All the components that were previously mounted to the 3D MOT chamber were then mounted onto this frame, which isolated them from the vacuum chamber, and therefore the ring cavity. The 2D-MOT coils are never switched, and are rigidly mounted to the 2D MOT chamber. These were not moved, as they do not pose any problems in their current position. In the standard operating conditions of the MOT, 12A is passed through the MOT coils, which produces a

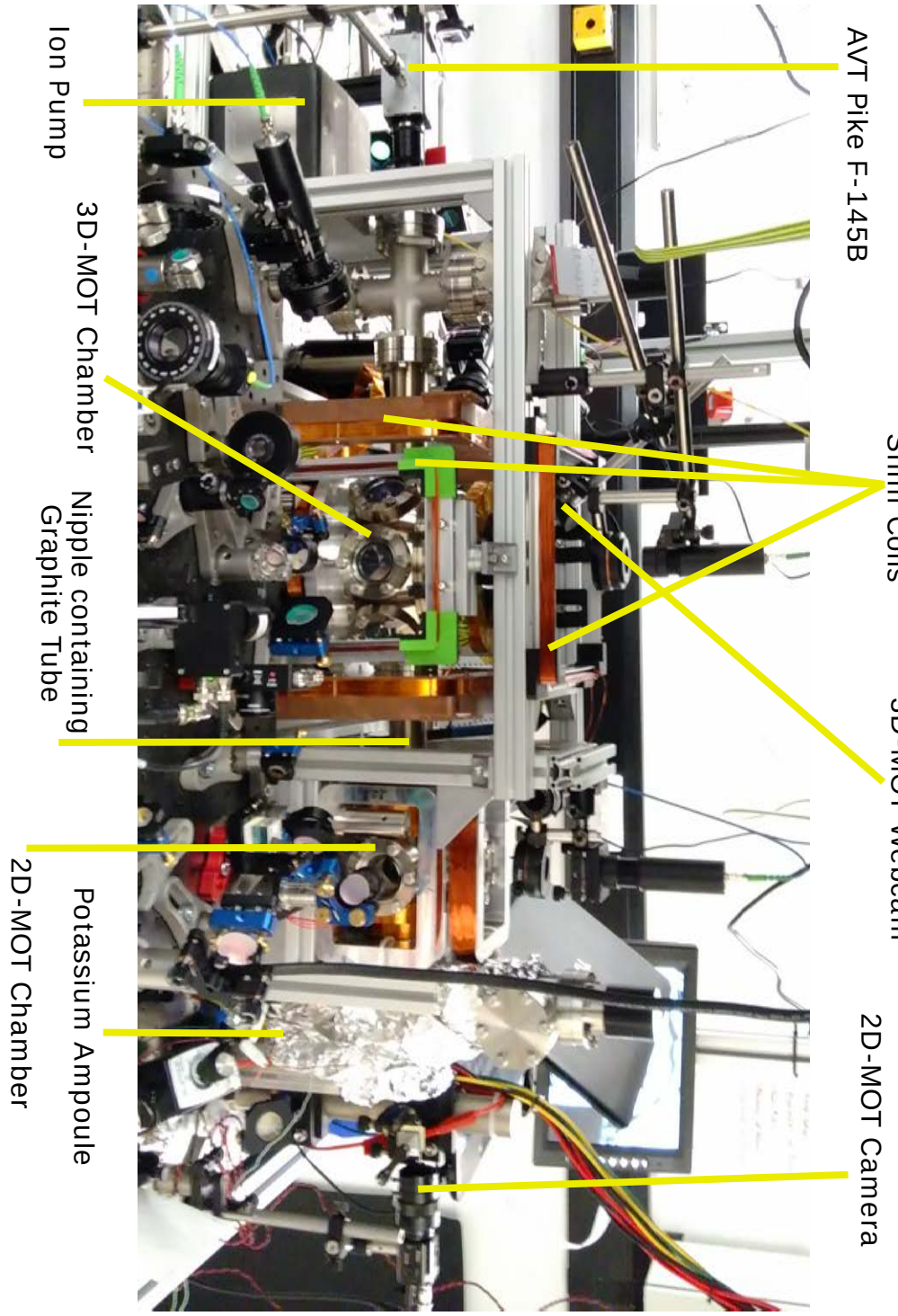

Figure 2.2: Photograph of the vacuum chamber.

B-field gradient of 11 G/cm in the vertical axis and 5.5 G/cm in the horizontal direction in the centre of the 3D-MOT chamber.

Six rectangular coils are placed around the 3D MOT chamber. These are called the shim coils, and are used to produce a uniform magnetic field at the MOT. By changing the current through these coils, the position of the B field zero, and therefore the MOT position is moved. The MOT can then be placed into the cavity mode easily, without physically moving the MOT coils. These coils also allow the MOT to be moved along the cavity axis.The pair of coils that shim the MOT along the push beam axis use two re-purposed MOT coils, described in [32]. These coils are 316×156 mm and produce a field of around 2 G/A at the MOT, as determined by a numerical simulation using Radia [33]. The other two pairs of coils that shim the MOT along the cavity axis and the vertical direction were purpose made. As the space around the experiment is very constrained, there was very little flexibility for the dimensions of the MOT coils. These are therefore constrained to be rectangular coils with dimensions 160×180 mm and 230×230 mm for the vertical and cavity axis directions respectively. The cavity axis coils have 12 turns each, and the vertical coils have 36 turns each. This difference reflects the original intended use of the coils, which was to cancel the earth's B-field. In the UK, this is primarily in the vertical direction so more turns are required for the vertical coils. These coils give approximately 1 G/A in the vertical direction and around 0.15 G/A in the cavity axis direction.

2.2 MOT laser system

The MOT laser system is used to deliver cooling and repump light to the 2D and 3D MOT. This is shown schematically in Figure 2.3.

Three home built external cavity diode lasers are used in the MOT laser system; The master laser is locked to the crossover of the potassium-39 D2 line using a magnetically induced dichrosim lock (MIDL) with a hot vapour cell. This laser provides the frequency

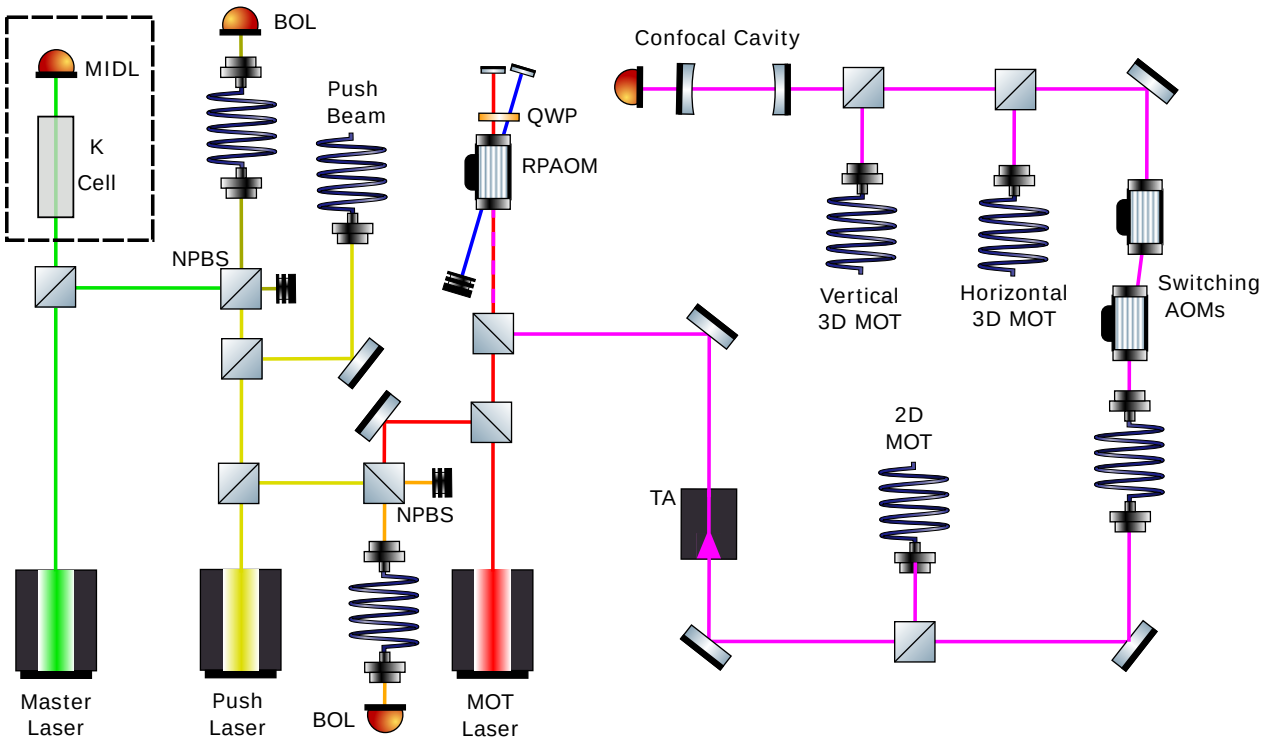

Figure 2.3: Simplified schematic of the MOT laser system. All lenses, optical isolators, and most mirrors are missing from this diagram. All beams splitters are polarising beams splitters with a half-wave plate, except for those labelled NPBS (Non-polarising beam splitter), which are 50/50. The area in the dashed box is the magnetically induced dichrosism lock (MIDL) setup, and is greatly simplified. Other abbreviations are: BOL - beat offset lock, (RP)AOM - (repump) acousto optic modulator, TA - tapered amplifier, QWP - quarter waveplate.

reference for the rest of the system. The push laser is then locked to the master laser using a beat offset lock (BOL) [34], such that the push laser is 205 MHz blue detuned of the master laser, making it close to resonance with the $|F = 1\rangle \rightarrow |F'\rangle$ transition. The push laser is sent to the vacuum chamber, and is used to push atoms from the 2D-MOT to the 3D-MOT. The MOT laser is the source of the cooling and repump beams used to cool and trap the atoms in both the 2D and 3D MOTs. This is locked using a BOL to the push laser, such that the MOT laser is 450 MHz red detuned of the push laser which is approximately resonant with the $|F = 2\rangle \rightarrow |F'\rangle$. A BOL is tunable over a range of several hundred MHz, which allows the frequency of the MOT and push lasers to be easily adjusted. The MOT laser is passed through a double-passed AOM, which is used to create the repump beam. The double pass AOM shift is +454 MHz, which sets the repump beam to be near resonance with the $|F = 1\rangle \rightarrow |F'\rangle$ transition. The unshifted light gives the cooling beam, and the repump and the cooling beam are spatially overlapped. A summary of the frequencies used in the MOT laser system, and their relative frequencies to features of the potassium D2 line is shown in Figure 2.4.

The RF power to the repump AOM (RPAOM) is set to give a cooling to repump ratio of approximately 1:1 at the MOT. The combined cooling and repump beam is amplified using a tapered amplifier (TA) to give enough optical power for both the 3D and 2D MOTs. The beam passes through several telescopes and an aperture in order to recover a good beam shape. Some of the light is then coupled into a single mode fibre (SMF). This light is then split with a fibre beam splitter, and becomes the 2D MOT beams. Each 2D MOT beam has a total power of approximately 80mW. The remaining light is coupled into a short SMF which is used to clean the beam shape. This beam is then passed through a pair of 80MHz AOMs, which allow rapid switching of the MOT light to an arbitrary intensity. The first AOM shifts by +80MHz and the second by -80MHz, giving no overall frequency shift. The beam is then split into three parts using two polarising beam splitters. Two of the beams are coupled into two SMFs, which become the 3D MOT beams. One of the fibres is split using

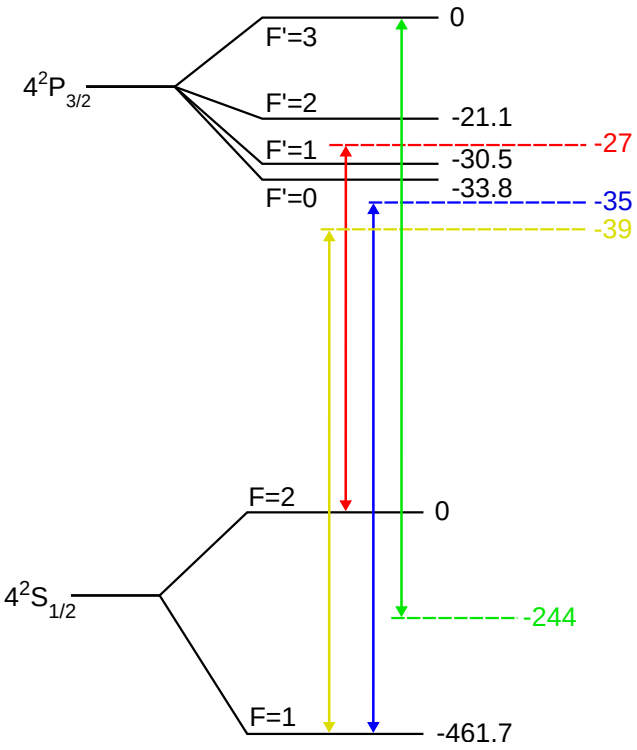

Figure 2.4: Energy level diagram of potassium-39 and the frequencies used in the MOT laser system. The red, yellow, red, and blue lines match the colours in Figure 2.3, and correspond to the master, push, cooling, and repump beams respectively.

a fibre beam splitter, which become the horizontal MOT beam, and the other is used as the vertical MOT beam directly. The third beam is coupled into a high finesse confocal cavity which allows the spectrum of the MOT light to be studied.

This setup gives a total optical power of approximately 13mW into each 3D-MOT beam, split between the cooling and repump beam. Considering all 6 MOT beams, this corresponds to a total maximum intensity of 30 mW/cm^2 at the MOT. Assuming a cooling repump ratio of 1:1, this corresponds to approximately 15 mW/cm^2 at the MOT in each of the cooling and repump beams. This will be considered the default power throughout the rest of this thesis. When most measurements in this thesis were taken, the cooling repump ratio could not be directly measured, due to the non-linear amplification of the TA. The uncertainty on the intensity in each beam is therefore large as the cooling repump ratio could be in the range of 2:1 to 1:2. The power in either beam is therefore 15 ± 5mW/cm^2. In order to reduce this uncertainty an optical cavity was installed in to measure the cooling and repump powers after the TA.

2.2.1 Confocal Cavity

The main new feature of the experimental setup since the previous thesis [28] is the addition of the confocal cavity to measure the relative repump and cooling powers. This is required as it was found that the power ratio between the cooling and repump is strongly dependent on the alignment into the TA. In addition to this, optimising the alignment for either the cooling or repump gives approximately no power in the other beam. A compromise between the two alignments must be found. However, as the TA is operated in a saturated regime, the power in each beam cannot be measured by blocking the other one. The confocal cavity allows measurement of each frequency after the TA, with both beams on simultaneously. The cavity used for this purpose has several design criteria:

1. The TEM modes should be highly degenerate, to make unambiguous identification of features in the transmission spectrum easier.

2. The periodicity of the transmission spectrum should be greater than 460 MHz, which is the potassium hyperfine splitting, in order to allow cooling and repump to be seen without overlapping.

3. The linewidth should be much less than a MHz, in order to give good frequency resolution of the MOT spectrum.

In a confocal cavity, the Gouy phase shift for the $\mathrm{TEM}_{n,m}$ modes is given by,

$$\phi_g = (n+m)\pi \tag{2.1}$$

This means that over a free spectral range, there are only two transmission peaks. One peak corresponds to $\mathrm{TEM}_{n,m}$ modes where $n+m$ is even, and the other where $n+m$ is odd. In general, unless great care is taken to align into any particular mode, these two peaks will have the same amplitude, as each peak is the sum of a large number of high order modes. A confocal cavity therefore meets criterion 1, and has the added benefit of being easy to align.

The periodicity of the transmission spectrum for a confocal cavity is half of the free spectral range, and is given by

$$\nu_p = \frac{c}{4L} \tag{2.2}$$

In order to meet criterion 2, the cavity must therefore be shorter than 16.3 cm. However, a long cavity has the benefit of a narrow linewidth for a given finesse, so a cavity length just shorter than 16.3 cm is ideal. The confocal cavity was therefore designed to have a length of 15 cm, which has a periodicity of 500 MHz. As the repump beam is shifted by 454 MHz, a separation of ~ 46 MHz will be measured between cooling and repump transmission features from different TEM modes. In order to meet criterion 3 using a 15 cm long cavity, the cavity finesse should be much larger than 1000. Assuming the cavity losses are dominated by the mirror losses, the mirrors should have a reflectance of greater than 99.7%. The mirrors used had a specified reflectance of $> 99.96\%$ at 750 to 900 nm, which corresponds to a finesse of $\gtrsim 7800$ and a full width half maxiumum linewidth of $\lesssim 130$ kHz. This is well above the

required cavity finesse. In order to make the cavity confocal, both cavity mirrors had a radius of curvature of 15cm.

The cavity body is constructed from lens tubes. One of the mirrors is mounted directly onto the lens tube, and the other is mounted onto an adjustable zoom housing (Thorlabs SM1ZM), which allows the length of the cavity to be precisely adjusted to meet the confocal condition. The angle of the mirrors cannot be adjusted, but the construction of the cavity is such that they are close to parallel. The cavity is then mounted to the optical table in two places to ensure that it cannot rotate. A photodiode (Thorlabs Det36A/M with 1kΩ termination) is mounted close to the end of the cavity to measure the transmitted light. In order to keep the cavity design simple, the cavity contains no piezo, or any other way to adjust its length. Instead, the MOT laser is scanned to take a spectrum. This gives the limitation that the cooling-repump ratio cannot be measured while the lasers are locked. An example confocal cavity spectrum is shown in Figure 2.5. The two large features correspond to the cooling and repump beams, and the intensity ratio can be determined from this plot. In this trace, the ratio was 1.4. The two smaller peaks correspond to frequencies generated in the TA by a non-linear process.[35] These are at frequencies of $2\nu_c - \nu_r$, and $2\nu_r - \nu_c$, where ν_c and ν_r are the cooling and repump frequencies, respectively. These features are far detuned from any atomic transitions, and so do not affect the MOT. The FWHM linewidth of the cavity is 4MHz, which is significantly larger than the expected linewidth of 130kHz. The asymmetry in the transmission peaks suggests this is due to the cavity length not exactly matching the confocal condition, as the asymmetry can be reversed by changing the cavity length. However, the linewidth is small enough to measure the cooling to repump power ratio, which is the main purpose of the cavity, so fixing this problem will be deferred until a narrower linewidth is required.

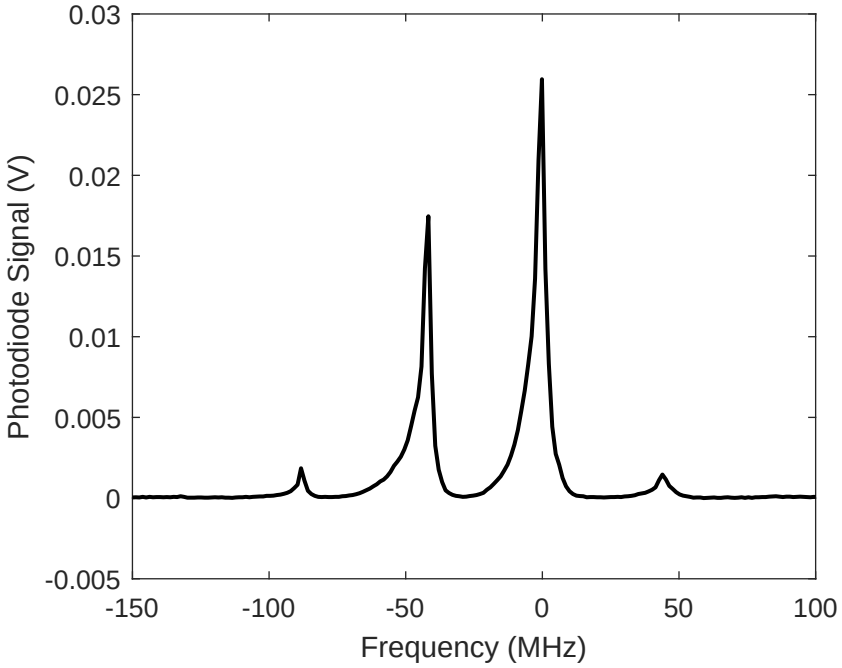

Figure 2.5: Confocal cavity spectrum as the MOT laser is scanned. The x-axis offset has been set so that the cooling peak is at $x = 0$, and the photodiode signal has had the baseline subtracted.

2.3 Probe and Cavity Lock System

The second laser system is used to probe the ring cavity or the atoms and lock the ring cavity. The system is designed such that both the probe and the cavity are ultimately stabilised to an atomic reference. Both lasers in this system are commercial semiconductor ECDLs (Toptica DLPro). A schematic of the probe and cavity lock is shown in Figure 2.6.

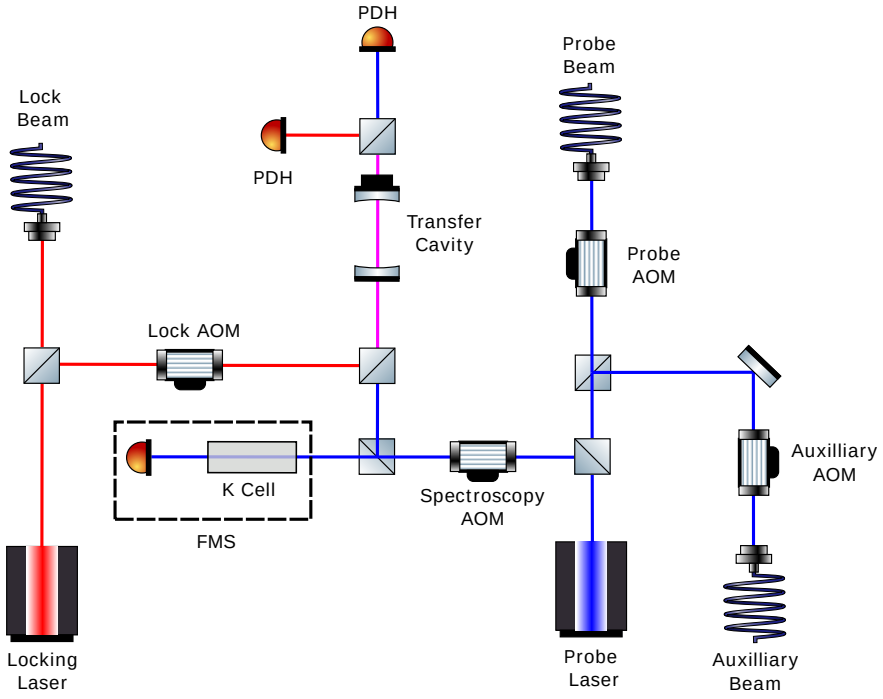

Figure 2.6: Schematic of the probe and cavity locking laser system. Many optical elements are missing in order to simplify the diagram. All AOMs are in the double pass configuration, which is shown explicitly in Figure 2.3. The dashed box labelled FMS (frequency modulation spectroscopy) is especially simplified.

The potassium laser frequency is set to be close to the D2 line of potassium-39. It is split into three beams, using two polarising beam cubes. Each of these beams then passes through a double pass AOM, which allow the frequency of each beam to be independently controlled, while maintaining a lock to spectroscopy. One of the beams, referred to as the spectroscopy beam, is used to stabilise the laser frequency, while the other two beams, referred to as the probe beam and auxiliary beam interact with the cold atoms. The probe beam can be used

to probe both the coupled cavity-atom system, or only the atoms. The auxiliary beam is not used in any experiment presented in this thesis, but was an integral part of previous experiments using this apparatus [36]. The spectroscopy beam is split into two. One of the beams is incident on an optical cavity called the transfer cavity, and the other passes though an potassium vapour cell. The potassium laser is locked to the transfer cavity using the Pound-Drever-Hall technique (PDH). The cavity length is then adjusted, such that the spectroscopy beam is resonant with the ground state crossover of the D2 transition. The transfer cavity is locked to this transition using frequency modulation spectroscopy (FMS). The AOM frequencies are such that when the potassium laser and transfer cavity are locked, the probe beam is approximately resonant with the $|F = 2\rangle \rightarrow |F'\rangle$ and the auxiliary beam is approximately resonant with the $|F = 1\rangle \rightarrow |F'\rangle$.

The locking laser has a wavelength of 852nm, which is very far from any transition in potassium. This is so that the locking laser can be present in the ring cavity without disturbing the atoms. However, in order to stabilise the ring cavity, the locking laser must also be stabilised to an atomic reference. The locking laser is split into two beams with a PBS. One beam is incident on the transfer cavity, and the other is coupled into a fibre, which is coupled into the ring cavity with a power of approximately 1mW. The locking laser is locked to the transfer cavity using PDH. As the transfer cavity length is stabilised to the potassium-39 vapour cell, this stability can be transferred to the locking laser. The ring cavity can then locked to the locking laser using PDH. The result of the implementation of this system is the ring cavity, probe, and auxiliary beams are all locked to an atomic reference.

2.4 Ring Cavity

The ring cavity is mounted on a steel frame, such that the cavity is tilted 45° to the plane of the optical table. The frame is bolted to the bottom of the vacuum chamber. The cavity frame has a 7.5 mm diameter hole that allows the push beam to intersect with the cavity

waist. The cavity has one curved mirror with reflectivity of $99.938 \pm 0.007\%$ and radius of curvature 100 mm. This mirror is glued to a flexure mount with a piezo behind it, which allows the cavity length to be adjusted. The flexure mount is damped by a small piece of Viton[1], which acts to reduce cavity vibrations. This setup allows the cavity length to be adjusted by approximately two free spectral ranges. The other two cavity mirrors are glued onto the cavity frame such that the cavity mirrors form a symmetrical right angled triangle. These mirrors are flat and semi-transparent, and they act as the cavity input/output mirrors. These mirrors have a measured reflectivity of $99.848 \pm 0.003\%$, and a transmissivity of $0.116 \pm 0.001\%$. The ring cavity geometry breaks the symmetry between the polarisations that are parallel and perpendicular to the cavity plane. This means the two polarisations have very different resonance frequencies and finesses. Only the high finesse polarisation, which is perpendicular to the cavity plane, is considered throughout this thesis. The important cavity parameters that result from this arrangement are summarised in Table 2.1. Details of these measurements can be found in [30].

Parameter	**Value**
Cavity Length	9.51 ± 0.05 cm
Round Trip Energy Loss	$0.37 \pm 0.01\%$
Finesse	1710 ± 60
Calculated Cavity Waist	90.2×128.0 μm
Free Spectral Range	3151 ± 2 MHz
Linewidth (FWHM)	1.84 ± 0.06 MHz
Energy Decay Rate (κ)	$2\pi\times$ (1.84 ± 0.06) MHz

Table 2.1: Table of important cavity parameters.

In general, each TEM mode in an optical cavity has a different resonance frequency. This is caused by the Gouy phase shift of the light as it passes through the beam waist, which is different for each TEM mode [37]. As there are, in principle, a countably infinite number of

[1]Viton is a brand of synthetic rubber.

TEM modes, in general, at any cavity length there will be a TEM mode close to resonance for a given frequency. This also means that the $TEM_{0,0}$ mode is arbitrarily close to a large number of TEM modes. In order to make sure both modes can be detected and probed from both sides of the vacuum chamber, two gold mirrors are also glued to the cavity frame. These make the clockwise and counterclockwise modes emerge from the vacuum chamber parallel to each other, separated by approximately 1 cm. Gold mirrors (rather than dielectric mirrors) are used for this purpose, as this preserves the polarisation properties on reflection. A schematic of the optics used to probe and detect the ring cavity is shown in Figure 2.7

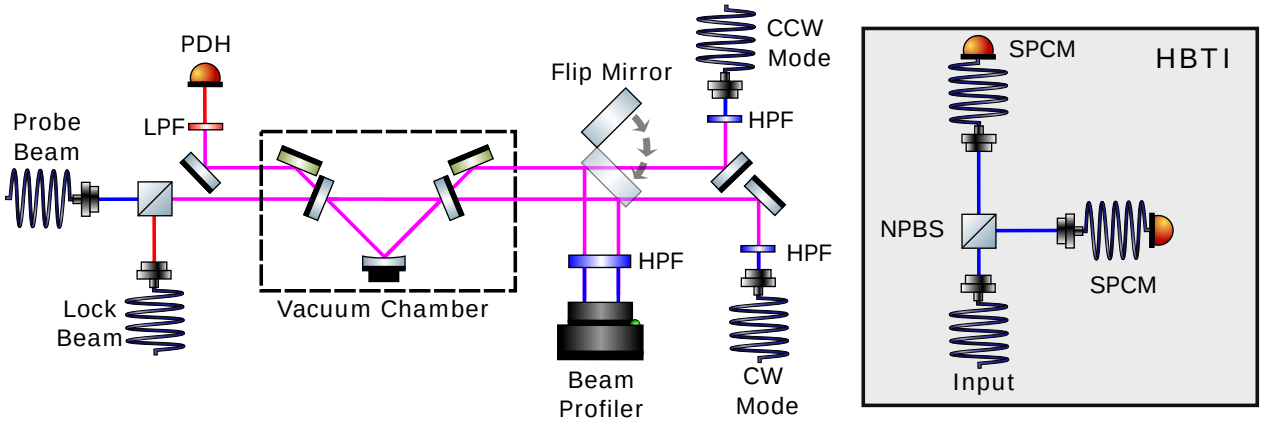

Figure 2.7: Schematic of the ring cavity probing and detection. LPF and HPF stand for low pass filter and high pass filter, and block the 767nm and 852nm light respectively. The section in the dotted box represents what is inside the vacuum chamber. The inset box shows the Hanbury Brown-Twiss interferometer (HBTI), which consists of a 50/50 non-polarising beam splitter (NPBS) and two fibre coupled single photon counting modules (SPCMs).

The lock and probe beams are combined on a polarising beam splitter, then are passed through a single lens used for mode matching with the $TEM_{0,0}$ mode, before being incident on the cavity. The reflected light passes through a low pass filter to remove the probe light, and is detected on a photodiode. This signal is used for PDH locking of the cavity to the lock beam. The transmitted light goes to the detection apparatus, described in the next section.

2.4.1 Detection

On the other side of the cavity, a flip mirror either directs both modes to a beam profiler or to be separately fibre coupled into SMFs. The beam profiler (Thorlabs BC106-VIS) allows imaging of the beam shape of both modes and measurement of the total power emitted into all TEM modes. The beam power was calibrated using a beam of known power in order to allow conversion from beam profiler counts to nanowatts. The SMFs are aligned in order to maximise coupling to the $TEM_{0,0}$ mode of the cavity, which filters out higher order modes effectively. The output from the SMFs are then either detected on an avalanche photodiode (APD) (Laser Components LCSA500-03 APD), detected with a single photon counting module (SPCM) (Perkin Elmer SPCM-AQRH-13-FC), or sent to a Hanbury Brown-Twiss interferometer (HBTI). The APD is used for real time measurement of the power in the $TEM_{0,0}$. The limitations of the APD are that it cannot detect very low powers, and it has a finite bandwidth. The SPCMs can be used to address these problems. They have a timing resolution of 80 ps, which in principle allow very fast timescale processes to be seen. They have a quantum efficiency of $\sim 60\%$ and a dark count rate of 200 s^{-1}, which corresponds to a power of $\sim 5 \times 10^{-17}$ W. All specifications are given for 766.7nm light. Very low powers can therefore be detected with good signal to noise. However, due to losses in fibre coupling, the total detection efficiency of the SPCM is significantly lower than the maximum possible efficiency. The fibre coupling efficiency was measured to be approximately 10% for the $TEM_{0,0}$ mode, although this can vary by several percentage points depending on the alignment on a particular day. The maximum count rate of the SPCMs is $\approx 10^6$ counts per second, which is determined by the dead time of the detectors of 50 ns. If the count rate is raised above this limit, a significant number of counts are missed by the detector due to photons arriving within the dead time of the detectors. In order to keep the count rate below this limit, the output from the cavity could be attenuated with a pair of neutral density filters. The attenuation used depended on the total power, and varied from no attenuation

to 10^{-6}, depending on the power of the beam being detected.

The HBTI is used for making measurements of the second order coherence time, which is discussed in Chapter 3 and a schematic of the HBTI is shown in the inset of Figure 2.7. Due to losses in fibre coupling, the total detection efficiency of the HBTI was measured at 1.6% and detection efficiency was also different in each of the two arms by a factor of two. However, as the second order coherence is independent of detection efficiency, this was not considered a major problem.

CHAPTER 3

LASING WITH COLD POTASSIUM ATOMS

This chapter discusses the cold atom ring laser produced when the MOT is overlapped with the cavity modes. First, the system is demonstrated to be lasing by means of a threshold curve and a second order coherence measurement, both of which show characteristics of lasing. Then aspects of lasing unique to the ring cavity geometry are studied. In particular, directional bistability is observed, and the two counter propagating lasing modes are demonstrated to be non-reciprocal. Parts of this chapter are taken from [38].

3.1 Demonstration of Lasing

The MOT was overlapped with the cavity modes using the shim coils, and the cavity was scanned over a range of several hundred MHz. The cavity output was then collected into a single mode fibre and detected on the APD. Several peaks were observed on the APD trace, which suggests there is light emission from the cavity at several different cavity lengths, which were thought be lasing into different transverse modes. In principle all modes except for the $TEM_{0,0}$ should be filtered out by the single mode fibre which collects the light, but in practice, some higher order modes are coupled into the fibre due to imperfect coupling. In order to demonstrate the presence of lasing high order modes, the cavity modes were then imaged onto a beam profiler. This allowed the beam shape to be imaged, from which separate transverse modes can be easily seen. A selection of beam profiler images for different cavity

lengths are shown in Figure 3.1.

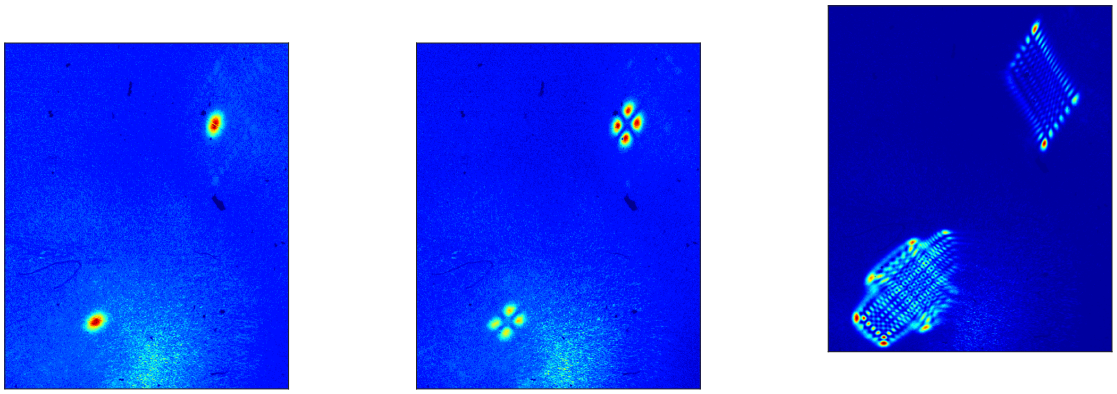

(a) Lasing into (0,0) (b) Lasing into (1,1) (c) Lasing into high order modes

Figure 3.1: Lasing into different transverse modes. The upper-right feature is the CCW mode, and the lower left feature is the CW mode. There are relatively low order modes $(n, m < 20)$ within a gain bandwidth of any given cavity length. This leads to lasing at every cavity length.

Note that in Figure 3.1c, the two directions appear very differently. This is the first evidence that there is some non-reciprocity between the two lasing directions. However, these images do not prove that the light we are detecting is lasing. One possible alternative is that the cavity emission is Purcell-enhanced fluorescence of the atoms. To prove lasing two measurements were made: A threshold curve, and a $g^{(2)}$ measurement.

3.1.1 Threshold Curve

One characteristic of lasing is the presence of a threshold. The threshold occurs when round trip gain is equal to the round trip loss for a weak probe beam. If the gain is below this value, light does not build up in the cavity. However, if the gain is higher than the loss, the light in the lasing mode grows exponentially, until the gain is saturated. At this point, the gain is pinned to the round trip losses and a steady state is reached. Typically the gain is saturated by the optical pumping from the lasing process having a comparable pump rate

which maintains the gain. The lasing power above threshold is therefore linear with respect to the total pumping rate, and therefore is linear with respect to the atom number in the case of a cold atom laser with fixed pump rate per atom. A plot of lasing power against atom number (or some other parameter that the gain depends on) is known as a threshold curve. This plot has two important parameters: the threshold, and the slope efficiency. The threshold gives the atom number where the round trip gain is equal to one. From this, the average gain per atom can be determined. The slope efficiency is the gradient of the curve above threshold. This gives the average power scattered into the cavity per atom. To take a threshold curve, the push beam was blocked, which strongly reduced the loading rate of the MOT. This brought the system well below threshold. The push beam was then unblocked, which allowed the MOT to refill over a timescale of ~ 7 seconds. This process causes the system to pass slowly across threshold. The output of the cold-atom laser was then detected on the beam profiler, which had been calibrated using a probe of known power. This method has several advantages over the intuitive method of changing the MOT beam power and measuring the lasing power. Firstly, the fact that the MOT beam powers were fixed made it easy to measure the atom number, as the fluorescence emitted from the MOT is proportional to the atom number. If the MOT powers were altered, the fluorescence from the MOT is dependent on both the scattering per atom and the number of atoms. Similarly, the single pass gain depends on both the beam power and atom number. Changing the MOT power therefore changes the gain in a non-trivial way, and so a linear threshold curve would not be expected if the MOT beam powers were changed. However, the single pass gain is proportional to the atom number, so a linear threshold would be expected from the MOT loading method. Finally, due to the experimental control system, the MOT powers can not be quickly and continuously changed by the computer. The MOT beam power would therefore have to be adjusted manually, which would mean a threshold curve measurement would take several minutes, rather than the several seconds required for the MOT loading method. The MOT loading method therefore minimises the effect of low frequency drifts in

the experimental parameters.

One problem with this method was that the connection between the beam profiler and the computer where the images were saved was slow, which limited the frame rate of the beam profiler. Decreasing the size of each image meant that the frame rate could be increased to give good atom number resolution. However, to get a good frame rate the size of the image had to be decreased to the point where only one direction of the laser could be imaged at any given time. This meant that the CW and CCW thresholds had to be taken in separate measurements. Taking each measurement separately allows a frame rate of 8 Hz, which was sufficient to get good atom number resolution.

Using the beam profiler meant that the power from every transverse mode was measured. This was advantageous as it meant the total output power of the laser was measured and so any noise from competition between transverse modes was not measured. The total MOT number was measured by taking pictures of the MOT, and the effective number of the atoms interacting with the cavity was determined using the method described in [30]. The total MOT beam intensity for this measurement was 18mW/cm^2, which was chosen so that the threshold, a clear section of $P_{out} = 0$, and a linear section could be seen in a single measurement. The threshold measurement obtained is shown in Figure 3.2.

In order to extract the atom number at threshold and the slope efficiency, the data below threshold were deleted, and a linear fit to the remaining data was performed. The x-intercept then gave a threshold atom number of $6.2 \pm 0.6 \times 10^7$ atoms, with a slope efficiency of 2.8 ± 0.2 fW per atom. The uncertainties are calculated from the uncertainty of the fitted lines. This means there may be systematic errors in the measurement of the atom number and output power which are not accounted for in the stated uncertainties. The percentage of atoms in the MOT that interact with the cavity mode was calculated to be approximately 0.5%. This was calculated by calculating the overlap between the cavity and the MOT under the assumption that the cavity mode waist is small compared to the MOT but the MOT diameter is small compared to the Rayleigh length of the cavity. When this is taken into account, the

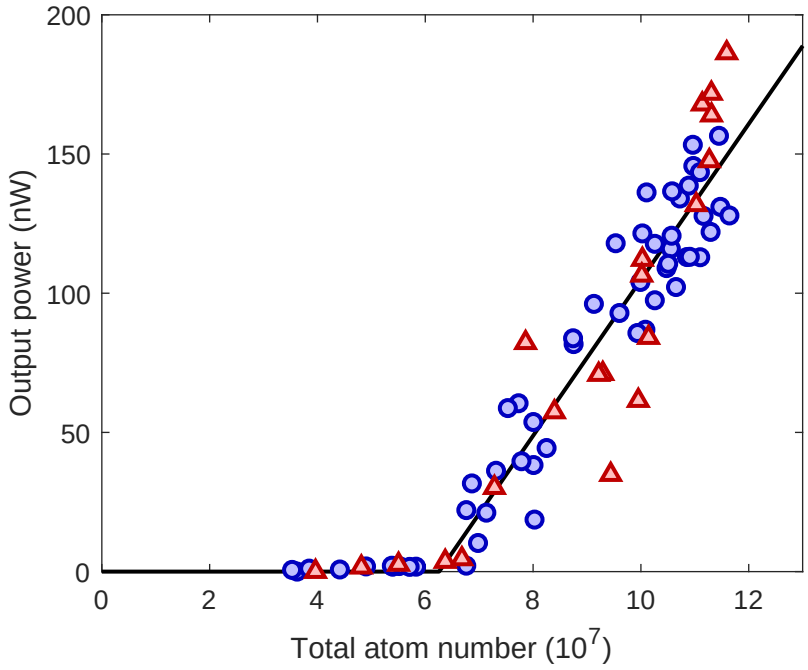

Figure 3.2: Threshold measurement of the Cold atom laser. Blue circles and red triangles give the output power of the clockwise and counterclockwise modes respectively. The black line is a linear fit to the combined data from both directions above threshold.

effective slope efficiency for the atoms in the cavity is 560 ± 40 fW per atom. For scale, this is comparable to the energy emitted by spontaneous emission from saturated atoms which is $\frac{1}{2}\gamma\hbar\omega = 780$ fW per atom, indicating that the gain saturates when the population transfer rate due to spontaneous emission is similar to the transfer rate caused by the lasing process, as expected. However, due to the small diameter of the lasing mode, this saturation is not directly measurable in the populations, as any probe beam will primarily measure the populations of the atoms not interacting with the cavity mode. The threshold curve in Figure 3.2 is consistent with lasing.

3.1.2 Degree of Second-Order Coherence

Another way of detecting a transition to lasing is to measure the statistics of the emitted light. This can be done using the degree of second order coherence, $g^{(2)}(\tau)$, which is a measure of the correlation between the intensity of a field at a given time, and the intensity at a different time, τ later. It is defined as

$$g^{(2)}(\tau) = \frac{\langle a^\dagger(t)a^\dagger(t+\tau)a(t+\tau)a(t)\rangle}{\langle a^\dagger(t)a(t)\rangle^2} \tag{3.1}$$

where $a(t)$ is the cavity lowering operator and angle brackets denote an expectation value. Using the commutation operator $\left[a, a^\dagger\right] = 1$ and $a^\dagger a = n$, for $\tau = 0$,

$$g^{(2)}(0) = \frac{\langle n^2\rangle - \langle n\rangle}{\langle n\rangle^2}. \tag{3.2}$$

The definition of the variance is $\mathrm{Var}(n) = \langle n^2\rangle - \langle n\rangle^2$. Substituting this into Equation 3.2 and rearranging gives

$$g^{(2)}(0) = 1 + \frac{1}{\langle n\rangle}\left(\frac{\mathrm{Var}(n)}{\langle n\rangle} - 1\}\right), \tag{3.3}$$

meaning $g^{(2)}(0)$ can be interpreted as a measure of the variance. In this interpretation it is apparent that $g^{(2)}(0)$ is not only dependent on the fundamental quantum state of the system (e.g number state, coherent state), but also on any intensity noise with a technical source.

For a monochromatic field of constant power, as would be expected for an ideal laser, $a(\tau) = a(0)e^{-\omega\tau}$. The τ dependence of Equation 3.1 therefore disappears. Assuming a coherent state gives a result for an ideal laser as $g^{(2)}(\tau) = 1$ for all τ.

A thermal state is defined by its density matrix,

$$\rho_t = \frac{1}{Z}\sum_n e^{-\beta n}\left|n\right\rangle\left\langle n\right|, \tag{3.4}$$

where Z is the partition function, $Z = \sum_n e^{-\beta n} = e^\beta(e^\beta - 1)^{-1}$, which normalises the

probabilities and $\beta = \hbar\omega/k_B T$. Using that an expectation value of a general operator, O, is given by $\langle O \rangle = \mathrm{Tr}\{O\rho\}$, after expanding the sums over n, we get that for a thermal state,

$$\langle n \rangle = \frac{1}{Z} \frac{e^{\beta}}{(e^{\beta}-1)^2} = \frac{1}{e^{\beta}-1}, \tag{3.5}$$

$$\langle n^2 \rangle = \frac{1}{Z} \frac{e^{\beta}(e^{\beta}+1)}{(e^{\beta}-1)^3} = \frac{1+e^{\beta}}{(e^{\beta}-1)^2}, \tag{3.6}$$

and

$$\langle n \rangle^2 = \frac{1}{Z^2} \frac{e^{2\beta}}{(e^{\beta}-1)^4} = \frac{1}{(e^{\beta}-1)^2}. \tag{3.7}$$

After substituting these results into Equation 3.2 and some algebra we arrive at the result that for a thermal state $g^{(2)}(0) = 2$. For large τ, photon arrival times must be uncorrelated, and therefore $g^{(2)}(\infty) = 1$ for any state, including a thermal state. For a thermal state, $g^{(2)}(\tau)$ decays exponentially from 2 to 1 over some coherence time which is determined by the linewidth of the source, and is given by

$$g^{(2)}(\tau) = 1 + e^{-\tau/t_c} \tag{3.8}$$

where t_c is the coherence time of the light [39]. A measurement of $g^{(2)}(0)$ therefore provides a good test of lasing, as if the system is brought above threshold, we would expect a change from a thermal state to a coherent state [40], and a corresponding change in $g^{(2)}(0)$ from 2 to 1.

3.1.3 Measuring the Degree of Second-Order Coherence

To measure $g^{(2)}$, a Hanbury-Brown Twiss interferometer is used, which is shown schematically in the inset of Figure 2.7. The light from the clockwise mode of the cavity is coupled into a single-mode fibre in order to filter out the higher order modes. The output from this fibre is incident on a 50/50 beam splitter, and each output of the beam splitter is sent to a single-

photon counting module (SPCM), which generates a time stamp when a photon is detected. This setup allows the measurement of the expectation value of the number of photons in each mode at any given time, and so can be used to measure,

$$M(\tau) = \frac{\langle n_c(t+\tau) n_d(t) \rangle}{\langle n_c(t) \rangle \langle n_d(t) \rangle} = \frac{\langle c^\dagger(t+\tau) c(t+\tau) d^\dagger(t) d(t) \rangle}{\langle c^\dagger(t) c(t) \rangle \langle d^\dagger(t) d(t) \rangle} \tag{3.9}$$

where c and d are the lowering operators of the output modes of the beam splitter. Note that the denominator of Equation 3.9 is averaged over time, so the choice of $n(t)$ or $n(t+\tau)$ gives the same answer. For a beam splitter the output modes are related to the input modes by the relations,

$$c = \frac{a+ib}{\sqrt{2}} \qquad c^\dagger = \frac{a^\dagger - ib^\dagger}{\sqrt{2}} \qquad d = \frac{a-ib}{\sqrt{2}} \qquad d^\dagger = \frac{a^\dagger + ib^\dagger}{\sqrt{2}}, \tag{3.10}$$

where a and b are the lowering operators of the input modes of the beam splitter. a is the mode being studied, and b is in the vacuum state. c and d represent separate modes, and so they commute. Equation 3.9 can then be normally ordered with no additional terms. After normal ordering, Equation 3.10 can be substituted into Equation 3.9 to give the measured value in terms of the input modes,

$$M = \frac{\langle [a^\dagger(t+\tau) - ib^\dagger(t+\tau)][a^\dagger(t) + ib^\dagger(t)][a(t+\tau) - ib(t+\tau)][a(t) + ib(t)] \rangle}{\langle [a^\dagger(t) - ib^\dagger(t)][a(t) + ib(t)] \rangle \langle [a^\dagger(t) + ib^\dagger(t)][a(t) - ib(t)] \rangle} \tag{3.11}$$

The mode relating to b is in the vacuum state, meaning any term which has a b with no $b^\dagger$ to the right of it, and any mode which has a $b^\dagger$ with no b to the left of it will give 0 when the expectation value is taken. This leaves only one term in each set of angled brackets, giving

$$M(\tau) = \frac{\langle a^\dagger(t) a^\dagger(t+\tau) a(t+\tau) a(t) \rangle}{\langle a^\dagger(t) a(t) \rangle^2} = g^{(2)}(\tau), \tag{3.12}$$

which is the definition of $g^{(2)}(\tau)$.

The output of the SPCMs was in the form of a list of time stamps indicating the time of

arrival of each photon to a precision of 80 ps. The arrival times were then binned into two histograms of bin width of $t_{bin} = 5$ ns. The two histograms represent the photon counts from the different detectors. The value of t_{bin} was chosen to be much smaller than the expected coherence time, which ensures that $g^{(2)}(0)$ can be resolved. The correlation between the two histograms was then taken, which gives the numerator of Equation 3.9. As the time stamp files can be very large (approximately GB), and the bin width is small compared to the measurement time, it isn't practical to calculate the correlation of the whole time stamp file in one calculation. The data are therefore separated into sections of length ~ 400 ns. The correlation is calculated for these short sections, and the correlations are then averaged. This significantly reduces the amount of RAM required, as well as the time taken to process the data. $g^{(2)}(\tau)$ is then calculated according to [41],

$$g^{(2)}(\tau) = 1 + \left(1 + \frac{R_d}{R_1}\right)\left(1 + \frac{R_d}{R_2}\right)\left(\frac{C(\tau)}{t_{int}t_{bin}(R_1 + R_d)(R_2 + R_d)} - 1\right), \tag{3.13}$$

where R_d is the dark count rate of the SPCMs (~ 100 Hz), R_1 and R_2 are the count rates of the SPCMs, t_{int} is the total integration time of the measurement, and $C(\tau)$ is the correlation between the two histograms. This formula accounts for the dark counts of the detectors. If $R_d = 0$, it reduces to Equation 3.9.

Assuming the count rates of the two modes are constant and independent gives the coincident count rate as approximately, $R_{co} \sim R_1 R_2 t_{bin}$. The maximum count rate of the SPCMs before saturation was of the order of 10^6. To ensure the SPCMs were not saturated, the count rate was attenuated to around 10^5 counts per second. While lasing, this was done using a pair of neutral density filters which each attenuated by a factor of $\sim 10^{-4}$. For fluorescence, the attenuation from fibre coupling alone gave the correct count rate. This count rate meant that the approximate counts per bin was 5×10^{-4} and the approximate coincidence count rate, assuming uncorrelated photons, was 50 Hz, requiring data to be taken for many seconds to avoid excessive shot noise. This meant that slow intensity fluctuations were present over

the measurement timescale. For fluorescence, the intensity fluctuations are relatively small, but for lasing, the presence of a threshold effectively amplifies any technical noise. Bistability associated with the ring laser geometry, which is discussed in section 3.3, also causes large variations in intensity. To eliminate this noise, and allow $g^{(2)}(0)$ to act as a measurement of the coherence of the state, the effect of the variations was removed by calculating their effect on the photon statistics.

Assuming the laser is in a coherent state with a varying intensity, the photon arrival times can be approximated as Poissonian with a mean arrival rate $R(t)$. The conditional probability of detecting n photons in a time T is then

$$p(n|R) = \frac{(RT)^n e^{-RT}}{n!}. \tag{3.14}$$

This leads to formulae for the expectation values for n and n^2,

$$\langle n \rangle = \sum_n \sum_R \frac{np(R)(RT)^n e^{-RT}}{n!} \qquad \langle n^2 \rangle = \sum_n \sum_R \frac{n^2 p(R)(RT)^n e^{-RT}}{n!} \tag{3.15}$$

The sums over n can then be evaluated, and the remaining sums over R can then be expressed in terms of $\langle R \rangle$ and $\langle R^2 \rangle$, which gives an expression for $\mathrm{Var}(N)$ in terms of R,

$$\frac{\mathrm{Var}(n)}{\langle n \rangle} = 1 + T\frac{\mathrm{Var}(R)}{\langle R \rangle}. \tag{3.16}$$

Using Equation 3.3 and that $T = \frac{\langle n \rangle}{\langle R \rangle}$, we reach an expression for the measured second order coherence of a coherent state with slow intensity noise, which can then be used as a correction factor, χ:

$$\chi = \frac{\mathrm{Var}(R)}{\langle R \rangle} + 1 \tag{3.17}$$

χ was calculated for four different data sets with $T = 10^{-4}$ s. This value was used as it is faster than the intensity noise, but slower than the mean separation of photon counts. The values of χ calculated were 6.7, 6.7, 3.7, and 5.8, meaning the intensity noise varied significantly

between data sets. However, each value of χ gave a corrected $g^{(2)}(\tau) \sim 1$ indicating this technique is effective at compensating for the effect of intensity noise. The fluorescence data can be analysed in a similar way, with an initial assumption of a thermal state rather than a coherent state. However, the intensity noise of the fluorescence is an order of magnitude lower than for the lasing so the compensation is unnecessary for fluorescence data, and is not performed. The compensated $g^{(2)}(\tau)$ for lasing is plotted alongside the uncompensated $g^{(2)}(\tau)$ for fluorescence in Figure 3.3.

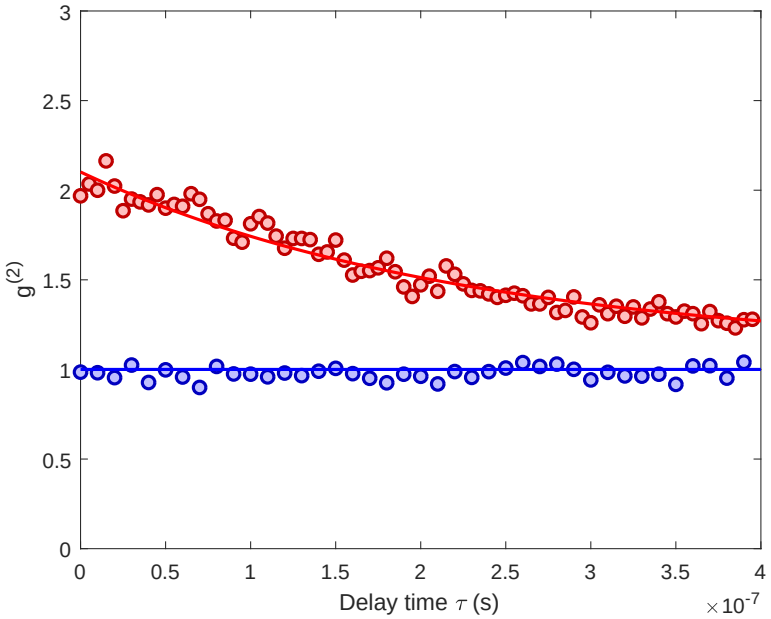

Figure 3.3: Red circles are data taken below threshold and blue circles are data above threshold. The red line is a fit to the data of the form of Equation 3.8 and the blue line is at $g^{(2)}(\tau) = 1$, as expected for lasing.

The data taken below threshold were fitted to Equation 3.8. It can be seen that this produces a good fit to the data. This provides evidence for lasing by showing that when the system is brought above threshold, a transition from a thermal state to a coherent state takes place. The coherence time from the fit to Equation 3.8 is 170 ± 5 ns, which is approximately twice the empty cavity coherence time of $\frac{1}{\kappa} = 88$ ns. This increase from the expected coherence time is explored further in Chapter 5.

3.2 Polarisation

As the cavity is strongly birefringent, the gain curve can only be on resonance with the $TEM_{0,0}$ for one linear polarisation at a time. In addition to this, the two linear polarisations have very different finesse, as the mirror reflectivity is much lower for the p-polarisation than the s-polarisation. Both of these facts suggest that the laser should only emit into the high finesse polarisation of the cavity, and so a linear polarisation should be expected from the output.

In order to confirm this, the light was passed through a linear polariser (Thorlabs LPNIRE100-B), and detected on the beam profiler. Because the cavity is mounted at 45° relative to the plane of the optical table, any dielectric mirror would act like an arbitrary waveplate, which would destroy the expected linear polarisation of the output. The polariser therefore had to be placed immediately after the vacuum chamber. The mirrors inside the vacuum chamber are gold, which is not birefringent so they do not have this effect.

The polariser was then rotated, and the power measured on the beam profiler. For perfectly linearly polarised light, $I = I_0 \cos^2(\theta)$, where at $\theta = 45°$, no light is transmitted. For circularly polarised and unpolarised light, half of the light is blocked, independent of angle. In general, any polarisation can be given by a superposition of linear, circular, and unpolarised light. The expression for the expected intensity is then given by

$$I = I_l \cos^2(\theta) + \frac{I_c + I_u}{2} \tag{3.18}$$

where I_l represents the linear polarised component, I_c represents the circularly polarised component,and I_u represents the unpolarised component. By measuring the extinction ratio of the polariser, the degree of linear polarisation can be determined. This measurement is shown in Figure 3.4.

Each data point is the made from averaging the intensity from 20 beam profiler pictures in order to average over the intensity noise of the laser. The background intensity was

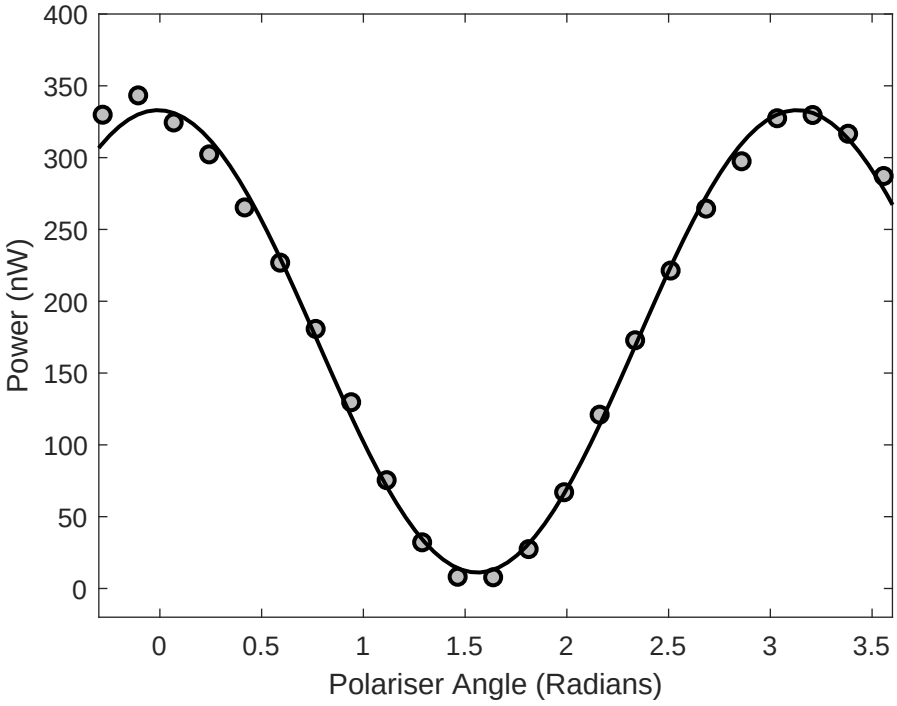

Figure 3.4: Lasing intensity measured on the beam profiler as a polariser is rotated. The dots show experimental data, and the line shows a fit to the data of the form of equation 3.18. The x-axis offset was set so there was an intensity maximum at $\theta = 0$.

measured by measuring intensity in a region of the beam profiler not hit by the laser. This was then subtracted from the raw intensities to give the lasing intensities. The fit to the 3.18 gives $I_c + I_u = 14 \pm 7$nW, and $I_0 = 320 \pm 16$nW, which suggests the laser is $96 \pm 2\%$ linearly polarised, meaning the laser is primarily linear polarised. It should be noted that the fit overestimates the data at the intensity minimum suggesting that the fit overestimates $I_c + I_u$. Other reasons for a possible overestimating $I_c + I_u$ are that the polariser itself does not have a perfect extinction ratio, or that the background is improperly subtracted due to a non-uniform dark count rate on the detector. In addition, vacuum chamber windows have been shown to be slightly birefringent, which make the laser light elliptically polarised [42]. More work is needed to eliminate these sources of error and confirm if the laser is perfectly

linearly polarised, as expected.

3.3 Bistablility

One property of a ring cavity that distinguishes it from a Fabry-Perot cavity is that there are two counter-propagating modes which are entirely spatially overlapped. This means that each mode will interact with the same group of atoms. In a Fabry-Perot cavity, there are not counter propagating modes, so each TEM mode interacts with a slightly different set of atoms. Ring cavities are therefore distinct from Fabry-Perot cavities in that the complete overlap between the counter propagating modes leads to stronger saturation effects than would be possible in a Fabry-Perot cavity. The lasing dynamics from a laser, with two counter propagating modes can be described phenomenologically with a pair of dimensionless equations [43]:

$$\begin{aligned} \dot{E}_1 &= \left[a_1 + p_1(t) - |E_1|^2 - \xi|E_2|^2\right] E_1 + q_1(t) \\ \dot{E}_2 &= \left[a_2 + p_2(t) - |E_2|^2 - \xi|E_1|^2\right] E_2 + q_2(t), \end{aligned} \tag{3.19}$$

where 1 and 2 label the clockwise and counterclockwise modes, E_i represents the electric field, a is a phenomenological pump parameter, which is 0 below threshold and greater than zero above threshold, p_i represents random noise associated with the pumping power, ξ represents cross coupling between the clockwise and counterclockwise modes, and q_i represents spontaneous emission into the cavity modes and is a white, Gaussian, delta correlated noise term. ξ, the cross coupling term, is determined by the broadening mechanism of the gain curve. For two modes that overlap, if the laser cavity is on resonance with the gain, both modes interact symmetrically with the atoms, meaning $\xi = 1$ for Doppler gain broadening. If the cavity is moved off resonance with the gain peak, then each mode interacts with a different velocity class of atoms, meaning the cross saturation is reduced, meaning for a Doppler broadened gain medium, $0 \leqslant \xi \leqslant 1$ [44]. For a homogeneously broadened ring laser,

the standing wave produced by the two modes travelling in opposite directions provides a mechanism for another coupling term between the two modes. On resonance, the coupling from this mechanism is equal to the normal saturation term. This means that on resonance, $\xi = 2$ meaning the effect of saturation from the opposite mode is stronger than the effect of self-saturation. From Equation 3.19, after setting $p_1(t)$, $p_2(t) = 0$ it can be shown that the joint probability of measuring a given intensity in each mode is given by [43],

$$P(I_1, I_2) = \frac{1}{Q} \exp\left\{ \frac{a_1 I_1 + a_2 I_2 - \xi I_1 I_2}{2} - \frac{I_1^2 + I_2^2}{4} \right\} \tag{3.20}$$

where Q is the normalisation factor, and I_1 and I_2 are the dimensionless intensities of the two modes. Integration over I_2 gives the probability of detecting the laser emitting with intensity I_1, with no information about the second mode. This gives

$$P(I_1) = \frac{\sqrt{\pi}\left[1 - \mathrm{erf}\left(\frac{1}{2}\xi I_1 - \frac{1}{2}a_2\right)\right]}{Q} \exp\left(\frac{1}{4}[\xi^2 - 1]I_1^2 - \frac{1}{2}[a_2\xi - a_1]I_1 + \frac{1}{4}a_2^2\right) \tag{3.21}$$

From examination of this equation, it is apparent that two of the terms in the exponential change sign at $\xi = 1$ for $a_1 = a_2$. Significant changes in behaviour would therefore be expected around these values.

Figure 3.5 shows the behaviour of a laser with different cross coupling strengths and equal pumping in each direction. Each coupling strength shows qualitatively different behaviour. For $\xi = 0$, both modes have a roughly constant intensity, with $I_1 \approx I_2 \approx a$. For $\xi = 1$, the total lasing power is roughly constant, but is split between each mode, such that $I_1 + I_2 \approx a$. Each possible way of producing a total output intensity of a is equally common. For $\xi = 2$, there are two distinct regions with a non-zero probability of occurring, at $I_1 \approx a, I_2 \approx 0$, and $I_1 \approx 0$, $I_2 \approx a$. This results in a twin peaked structure in the probability density of I_1. As the probability of having intermediate intensity is very low, any switching between the high and low intensities must occur nearly instantaneously compared to the dwell time in each region. The system for $\xi = 2$ is therefore bistable. The $q_i(t)$ term in Equation 3.19 causes random

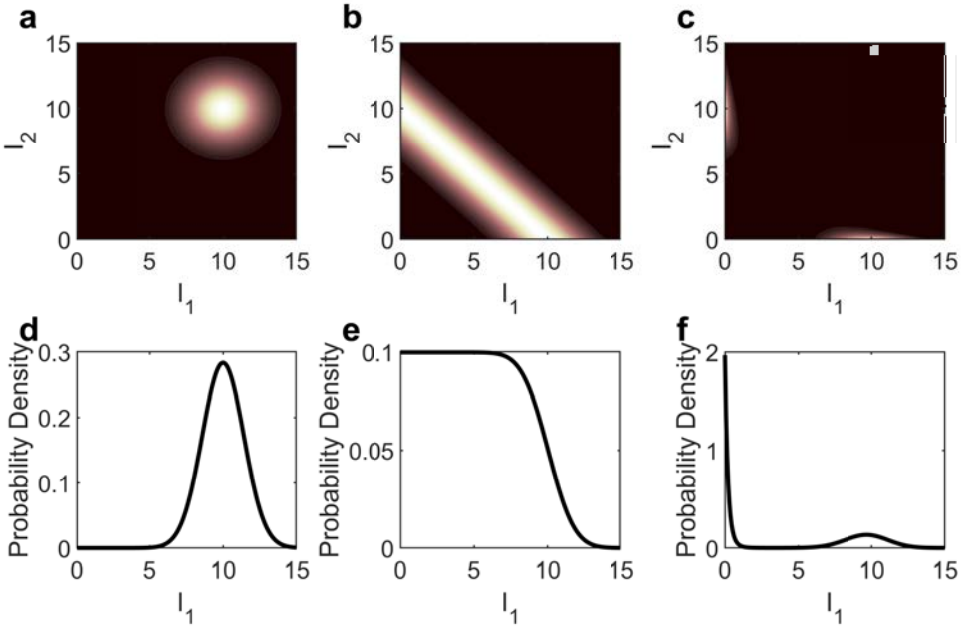

Figure 3.5: Probability density plots for different coupling strengths with $a_1 = a_2 = 10$. a, b, and c show the probability of detecting joint intensities of I_1 and I_2 at a given time for $\xi = 0$,1 and 2 respectively. d, e, and f show the probability of detecting an intensity of I_1, after integrating over I_2 for the same values of ξ.

fluctuations in the intensity of each mode, which leads to the random switching between the two modes [45].

For a potassium MOT the Doppler broadening width is $\sim$ 1 MHz at 1 mK, which is comparable to homogeneous dephasing effects [29]. Bistable behaviour therefore may be expected for this system.

Note that this theory describes an ideal cavity with only two modes, one counterclockwise, and one clockwise. Real cavities are much more complicated than this, and contain many high order modes. These high order modes will also be coupled to the $TEM_{0,0}$ modes, with a coupling of $0 \leqslant \xi \leqslant 2$, depending on the spatial overlap, detuning, and the direction of the high order modes in comparison to the $TEM_{0,0}$ mode. In the ring cavity used here here, the most relevant low order modes are the $TEM_{1,1}$ and $TEM_{10,5}$ modes, which are

9.3 MHz and -2.7 MHz detuned from the $TEM_{0,0}$ mode respectively. The complexity of the mode structure makes quantitative analysis of their effects impossible, but qualitatively, lower than expected lasing intensities would be expected in the $TEM_{0,0}$ when the cavity is close to resonance with another mode.

3.3.1 Intensity Histogram

In order to investigate the inter mode dynamics of the system, a histogram of the lasing intensity into the CCW mode was produced. The similarity to Figure 3.5d,e or f will then give information about ξ for the system. In this measurement the laser output light was viewed on the APD with no attenuation. This ensures the effect of the shot noise is eliminated as the number of photons detected on the APD is much larger than can be detected on the photon counter, for their normal working power. However, the APD output is acquired on an oscilloscope (Agilent DSO-X 3014A), which records 2000 data points in a single trace. Ten traces were therefore acquired, and stitched together in order to make give enough data to calculate clean statistics. The time resolution was 25 μs, which gives 0.5 s of data. The power was then binned with a width of 0.35 nW. The resulting histogram is shown in Figure 3.6, alongside a fit of the form of Equation 3.21.

The agreement with theory demonstrated here is good, suggesting the laser behaves in a bistable manner, and showing that the two lasing modes are strongly coupled, with $\xi \approx 2$. However, the lasing parameters extracted from the fit were $a_1 = 7.70 \pm 0.05$, $a_2 = 7.50 \pm 0.05$. These parameters being different suggests there is some degree of non-reciprocity in the system, which will be investigated further in Section 3.4. In addition, the histogram in Figure 3.6 could be obtained from a pulsing laser rather than a bistable laser. In order to prove bistability, it should be demonstrated that only one mode is lasing at a given time. This can be done via a cross correlation measurement.

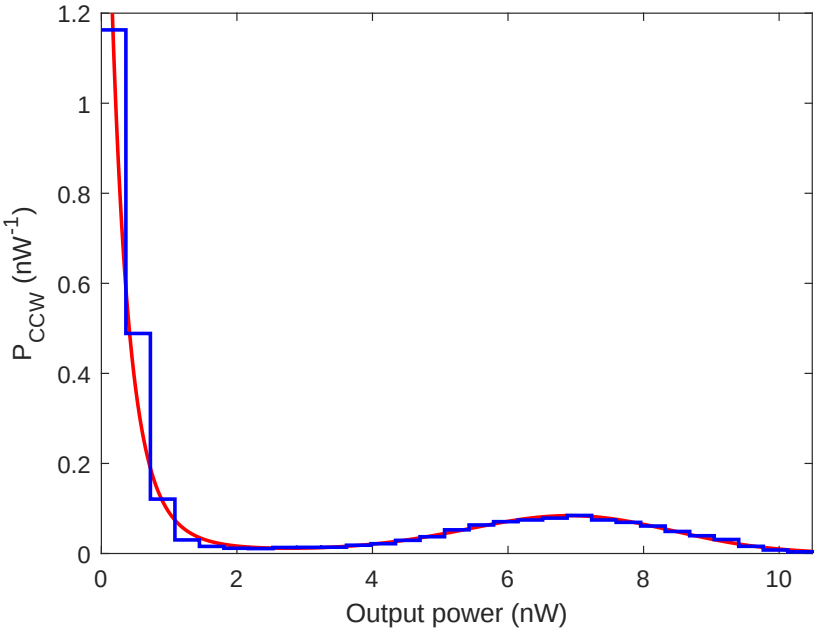

Figure 3.6: Histogram showing the probability density of lasing with a given power in the CCW cavity mode. The blue line shows the experimental data, binned into discrete 0.35 nW bins, and the red line shows a fit to the experimental data with the form of Equation 3.21.

3.3.2 Cross Correlation

The cross correlation gives the relative probability of detecting a photon in a given mode at time $t+\tau$ if a photon has been detected in the other mode at time t. A cross correlation of 0 signifies if a photon is detected in the CW mode, then there is no probability of detecting a photon in the CCW mode, whereas a cross correlation of 1, signifies that detecting a photon in the CW mode has no effect on the probability of detecting a photon in the CCW mode. If the laser is bistable, the cross correlation should be much less than one for $\tau = 0$, and equal to one at $\tau \to \infty$. The transition between the two values depends on how the switching behaves. For example, if the switching has some well defined frequency, the cross correlation should oscillate between 0 and 2, and eventually damp to one. If the switching is random, the cross correlation should tend quickly to one, with a time constant given by the residence

time of the laser.

To make a cross correlation measurement, each mode was coupled into a single mode fibre to remove higher order modes, which were then coupled into two SPCM such that each SPCM measured the intensity of one of the two $TEM_{0,0}$ modes of the cavity. The MOT was loaded and moved into the cavity mode such that the two modes were as symmetrical as possible. To calculate the cross correlation, the same algorithm that was used to calculate the $g^{(2)}$ for fluorescence was used, except $t_{bin} = 10$ μs, rather than 5 ns as in the $g^{(2)}$ measurement. This is because the bistability timescale is much longer than the coherence time, meaning that less time resolution is needed in order to resolve the features. In addition, a longer t_{bin} means that there are more counts per bin and fewer empty bins, which reduces the noise, and the processing is less computationally expensive because the histograms which are correlated are shorter.

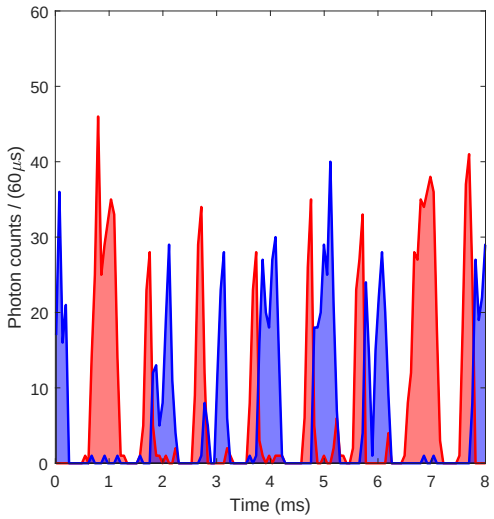

(a) Pulsed bistable lasing

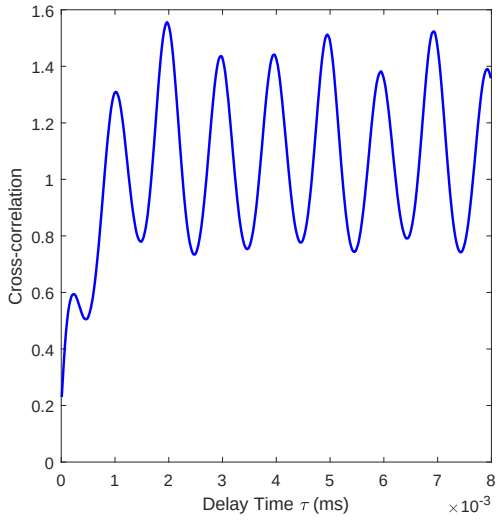

(b) Cross correlation of data similar to that shown in Figure 3.7a

Figure 3.7: Intensity and Cross correlation for the steady state mot using the tightly locked MOT laser. The blue trace is counts from the CW mode, and the red trace is from the CCW mode. A pulsing at $\sim$ 1kHz is present in the lasing intensity, which manifests itself as a 1 khz oscillation in the cross correlation.

A preliminary cross correlation measurement is shown in Figure 3.7b. Figure 3.7a is a short subsection of the intensities used to produce it. Several minutes of photon count traces are used to produce Figure 3.7b. This reveals that the cross correlation at $\tau = 0$ is 0.23, indicating that while lasing into one mode does suppress the other mode, this suppression is only partial and lasing into both modes is sometimes observed. In addition to this, a pulsing at ~ 1 kHz is observed in both the cross-correlation and intensity figures. This oscillation was unexpected and could potentially have had two causes. Either it is an intrinsic phenomenon caused by the atoms behaving as a saturable absorber or some similar effect[46], or it could be a result of technical noise causing the gain to oscillate above and below threshold. To investigate this further, and to confirm that the bistability is associated with the lasing, the system was brought below threshold by lowering the MOT beam intensity. The intensity as a function of time below threshold is shown in Figure 3.8. It should be noted that while the units are the same on the y-axis in figures 3.7a and 3.8, a neutral density filter has been removed between the measurements, so the y-axes are not comparable. A 1 kHz oscillation is

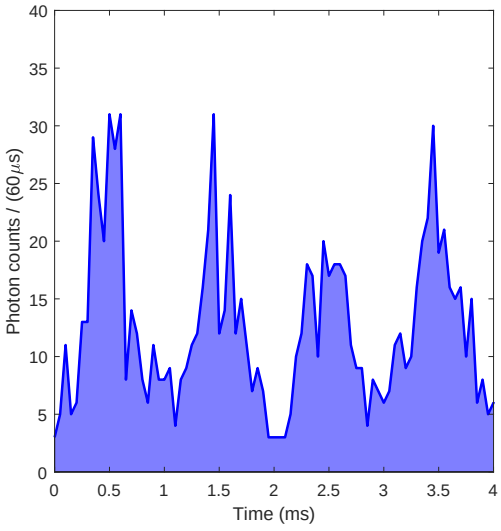

Figure 3.8: Intensity of the output of one cavity mode below threshold

clearly present in Figure 3.8, which suggests that the pulsing is due to technical noise rather

than lasing. This technical noise is attributed to intensity noise on the laser which is added when the laser is locked. The MOT laser frequency is controlled in two ways: the diffraction grating inside the laser can be moved, and the current can be changed. Both these methods have limitations. Moving the diffraction grating is limited by the mechanical resonances of the laser. If the grating is moved too quickly, the grating arm will oscillate, causing the frequency to oscillate as well. The mechanical resonance frequency for the MOT laser was measured to be ~ 1 kHz by tapping the laser case and looking at the Fourier transform of the error signal. The current can be changed much more quickly, as this cannot excite the resonance, but changing the current also affects the output power of the laser. For this reason, when locking the laser, the I branch of the servo controls the low frequency noise using the grating, and the P branch controls the higher frequency noise using the current. In this case, the gain and bandwidth of the I branch was set too high, which caused oscillations at the resonance frequency of the laser. The P branch then compensated for these oscillations, meaning the frequency was well controlled, but the intensity oscillated. To get rid of this effect, the gain and bandwidth of the I branch was lowered. This removed most of the intensity noise at 1kHz, at the expense of increased frequency noise of the MOT laser. The measurements shown in Figure 3.7 were then retaken and are shown in Figure 3.9.

The pulsing can be seen to have disappeared, proving that it was caused by technical noise. In addition the zero delay cross correlation is also significantly reduced to 0.045, indicating a much clearer bistability. This trace also indicates that the power in each lasing mode is roughly the same, so that the total output power of the laser is approximately constant. In this trace the average photon count rate is 39/60 μs^{-1}, which gives a shot noise standard deviation of 6.3, comparable to the fast intensity noise on Figure 3.9a. A function of the form $1 - Ae^{-\frac{\tau}{\tau_A}} + Be^{-\frac{\tau}{\tau_B}}$ was fitted to the cross correlation measurement, which gives a very good fit with $\tau_A = 0.6$ ms and $\tau_B = 4$ ms. This is the same functional form that was found in earlier experiments using semiconductor ring lasers, which gives evidence that the physics of the bi-stability is well understood by earlier theory [47, 48], which considered the phase-space

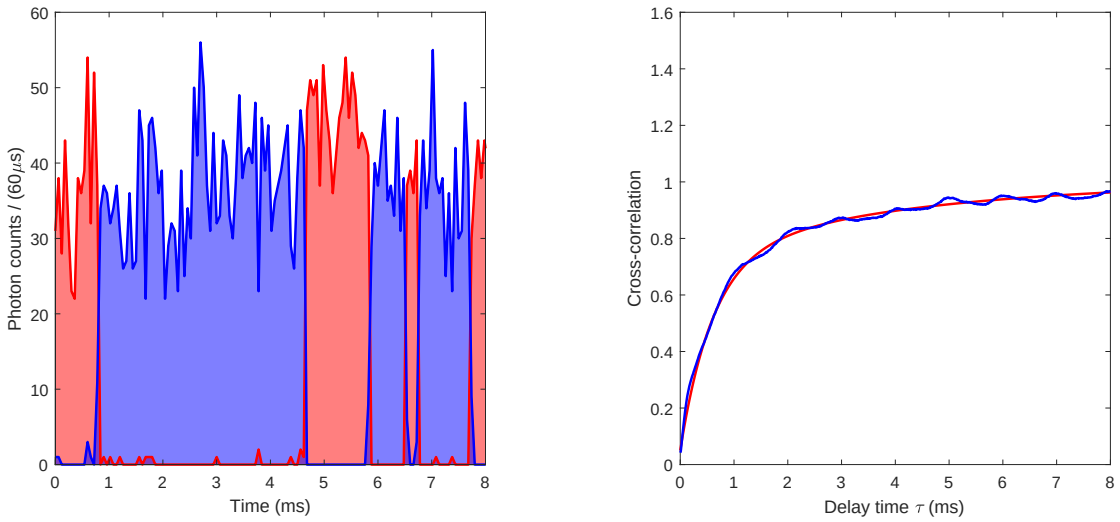

(a) Bistable lasing

(b) Cross correlation of Figure 3.9a

Figure 3.9: Intensity and Cross correlation for the steady state MOT using more loosely locked MOT laser. The lasing is seen to be much more stable compared to Figure 3.7, although some oscillation is still present.

topology of a ring laser. In this model, the two timescales are features of the stable paths in the phase space, and are not associated with the timescales of the noise itself. The long timescale represents a noise induced transition between two stable, unidirectional paths in the phase space, whereas the short timescale represents an orbit in the phase space with intrinsic switching. However, the magnitude of the two switching times are significantly different from what was observed in [47], which were of the order of 10 ns for the short timescale switching and 1 ms for the long timescale switching. This difference is unsurprising, given the large difference in operating conditions between the semiconductor lasers used in [47] and the cold atom laser demonstrated here.

3.4 Non-Reciprocity

3.4.1 Theory

Phenomenologically, non-reciprocity can be introduced into a lasing system by allowing a different pump parameter i.e. $a_1 \neq a_2$ in Equation 3.19. Solving Equations 3.20 and 3.21 with a 5% difference in a_1 and a_2 gives 3.10. The qualitative behaviour for the asymmetric

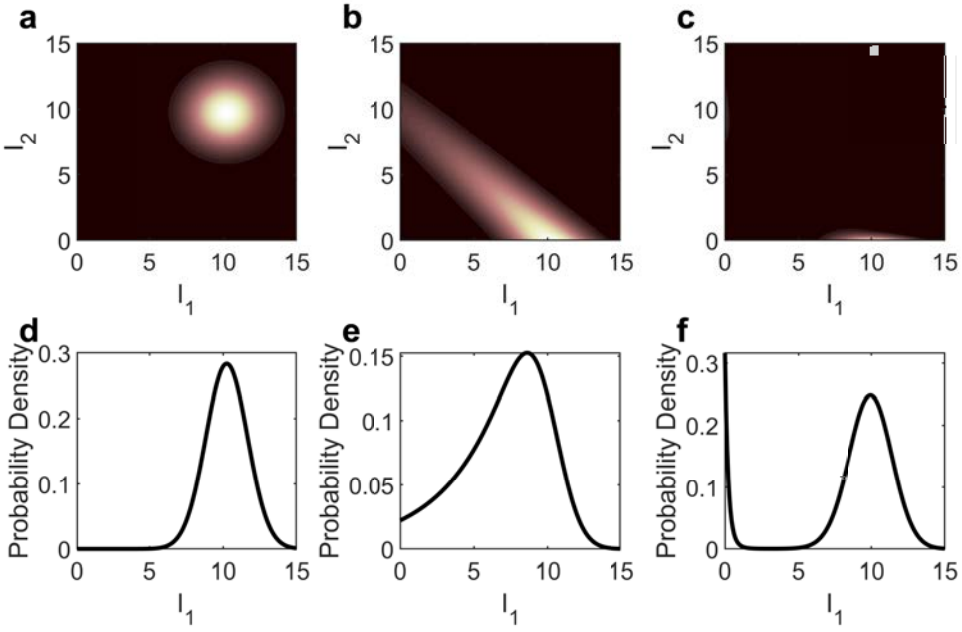

Figure 3.10: Probability density plots for different coupling strengths with $a_1 = 10.25, a_2 = 9.75$. Other parameters are the same as in Figure 3.5.

and the symmetric case is similar for each coupling strength, but large quantitative differences are observed for $\xi = 1$ and $\xi = 2$. The $\xi = 0$ result is approximately unchanged. For example, in the case where both $a_1 = a_2$, the average intensity of mode 1 and mode 2 is the same for all coupling strengths. However with the 5% asymmetry between a_1 and a_2, 51% of the power is in mode 1 for $\xi = 0$, 70% for $\xi = 1$, and 90% for $\xi = 2$. This higher power difference for stronger coupling strengths can be interpreted in terms of competition between modes.

In the coupled cases, each mode saturates the other, so an increased intensity in one mode causes suppression of the other mode. For $\xi > 1$, each mode saturates the other mode more strongly than it does itself. As this system has been demonstrated to operate in this regime, any small asymmetry in pumping power between modes should be expected to give large power variations in the output power.

3.4.2 Experiment

In order to investigate any asymmetry, the cavity length was scanned very slowly across the lasing, and the intensity of the $TEM_{0,0}$ was measured on the APD. The cavity scan had to be slow to ensure that each data point was averaged over the bistable switching, and to ensure that analysis of the switching could be performed in a region of approximately constant cavity length. A scan time of 20 s was found to give a good compromise between these advantages and reducing the slow noise caused by the MOT laser intensity drifting. The cavity scan was controlled by locking each laser and both cavities, and scanning the frequency of the AOM between the 852 nm light and the transfer cavity. The servo then adjusts the frequency of the 852 nm laser to keep the light on resonance with the transfer cavity, meaning the frequency shift of the 852 nm light going to the science cavity is given by $\Delta\nu = -2\Delta\nu_{AOM}$, where the factor of two comes from the fact the AOM is double passed. The science cavity servo then adjusts the cavity length to stay on resonance with the 852 nm light. The cavity adjustment for a ring cavity is given by $\frac{-\lambda L}{c}$, which for the cavity parameters used here is -0.27 nm/MHz. Taking into account the factor of -2 from the double pass of the AOM, the cavity length sensitivity on the AOM frequency is 0.54nm/MHZ. The cavity spectrum produced from this technique is shown in Figure 3.11.

As would be expected for a cavity, lasing into the $TEM_{0,0}$ mode was only present at a particular cavity length. This cavity length is such that the phase accumulated during a round trip at the lasing frequency is a multiple of 2π. However note that the lasing frequency is not well defined, but will change to where the round trip gain is highest. The output power

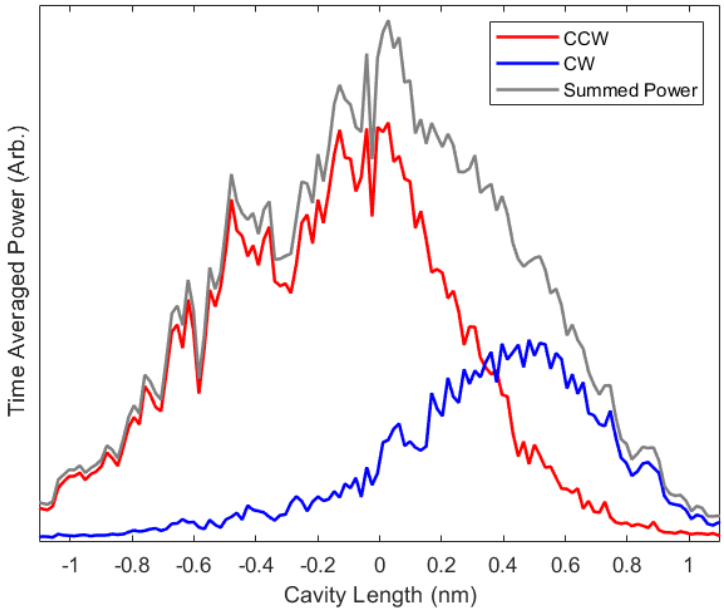

Figure 3.11: Typical spectrum produced by slowly scanning the cavity across the lasing peak.

linewidth is therefore a convolution of the gain linewidth and the cavity linewidth. As the $TEM_{0,0}$ modes in the clockwise and counterclockwise directions have exactly the same path, and therefore interact with the same atoms, it would be reasonable to assume that the lasing frequency and the cavity scan spectrum would be the same for both directions. However it can be seen from Figure 3.11 that the two directions lase into the $TEM_{0,0}$ at different cavity lengths, and have different peak intensities. There is therefore clearly some non-reciprocity between the CW and CCW modes. Note that although the CW and CCW lasing peaks are split, the total power output from the laser has a single peak. The total lasing power has a linewidth of approximately 1.2 nm of cavity displacement, corresponding to a linewidth of 5 MHz, which is approximately the gain bandwidth (investigated in Chapter 4). The linewidth of the lasing into each mode is necessarily smaller than the linewidth of the total lasing, but is of a similar order and has a value of approximately 0.8 nm of cavity displacement for both the CW and CCW directions.

3.4.3 Controlling the Non-Reciprocity

Being able to control non-reciprocity has many advantages for a ring laser, and has applications in producing narrow linewidth lasers [49], and laser gyroscopy. In particular, introducing a non-reciprocity into a ring laser gyroscope can eliminate lock in between the two modes, which is important for allowing small angular velocities to be detected [50]. The method of controlling the non-reciprocity will depend on the non-reciprocity's mechanism. Many possible sources of non-reciprocity have been found in ring lasers [22], but it is not clear which of these are relevant to the ring laser demonstrated here. Moving the MOT along the cavity axis was considered as a potential way of being able to control the non-reciprocity. There were several justifications for this: Firstly, one working theory of the source of the non-reciprocity was that the MOT was positioned to either side of the cavity waist. This would result in one direction being focused, and the other direction being defocused as it passed through the MOT. Combined with the knowledge that the MOT was providing non-linear gain to the cavity mode (which is required for lasing), this could lead to the different directions having non-identical intensities, which if combined with a non-linear refractive index, would cause each mode to lase at a different cavity length. Moving the MOT through the cavity waist by adding a variable bias field would therefore cause the sign of the non-reciprocity to reverse as the MOT was moved through the cavity waist. The other working theory for the non-reciprocity was that because of the influence of the MOT light, the MOT position is not at the position where $B = 0$. This can be thought of in terms of having an optical trap centre, which considers the complicated effect of the MOT beams, and a magnetic trap centre, which is the $B = 0$ point. When the two trap centers are in the same place, the MOT sits at the common centre. However, when the trap centres are in different places, the MOT will sit at some compromise position between the two centres. As the MOT has a constant gradient across it, the MOT will then be in a position where there is a net B field across it. This field will be counter-propagating with one direction and co-propagating with the other direction,

which could in principle lead to some non-reciprocal behaviour. A variable bias field could then be used to control the position of the magnetic trapping centre without affecting the optical trapping centre, and therefore change the net magnetic field across the MOT.

In both of these working theories, using a bias field to control the MOT position would work to control the non-reciprocity, so this was attempted. Initial attempts showed that the non-reciprocity was not dependent on the bias field, which suggested that both of the working theories described above were incorrect, however, it was realised that the position of the MOT along the cavity axis was not well known, and that the MOT could be many MOT diameters away from the centre of symmetry, which could lead to saturation of the non-reciprocity. For this reason in addition to moving the MOT with the bias field, the coils used to create the gradient were also moved in order to make large changes to the position of the B=0 point. Before and after moving the coils, images of the MOT were taken from cameras separated by $\sim 90^o$ to ensure the MOT was moved systematically along the cavity axis. To finely adjust the MOT position, the current through the shim coils was adjusted. At each MOT position, the cavity was slowly scanned as described above, and the cavity output power measured on the SPCMs. To quantify the non-reciprocity, Gaussian peaks were then fitted to each SPCM channel. The difference between the centre of these Gaussians was then used as a metric for the degree of non-reciprocity. The MOT position was measured by taking pictures of the MOT with the camera perpendicular to the MOT axis. With the MOT current at 12 A, this was 0.32 mm/A, which is similar to the calculated movement of the $B = 0$ point, which moves 0.3 mm/A. Figure 3.12 shows the splitting as a function of MOT position.

This shows that moving the MOT position has a strong influence on the non-reciprocity. In particular, it is possible to make the non-reciprocity disappear, and the sign can be controlled. The non-reciprocity saturates at a splitting of around ± 1.2 nm, or after moving the MOT 0.3 mm from the symmetric MOT position. Both of these are of a similar order of magnitude to length scales in the experiment; 0.3 mm is comparable to the MOT radius of 0.4 mm while

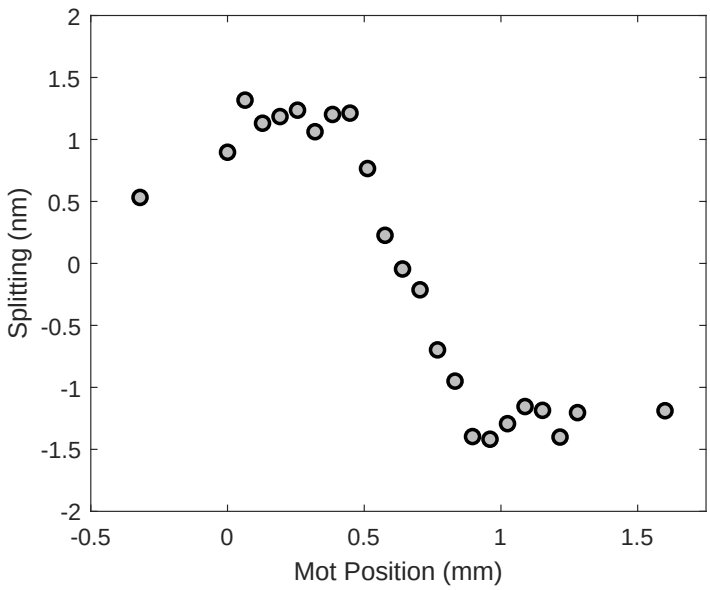

Figure 3.12: Splitting between the CW and CCW optimum lasing cavity lengths as a function of MOT position. The x-axis is referenced to the position of the MOT when no bias field is applied.

1.2 nm is the same as the FWHM of the lasing in Figure 3.11. This experiment therefore does not indicate what is causing the saturation.

3.4.4 Changing the B-field gradient

One distinction between the two possible sources of asymmetry, namely, the $B = 0$ point and the cavity waist is that the $B = 0$ point is dependent on the bias field and the gradient, which are both controllable, whereas the cavity waist is a fixed point in space. If the B-field causes the asymmetry, the point of symmetry will move if the B-field gradient is changed. Conversely, If the cavity waist causes the asymmetry, the point of symmetry will be independent of the B-field gradient. The MOT gradient current was therefore reduced from 12 A to 10 A, and the experiment represented by Figure 3.12 was repeated. This is shown in Figure 3.13.

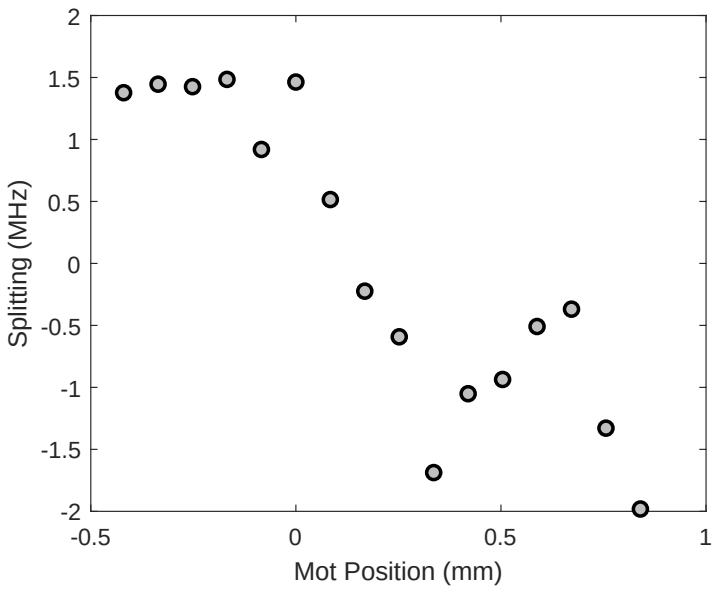

Figure 3.13: Similar to Figure 3.12, with the MOT current set to 10A.

With a MOT current of 10 A, the splitting data is significantly noisier than the previous data set because the MOT position and atom number is significantly noisier with a reduced MOT current. The MOT also moves 0.42 mm/A with the reduced gradient, which is expected, as the $B = 0$ point also is more sensitive to the bias field at lower gradients.

The MOT position that gives no splitting between the two directions is significantly different for the two different MOT gradients, suggesting the MOT being either side of the cavity waist cannot be the asymmetry responsible for the non-reciprocity.

Due to the effects of the MOT light, the MOT would be expected to be in a slightly different place for the two gradients with no shim field. This leads to the possibility that the reference MOT positions for the x-axes of Figures 3.12 and 3.13 are significantly different. To account for this, two images of the MOT were taken with the current through the cavity axis shim coils set to zero. One of the images used a current of 12A through the MOT coils and the other used a current of 10A. A comparison between them in Figure 3.14 shows that the MOT does not significantly move along the cavity axis when the MOT gradient is changed,

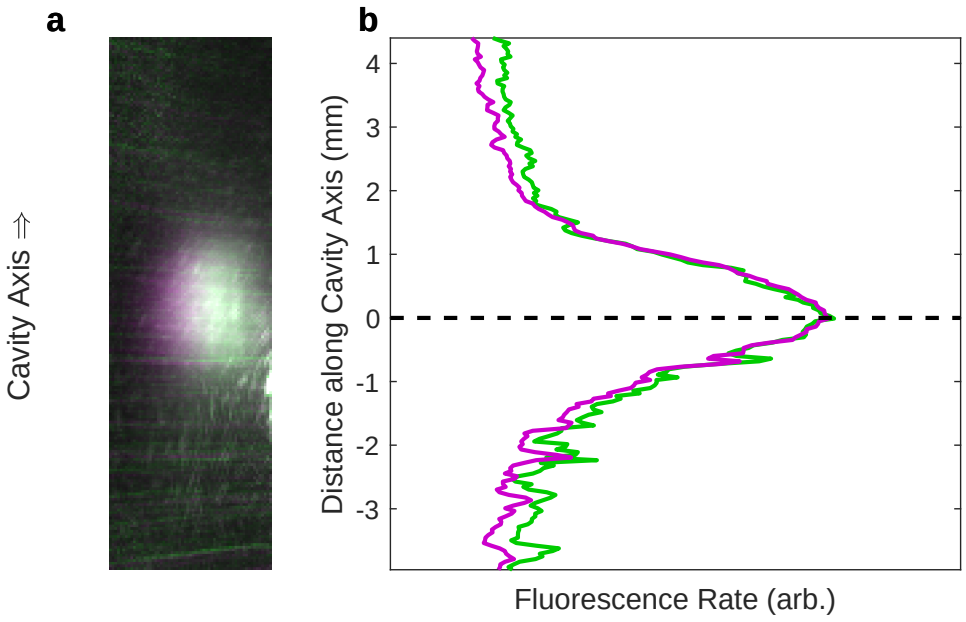

Figure 3.14: Comparison between the MOT positions for two different MOT gradients. Photographs of the MOTs are shown in **a**. The images with a MOT coil current of 12A and 10A are green and magenta respectively. **b** shows the summed counts along the horizontal direction in **a**, confirming that the MOTs are in the same position along the cavity axis.

although there is some transverse movement. This confirms that the MOT positions that give reciprocal lasing are different for different MOT gradient, which suggests that the magnetic field zero is the centre of symmetry relevant to the non-reciprocity.

3.4.5 Intensity

In previous investigations of ring lasers, optical non-linearities have been found to cause non-reciprocity between the two counter propagating directions [51]. This possibility is especially relevant, as the non-reciprocity was controlled by moving the gain medium parallel to the cavity axis, as is the case here. However, the proposed explanation was based on the short pulse length in a mode-locked laser. In the cold-atom laser, the bistability induced pulse length is $\sim$ 1 ms, which is a factor of approximately 10^{11} longer than in the mode locked laser, which suggests that it is implausible for the non-reciprocity in the cold-atom laser to have the same origin as in the mode-locked laser.

As optical non-linearities are caused by the lasing power itself, any non-reciprocity caused by the lasing would be expected to be strongly dependent on the lasing intensity. The pump power was therefore varied in order to change the output lasing power, after placing the MOT in a position where non-reciprocity could be seen with the default MOT settings. This produced Figure 3.15.

This demonstrates that the lasing output power has no apparent systematic effect on the non-reciprocity over the possible working conditions of this apparatus. Because a precise model for how a non-linearity would cause non-reciprocity has not been proposed, this measurement does not conclusively rule out a non-linearity being the cause of the effects seen here. However, non-linearities are intensity sensitive by definition, so it is unlikely that any model of producing non-reciprocity with a non-linearity could by intensity independent.

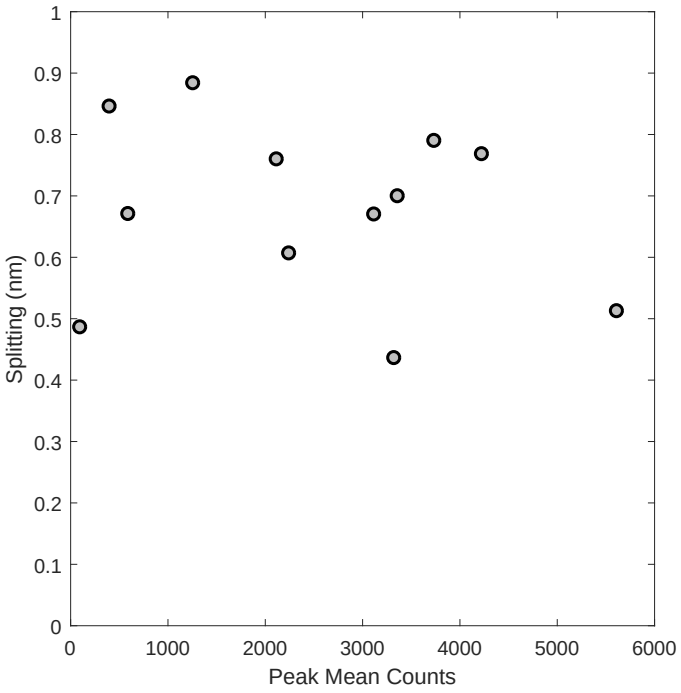

Figure 3.15: Effect on the non-reciprocity of the lasing power, which was controlled by varying the pump power. The x-axis is the average amplitude of the Gaussians fitted to the data.

3.4.6 Non-reciprocity below threshold

Although the intensity of the lasing has no effect on the non-reciprocity, if the laser is brought below threshold it behaves very differently. It is therefore possible that the non-reciprocity could behave significantly different below threshold. For example, above threshold small differences in the pump parameter for different cavity lengths would cause large difference in the output intensity due to mode competition, as shown by Figure 3.10. By looking at the system below threshold, any effects caused by mode competition will be strongly suppressed. This means that if the splitting is not observed below threshold then the non-reciprocity is strongly enhanced by mode competition when the system is lasing. The beam power was reduced such that the system was below threshold and the MOT was placed in a position where there was a strong non-reciprocity above threshold. The cavity was scanned as for the experiment represented in Figure 3.11 and the output intensity of each direction measured on

the SPCMs with no attenuation other than the losses due to imperfect fibre coupling. This measurement is shown in Figure 3.16. The peak is seen to occur at the same cavity length,

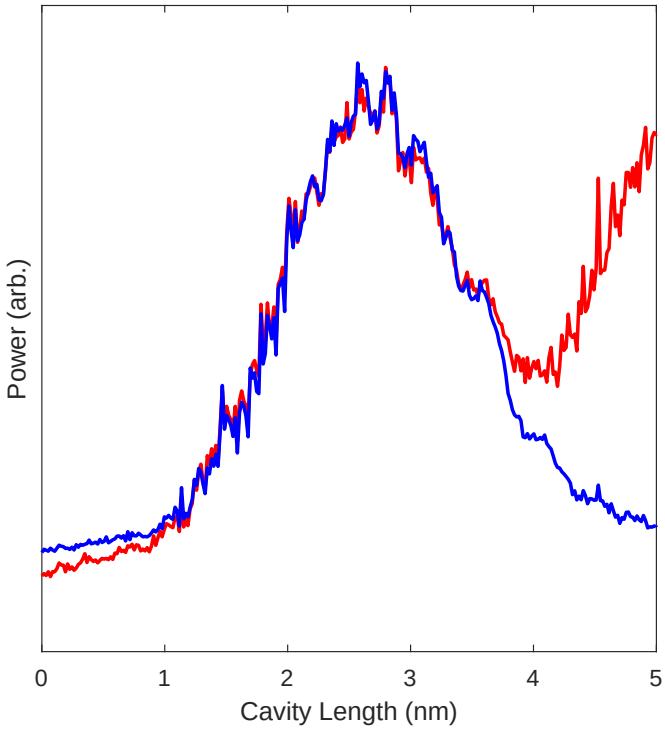

Figure 3.16: Cavity scan across the gain feature below threshold, showing that the fluorescence in each direction occurs at same cavity length.

indicating that the non-reciprocity is strongly enhanced by lasing due to mode competition between the two directions. The second peak in the CCW direction is caused by fluorescence into the TEM_{11} mode. It is visible in the CCW direction and not the CW direction because the CW coupler filters out higher order modes much more effectively due to better alignment.

This result limits the usefulness of the non-reciprocity somewhat. As the non-reciprocity is only large due to competition between counter-propagating modes, it suggests the gain is similar in both directions, meaning the two modes lase at approximately the same frequency. One This means that in a cold atom ring laser gyroscope, the non-reciprocity could probably

not be used to prevent lock-in by biasing the gyroscope.

3.4.7 Time vs Power ratios

Because Figure 3.16 suggests that lasing is caused by mode competition, and the difference in pump parameter between the two directions is small, it would be expected that the instantaneous lasing intensity would be similar for both directions, and the non-reciprocity is controlled by the relative probability of lasing into a given direction changing as the cavity or MOT position is changed.

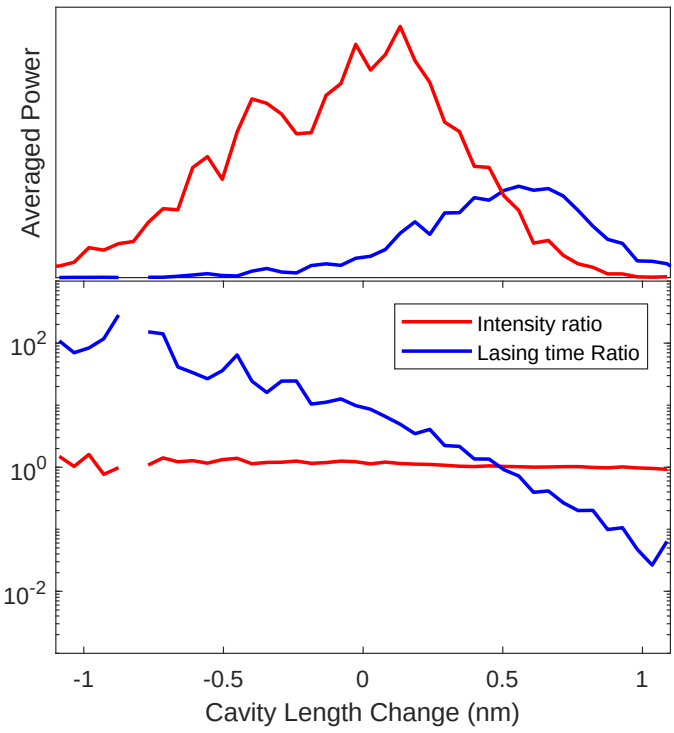

Figure 3.17: Ratios of lasing time and instantaneous lasing power for the clockwise and counterclockwise directions. The time averaged lasing power is included above for reference. The MOT position was chosen to maximise the non-reciprocity.

Each cavity scan spectrum used to produce Figure 3.12 was then split into regions of 0.2 s, corresponding to 0.05 nm. The chosen time interval gives approximately 200 switching events,

which allows for usable statistics for the lasing probability, while maintaining cavity length resolution. A threshold count rate was defined for each direction. Above this threshold, the system was said to be lasing into the relevant direction, and below the threshold the system was not lasing. This threshold was determined by looking at a figure similar to Figure 3.9a and choosing a threshold count rate well below the intensity noise, but much higher than 1. For example, a reasonable threshold would be 10 counts per 60 μs in figure 3.9a. The following results were relatively insensitive to the particular choice of threshold when this procedure was followed, demonstrating the validity of this method. The instantaneous output power was measured by averaging the power for all times where the output power was above the threshold. The ratio of the time lasing into the CCW and CW modes, and the ratio of the average instantaneous intensities while lasing was taken. The results for a trace with a strong non-reciprocity (corresponding to MOT position of 0.4 mm in Figure 3.12) are shown in shown in Figure 3.17.

The lasing time ratio can be seen to vary over a range of $\sim 10^4$ over this scan, while the instantaneous lasing power ratio is approximately constant. The variation in lasing intensity is therefore almost entirely determined by the time lasing into each mode. This supports the conclusion that the non-reciprocity is dominated by competition between the lasing modes, rather than each lasing direction having a different pump parameter. The equal time cavity length is around 0.5 nm longer than the peak lasing power cavity length. One possible reason for this is the presence of the high order modes at a longer cavity length competes with the $TEM_{0,0}$ mode for gain, which could cause the intensity in the $TEM_{0,0}$ to be lower for longer cavity lengths. Another way of studying the non-reciprocity is to look at the time spent lasing into each mode at a given cavity length for each MOT position, rather than the splitting, as the splitting does not relate directly to the pump parameter. When the MOT was moved parallel to the cavity axis the atom number changed which caused the total phase accumulated by the cavity light to change. This in turn meant that lasing occurred at slightly different cavity lengths for each MOT position. The cavity scans were therefore

pre-processed by fitting a Gaussian to sum of the lasing power in both directions. The centre of this Gaussian was then used as a reference cavity length, to allow comparison between different spectra. The probability of lasing into the CCW direction as a function of MOT position is shown in Figure 3.18d. As a guide for the eye, the theory from Equation 3.21 is plotted, assuming a linear change in $\Delta_a = a_1 - a_2$ with MOT position.

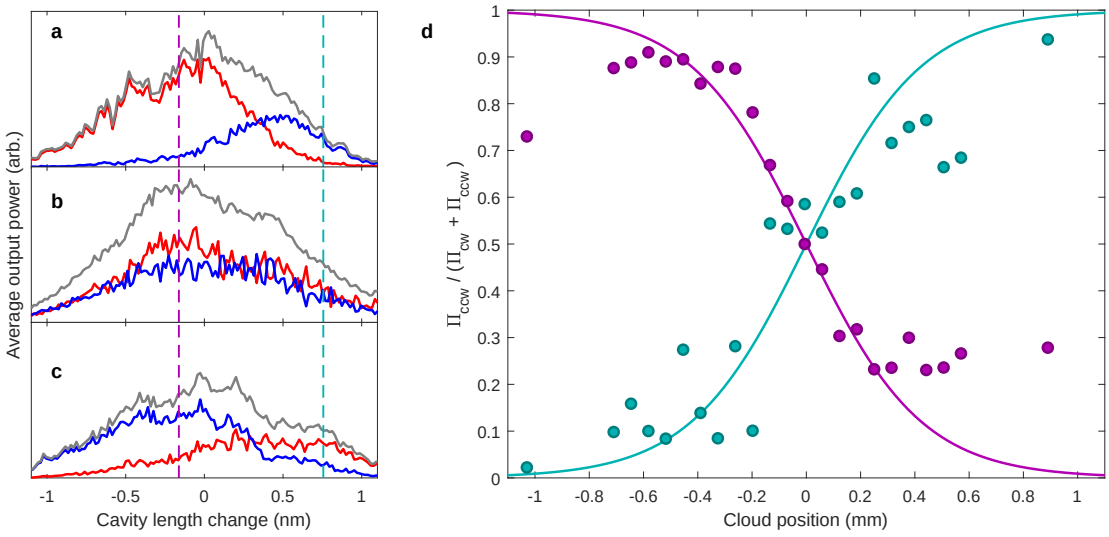

Figure 3.18: a, b, and c show data from slow cavity scans across the $TEM_{0,0}$ lasing peak for different MOT positions, as in Figure 3.11. d shows the fractional time spent lasing into the counterclockwise mode as a function of MOT position. The cyan and magenta points correspond to the cavity length shown by the lines of the same colour in a, b, and c. The data at cloud positions of -0.7mm, 0 mm, and 0.6 mm correspond to a,b, and c respectively. The solid lines in d correspond to theory from Equation 3.21, assuming a linear change in Δa with MOT position.

This analysis gives relatively good agreement with the theory and the assumption of Δa being linear with cavity length. The main deviation from the expected result is the magenta curve, representing the non-reciprocity as a function of cloud position, does not match well for positive cloud positions. The cause of this is not known, and more data is required to conclude how Δa changes with the MOT position.

3.5 Conclusion

A standard potassium-39 MOT has been demonstrated to lase when coupled with a high finesse cavity, evidenced by a threshold curve and $g^{(2)}(0)$ measurement. In addition, the system has been shown to demonstrate bistable behaviour due to the coupling between the CW and CCW modes, which is mediated by homogeneously broadened gain. This bistability enhances a non-reciprocity caused by the MOT position being off centre with respect to the B-field zero. The exact mechanism of this non-reciprocity is not yet known, but has been shown to be dependent on the B-field gradient. This is a promising avenue for future research.

CHAPTER 4

GAIN MECHANISM IN A POTASSIUM MOT

Several gain mechanisms have been observed in MOTs with different species in the past. Mollow gain[12, 52] has been observed in caesium [53] and rubidium [54] and Raman gain between Zeeman levels [11] has been observed in potassium. These two gain mechanisms are particularly notable because they can give net gain with no additional pump beams. Other gain mechanisms have also been reported with the addition of extra pump beams. Four-wave mixing [15] and Raman gain between hyperfine states [19] in rubidium, and Raman gain between excited states in ytterbium [16] have all been used to make cold atom lasers with an additional pump beam. However, to the author's knowledge, gain in a potassium MOT has never been reported in the literature. The small hyperfine splitting of potassium-39 means that the MOT works under significantly different conditions than a rubidium or caesium MOT, which allows hyperfine Raman gain to be present, without the addition of any pump beams.

In this chapter a theoretical explanation of Mollow gain and hyperfine Raman gain are given. These are the viable gain mechanisms which can resemble the observed gain. Numerical models of these processes are then described. After this, experimental results are presented, which demonstrate that a near resonance Raman process is responsible for the observed gain. Parts of this chapter are taken from [55].

4.1 Dressed Atom Theory for a Two-Level Atom

In order to understand the frequency of the gain and the gain mechanism that is observed we will look at the Jaynes-Cummings model of light-atom interaction. This describes the interaction between a quantum light field (an optical cavity) and an atom. We start by assuming that the interaction between the cavity and the atom is dominated by the dipole interaction. This gives the interaction Hamiltonian as

$$H_I = -\hat{d}.\hat{E}(t) \tag{4.1}$$

$$= -\hat{d}g(a + a^\dagger) \tag{4.2}$$

where

$$g = \left(\frac{\hbar\omega}{2\epsilon_0 V}\right)^{\frac{1}{2}}, \tag{4.3}$$

where ω is the optical frequency, V is the cavity mode volume and a is the cavity lowering operator. g is found to be of this form by equating the energy of a photon to the energy found by integrating the electric field over the cavity mode volume. Defining

$$\sigma^\dagger = |e\rangle \langle g| \tag{4.4}$$

$$\sigma = |g\rangle \langle e| \tag{4.5}$$

$$\sigma_3 = |e\rangle \langle e| - |g\rangle \langle g| \tag{4.6}$$

$$d = \langle e| \hat{d} |g\rangle \tag{4.7}$$

we get

$$\hat{d} = d(\sigma^\dagger + \sigma) \tag{4.8}$$

which leads to the interaction Hamiltonian in a more useful form:

$$H_I = -dg(\sigma^\dagger + \sigma)(a^\dagger + a) \tag{4.9}$$

We define the energy zero to be halfway between the ground and excited states of the atom with no photons in the cavity. This gives the full Hamiltonian as

$$H = \frac{1}{2}\hbar\omega_0\sigma_3 + \hbar\omega a^\dagger a - dg(\sigma^\dagger + \sigma)(a^\dagger + a) \tag{4.10}$$

where ω and ω_0 are the cavity and atomic resonance frequencies respectively. Now we use the rotating wave approximation to simplify this. The time dependence of a and σ can be approximated as

$$a = a(0)e^{-i\omega t} \tag{4.11}$$

$$\sigma = \sigma(0)e^{-i\omega_0 t} \tag{4.12}$$

in the limit of weak coupling. When we integrate the Schrödinger equation, each term will be divided by the frequency it is oscillating at. This means any terms that oscillate at optical frequencies will be negligible compared to slowly oscillating terms. The σa and $\sigma^\dagger a^\dagger$ terms oscillate at optical frequencies, giving the Hamiltonian in the rotating wave approximation as

$$H = \frac{1}{2}\hbar\omega_0\sigma_3 + \hbar\omega a^\dagger a - dg(\sigma^\dagger a + \sigma a^\dagger) \tag{4.13}$$

We define the total excitation number as $N = |e\rangle\langle e| + a^\dagger a$. Note that this commutes with the Hamiltonian, and is therefore conserved. We can then choose a subspace where $N = n + 1$, and the system will not evolve out of this subspace. It therefore makes sense to work in a basis that recognizes the conservation of excitation. This basis is $|e, n\rangle$ and $|g, n + 1\rangle$, where the first state represents an extra excitation in the atom and the second state represents an extra excitation in the cavity. In this is basis the Hamiltonian becomes,

in matrix form,

$$H = \begin{pmatrix} \hbar\omega n + \frac{\hbar\omega_0}{2} & -gd\sqrt{n+1} \\ -gd\sqrt{n+1} & \hbar\omega(n+1) - \frac{\hbar\omega_0}{2} \end{pmatrix} \tag{4.14}$$

$$= \begin{pmatrix} \hbar\omega(n+\frac{1}{2}) + \frac{\hbar\Delta}{2} & -gd\sqrt{n+1} \\ -gd\sqrt{n+1} & \hbar\omega(n+\frac{1}{2}) - \frac{\hbar\Delta}{2} \end{pmatrix} \tag{4.15}$$

where $\Delta = \omega_0 - \omega$. The eigenvalues of this Hamiltonian are

$$E_{\pm}(n) = (n + \frac{1}{2})\hbar\omega \pm \frac{\hbar\Omega'_n(\Delta)}{2} \tag{4.16}$$

where $\Omega'_n(\Delta) = [\Delta^2 + \Omega^2]^{\frac{1}{2}}$, $\Omega^2 = 4\lambda^2(n+1)$, and $\lambda = \frac{gd}{\hbar}$. Ω' is known as the generalised Rabi frequency, and gives the effective Rabi frequency for detuned light. Ω is the resonant Rabi frequency. The eigenstates associated with this Hamiltonian can be written as

$$\begin{aligned} |n+1,+\rangle &= \cos\left(\frac{\phi}{2}\right)|e,n\rangle + \sin\left(\frac{\phi}{2}\right)|g,n+1\rangle \\ |n+1,-\rangle &= \cos\left(\frac{\phi}{2}\right)|g,n+1\rangle - \sin\left(\frac{\phi}{2}\right)|e,n\rangle \end{aligned} \tag{4.17}$$

where the $|n+1,\pm\rangle$ represents the dressed state. The first term in the ket labels the excitation number, and the second term labels the sign of the second term of its energy eigenvalue.

The angles are defined as

$$\phi = \tan^{-1}\left(\frac{\Omega}{\Delta}\right), \tag{4.18}$$

$$\cos\left(\frac{\phi}{2}\right) = \frac{1}{\sqrt{2}}\left(1 + \frac{\Delta}{\Omega_n'(\Delta)}\right)^{\frac{1}{2}}, \tag{4.19}$$

$$\sin\left(\frac{\phi}{2}\right) = \frac{1}{\sqrt{2}}\left(1 - \frac{\Delta}{\Omega_n'(\Delta)}\right)^{\frac{1}{2}}. \tag{4.20}$$

For a red-detuned optical field, Δ is positive, which by inspection of Equation 4.20, means that the higher energy $|+\rangle$ state contains more excited state than ground state, and the $|-\rangle$ state contains more ground state than excited state.

4.1.1 AC Stark Effect

The AC Stark effect is the shift in the transition frequency due to the interaction of light with an atom. From Equation 4.20, for red-detuned light we can associate the $|+\rangle$ state with the excited state and the $|-\rangle$ state with the excited state [56]. Note that this approximation is good in the far detuned case, but breaks down when $\Omega \approx \Delta$, as the dressed states contain significant populations of both states. Equation 4.16 gives the splitting between the $|+\rangle$ and $|-\rangle$ states due to the interaction with the light state as $\hbar\Omega'$. We want to calculate the effect on the atoms, so we remove the energy only associated with changing the light frequency by subtracting $\hbar\Delta$. This gives a formula for the change in energy of a transition due to an applied field as

$$\delta E_t = \hbar(\Delta^2 + \Omega^2)^{\frac{1}{2}} - \hbar\Delta \tag{4.21}$$

In the limit that $\Delta >> \Omega$, i.e. for large detuning, this can be Taylor expanded with respect to Ω as

$$\delta E_t = 0 + \frac{\Omega^2}{2\Delta} - \frac{\Omega^4}{8\Delta^3} + ... \tag{4.22}$$

The first non-zero term of the expansion is the normal expression for the far-detuned Stark shift, and the second non-zero term shows that this approximation overestimates the Stark shift for smaller detunings. As the ground and excited states are treated symmetrically in the Jaynes-Cummings model, the shift in the transition must be half from a shift in the ground state, and half from a shift in the excited state. This gives that the magnitude of the shift in each state must be half the shift of the transition. The change in the ground state must also have the opposite sign to the change in the total transition, as the transition energy is $E_e - E_g$. This leads to the Stark shift of each state as

$$\delta E_s \approx \frac{\Omega^2}{4\Delta} \tag{4.23}$$

$$\delta E_g \approx -\frac{\Omega^2}{4\Delta} \tag{4.24}$$

4.1.2 Mollow Gain

Another effect that follows from this theory is Mollow gain. The dipole matrix element between two dressed states determines whether a transition between them is possible. Noting that terms of the form $\langle n_1, \pm| \hat{d} |n_2, \pm\rangle$ are zero if the signs of the states are the same or $n_1 \neq n_2 \pm 1$, the dipole matrix element between the $|n, +\rangle$ and $|n+1, -\rangle$ is given by,

$$\langle n, +| \hat{d} |n+1, -\rangle = \sin^2\left(\frac{\phi}{2}\right) \langle g, n| \hat{d} |e, n\rangle = d \sin^2\left(\frac{\phi}{2}\right). \tag{4.25}$$

which is non-zero, meaning that a transition between these states is allowed. Spontaneous emission into the ground state causes the dressed eigenstates which contains more ground state to be more populated than the excited states. For the case of red-detuning, this leads to the $|-\rangle$ states becoming more populated. A population inversion therefore exists between the $|n, +\rangle$, and the $|n+1, -\rangle$, which means that gain, rather than absorption would be observed on this transition. In the far detuned states, the inverted states approximate eigenstates of the uncoupled system: $|n+1, -\rangle \approx |g, n+1\rangle$ and $|n, +\rangle \approx |e, n-1\rangle$. This leads to the

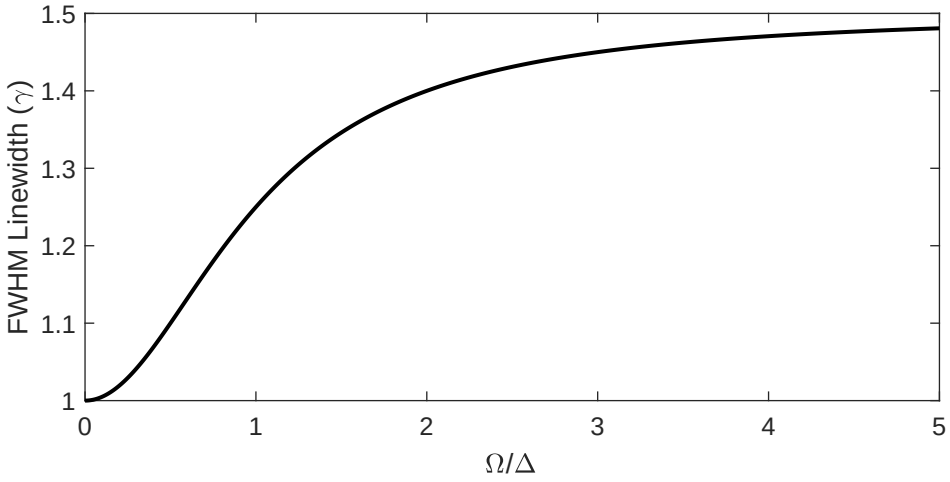

Figure 4.1: The linewidth of a Mollow gain feature. The feature gets broader with increasing Ω/Δ, but is limited to 1.5γ.

common interpretation that in the far-detuned case, Mollow gain corresponds to absorbing two photons from the pump field, exciting the atom, and emitting one photon by stimulated emission.

Further analysis of the dressed atom picture in [53] gives approximate linewidths of the gain feature in the limit of large detuning as

$$\gamma_m = \gamma(1 + 2\sin^2(\theta)cos^2(\theta)) \tag{4.26}$$

and the frequency as

$$\omega_m = \omega \pm (\Omega^2 + \Delta^2)^{\frac{1}{2}} \tag{4.27}$$

where $\theta = 1/2\tan^{-1}(\Omega/\Delta)$. As θ tends towards $\pi/4$ for large Ω, this implies that γ_m ranges between γ and 1.5γ. This is shown in Figure 4.1. The frequency of the gain feature follows the frequency of the transition between the two relevant dressed states, and so is seperated from the pump beam by Ω', the generalised Rabi frequency.

While this picture is good for intuitively understanding the gain mechanism, a more

detailed picture can be obtained by solving the optical Bloch Equations. This leads to an equation for the absorption coefficient, normalised to the dark, on-resonance absorption as [15],

$$\alpha = \frac{\gamma}{2}\frac{|z|^2}{|z|^2+\Omega^2/2}\mathrm{Re}\left[\frac{(\gamma+i\delta)(z+i\delta)-i\Omega^2\delta/(2z)}{(\gamma+i\delta)(z+i\delta)(z^*+i\delta)+\Omega^2(\Delta/2+i\delta)}\right], \tag{4.28}$$

where γ is the FWHM natural linewidth, δ is the probe-atom detuning, and $z = \gamma/2 - i\Delta$. This equation gives a full description of the absorption spectrum, and is included primarily for completeness, as Mollow gain can be conceptually understood better through the dressed-atom picture and quantitatively calculated numerically.

4.2 Raman Gain in Cold Atoms

Raman gain between hyperfine ground states is an alternative possible gain mechanism in Cold atoms, which has also recently been used for making a cold atom laser in rubidium [19].

This gain mechanism requires a three-level atom, with two ground states and one excited state and involves the absorption of a pump photon, the stimulated emission of a probe photon, and the transfer of population between the two ground states. This is shown schematically in Figure 4.2.

The ground state approximately resonant with the pump beam is labelled $|g_1\rangle$ and the other ground state is labelled $|g_2\rangle$. The $|g_1\rangle \rightarrow |g_2\rangle$ transition is dipole forbidden but both $|g_{1,2}\rangle \rightarrow |e\rangle$ are dipole allowed. The $|g_1\rangle$ state is dressed by the pump beam, whereas the $|g_2\rangle$ state is approximately unaffected by the pump beam. From Equations 4.17, the dressed basis is

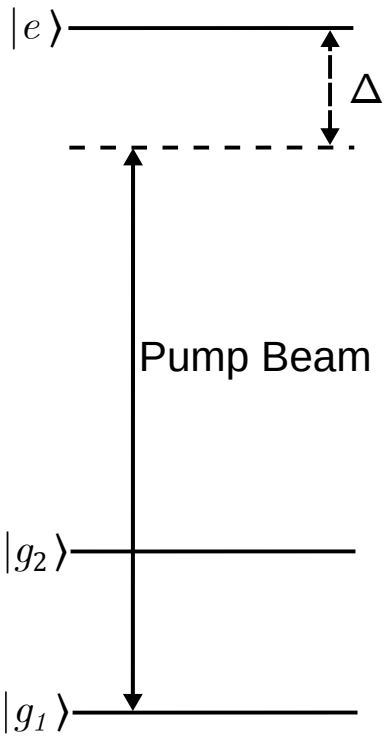

Figure 4.2: Energy level diagram of a simple three-level system capable of Raman gain.

$$|n+1,+\rangle = \cos\left(\frac{\phi}{2}\right)|e,n\rangle + \sin\left(\frac{\phi}{2}\right)|g_1,n+1\rangle \tag{4.29}$$

$$|n+1,-\rangle = \cos\left(\frac{\phi}{2}\right)|g_1,n+1\rangle - \sin\left(\frac{\phi}{2}\right)|e,n\rangle \tag{4.30}$$

$$|n,g_2\rangle = |g_2,n\rangle \tag{4.31}$$

Note for the uncoupled $|g_2\rangle$ state, we have chosen an eigenstate with a lower excitation number than the dressed states because there is no coupling between the $|n+1,g_2\rangle$ state and the dressed states. We can then calculate the dipole matrix elements between the dressed states

as

$$\langle n, g_2 | \, \hat{d} \, | n+1, + \rangle = \cos\left(\frac{\phi}{2}\right) \langle e, n | \, \hat{d} \, | g_2, n \rangle \tag{4.32}$$

$$\langle n, g_2 | \, \hat{d} \, | n+1, - \rangle = -\sin\left(\frac{\phi}{2}\right) \langle e, n | \, \hat{d} \, | g_2, n \rangle \tag{4.33}$$

which are non-zero, demonstrating that transitions between the dressed states are possible. In the far red-detuned case, $\cos\left(\frac{\phi}{2}\right) \approx 1$, which means $|n+1, +\rangle$ becomes approximately the excited state. This means that Equation 4.32 tends to the undressed $|g_2\rangle \rightarrow |e\rangle$ dipole matrix element. $|n+1, -\rangle$ becomes approximately the $|g_1\rangle$ state, but has a non-zero matrix element given by Equation 4.33. This means the effect of the dressing light is to allow a weak transition between the ground states. This is known as a Raman transition. For a far detuned beam, the dipole moment associated with the Raman transition is given by

$$d_{raman} = -\sin(\phi) \langle e, n | \, \hat{d} \, | g_2, n \rangle \approx \langle e, n | \, \hat{d} \, | g_2, n \rangle \, \frac{-\Omega}{2\Delta}, \tag{4.34}$$

meaning the Raman transition strength is inversely proportional to the detuning. The Rabi frequency of a probe interacting with this transition is therefore given by

$$\Omega_{Raman} = \frac{\Omega_p \Omega}{2\Delta} \tag{4.35}$$

where Ω_p is the Rabi frequency of the probe and the $|g_2\rangle \rightarrow |e\rangle$ transition. Note that for a blue-detuned pump, the physics is identical, except the $|+\rangle$ state becomes the ground state and is associated with the Raman transition, and the $|-\rangle$ state becomes the excited state and is associated with the normal transition. If a probe is approximately resonant with the raman transition then either gain or loss will be observed depending on the relative populations on the ground states. If the $|g_2\rangle$ state is more populated, then a net loss will be observed, but if the $|g_1\rangle$ state is more populated, the raman transition will appear as gain.

The populations of the ground states in a MOT are determined by the rate of optical

pumping by the cooling and repump beams, which depends on the beams' power and detuning. These parameters can be controlled in the MOT, which allows the possibility of controlling the steady state gain by controlling the MOT populations. However, changing the MOT parameters would also change the dipole moment of the Raman transition. This is non-trivial to calculate due the presence of multiple excited states so a more detailed, multilevel calculation is required to calculate how the MOT parameters affect the gain.

4.3 Effective Dipole Moment

For a multilevel atom, it is important to be able to calculate the effective dipole moment, which will in general be different for each transition. The effective Rabi frequency, $\Omega_n = \frac{2d_n.E}{\hbar}$, as well as the absorption of a resonant probe, will depend on the exact transition and the polarisation of the light, as the dipole moment is dependent on these factors. One way to calculate the effective Rabi frequency would therefore be to calculate d_n directly for each state and polarisation. However, a more natural way is to use the saturation intensity, I_s which is an easily measurable and intuitively simple parameter. For a non-degenerate two-level system, the saturation intensity is defined as the steady state intensity that reduces the absorption of a feature by a factor of two compared to the weak probe case. This occurs when the population the excited state fraction is one quarter, as the population difference between the excited and ground states is halved. Solving the Lindblad master equation (Equation 4.44) for these populations, which is equivalent to solving for $I/I_s = 1$, gives

$$\frac{\Omega^2}{\gamma^2} = \frac{1}{2}. \tag{4.36}$$

where I is the intensity. As I is proportional to E^2, and Ω is proportional to E, then I must be proportional to Ω^2. Combining this with Equation 4.36 gives the expression for the Rabi frequency in terms of the intensity.

$$\Omega^2 I_s = \frac{I\gamma^2}{2} \tag{4.37}$$

The saturation intensity will be different for different transitions, due to the different Clebsch-Gordan coefficients. However, the right hand side of Equation 4.37 is clearly independent of the transitions chosen and so the left hand side, which is proportional to $d_n^2 I_{s,n}$ is also independent of the transition. If the saturation intensity is known for any transition and the relative Clebsch-Gordan coefficients are known, we can therefore calculate the Rabi frequency for any transition. This is

$$\Omega^2 = \frac{I C_{g,n}^2 \gamma^2}{2 I_{s,0}} \tag{4.38}$$

where $I_{s,0}$ is the saturation intensity of the reference transition, and $C_{g,n}$ is the Clebsch-Gordan coefficient, normalized to the reference transition $n = 0$. The Clebsch-Gordan coefficient of a transition is therefore proportional to the dipole moment of that transition for any given atom. In potassium 39, the cycling transition of $|F = 2, m_f = 2\rangle \rightarrow |F' = 3, m_F = 3'\rangle$ has a saturation intensity of 1.75 mW/cm^2 [57], and is used as a reference. In order to calculate the effective Clebsch-Gordan coefficient for each hyperfine transition manifold, we must consider that the MOT light is isotropic. i.e. The MOT light contains equal intensities of π,σ^+ and σ^- polarisations from any quantisation axis. The effective Clebsch-Gordan coefficient for each transition manifold is then the RMS of the Clebsch-Gordan coefficient of each transition within that manifold. The effective squared Clebsch-Gordan coefficients for each transition for the D2 line are shown in Table 4.1.

This averaged transition strength is independent of the Zeeman state populations for isotropic light [58]. However, for a polarised beam, the effective transition strength is strongly dependent on the populations. In the context of a gain spectra in a MOT, this means the Rabi frequencies of the pump-atom interaction are independent of the Zeeman populations, but the absorption of each feature in the spectrum is dependent on the populations. Despite

Transition Manifold	Effective Isotropic Polarised Transition Strength $\overline{C_G^2}$
$\|F=1\rangle \rightarrow \|F'=0\rangle$	$\frac{1}{9}$
$\|F=1\rangle \rightarrow \|F'=1\rangle$	$\frac{5}{18}$
$\|F=1\rangle \rightarrow \|F'=2\rangle$	$\frac{5}{18}$
$\|F=2\rangle \rightarrow \|F'=1\rangle$	$\frac{1}{30}$
$\|F=2\rangle \rightarrow \|F'=2\rangle$	$\frac{1}{6}$
$\|F=2\rangle \rightarrow \|F'=3\rangle$	$\frac{7}{15}$

Table 4.1: Averaged Clebsch-Gordan coefficients for isotropic pumping

the isotropy of a MOT, the Zeeman state populations are not generally equally populated, meaning there is some uncertainty in the expected absorption strength of each feature.

Combining Equations 4.34 and 4.38 we get the Rabi frequency of the Raman transition formed by a given excited state as,

$$\Omega_{R,F'}{}^2 = \left(C_{G,g1,F'}C_{G,g2,F'}\right)^2 \frac{I\gamma^4}{16\Delta^2 I_{s,0}{}^2} I_p \tag{4.39}$$

The effective strength of the Raman transition associated with a given excited state is therefore proportional to the square of the product of the Clebsch-Gordan coefficients for the two ground states. For potassium-39, these are shown in Table 4.2

		$\left(C_{G,g1,F'}C_{G,g2,F'}\right)^2$
F'	0	0
	1	$\frac{1}{108}$
	2	$\frac{5}{108}$
	3	0

Table 4.2: Effective strengths of Rabi transitions from each of the excited states

The $|F'=2\rangle$ therefore dominates any Raman transitions in potassium-39. This simplifies the system, as considering only the $|F'=2\rangle$ state is a good approximation, and so any Raman

gain can be treated as arising from a single hyperfine Raman transition.

4.4 Measuring the Gain Experimentally

In order to measure the gain in the cold atoms, a MOT was made using the default detunings and intensities, defined in Chapter 2. A weak probe, nearly parallel to one of the MOT beams, was passed through the MOT and onto an APD (Thorlabs APD110A/M). The probe beam passed through a small hole before hitting the APD which blocked any stray MOT light. The internal piezo of the probe laser was then scanned in order to scan the probe frequency over the spectrum. The internal piezo was used to change the frequency instead of the AOM. This is because the AOM has a bandwidth of 50 MHz, which is comparable to the excited state hyperfine splitting and much smaller than the ground state hyperfine splitting. The measured MOT spectrum is the atomic transmission multiplied by the AOM efficiency curve, which means that transmission measurements will be strongly distorted by scanning using the AOM. In addition, the large scan range available using the piezo enabled a continuous scan across the $|F = 2\rangle \rightarrow |F'\rangle$ and the $|F = 1\rangle \rightarrow |F'\rangle$ transitions, which allowed the approximate ground state populations to be determined from the relative absorption of the two features.

The cost of scanning the laser with the piezo is the inability to precisely control the scan range and the inability to lock the laser to a precise frequency reference. The first problem was overcome by adding sidebands to the probe light and shining it through the cavity. The cavity transmission spectrum then contains sidebands, which give a frequency reference to the probe spectra as the frequency difference between the sidebands and the carrier peak is well known. The second problem was not considered major enough to address, and the observed Stark-shifted $|F = 2\rangle \rightarrow |F' = 3\rangle$ was used as the frequency reference. The uncertainty in this reference is dominated in the uncertainty of the Stark shift which is 1.2 ± 0.4 MHz for the default MOT parameters. This error is dominated by the uncertainty of the cooling-repump ratio, as measurements presented here were taken before the confocal cavity was

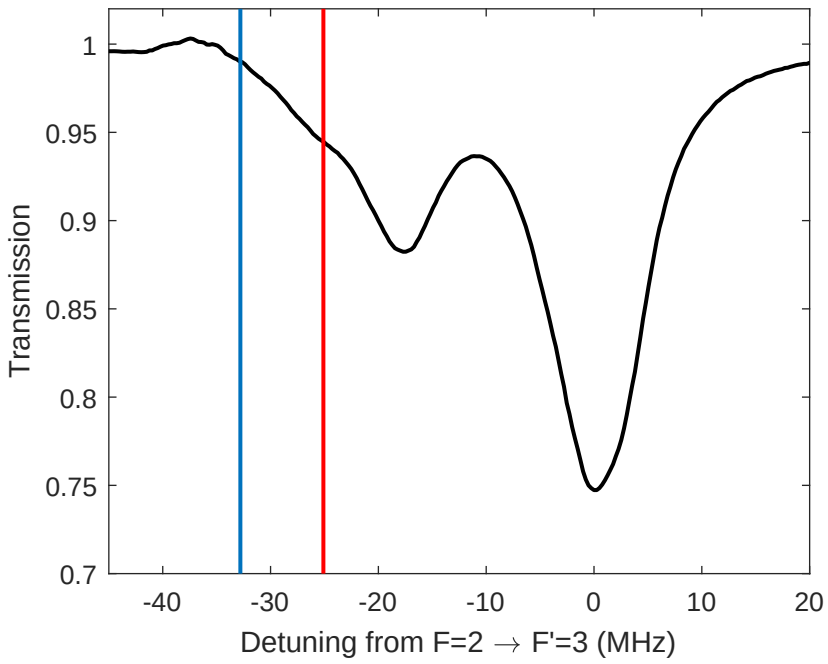

Figure 4.3: Measured weak-probe transmission spectrum through the MOT. The x-axis is referenced to the Stark shifted $|F = 2\rangle \rightarrow |F' = 3\rangle$ transition. The red line gives the approximate cooling frequency, and the blue line gives the expected two-photon transition frequency, without considering the effects of Stark shifts.

built. However, the uncertainty of the frequency reference is good enough for the purposes of understanding the gain mechanism, so the measurements need not be retaken with a precise knowledge of the cooling-repump ratio.

A small gain peak is clearly visible red of the $|F = 2\rangle \rightarrow |F' = 2\rangle$. It has similar linewidth to the absorption features, and has a frequency such that the pump beam is approximately halfway between the gain peak and the $|F = 2\rangle \rightarrow |F' = 2\rangle$ absorption feature. The pump frequency was worked out by adding the expected Stark shift from the pump light. This was calculated using the first non-zero term of Equation 4.22, which represents the Stark shift from far detuned light. For the default MOT parameters, this gives a Stark shift of 1.2 MHz for the $|F = 2\rangle \rightarrow |F' = 3\rangle$ transition, which means the MOT beam appears approximately

halfway between the $|F = 2\rangle \rightarrow |F' = 2\rangle$ transition, and the gain feature. The repump Raman transition is 7.7 MHz red-detuned of the pump beam, which is slightly blue-detuned from the gain feature. However, the Stark shifts of the ground states must be taken into account when calculating the expected Raman transition frequency. For a weak probe beam, the Stark shift from the two-photon transition is given by the sum of the Stark shifts from each excited state [59]. Using Equation 4.22, the total Stark shift from the repump beam is ≈ 3.3 MHz for the $|F = 1\rangle$ state. The Stark shift for the $|F = 2\rangle$ from the influence of the cooling beam is calculated to be ≈ 1.2 MHz, giving a total shift Stark shift of the Raman transition of ≈ 2.1 MHz. This suggests that the gain feature is at a similar frequency to the Raman transition frequency. However, the feature is comparable to the natural linewidth of the excited states.In the Raman gain mechanism, the transition is between two ground states, so the feature may be much narrower. One possible reason for the large linewidth is that the MOT beams are rapidly pumping atoms out of both ground states, which decreases their lifetime to the point that it is comparable to the lifetime of the excited state. Another possible reason for the broadening is that there is some decoherence between the two ground states, which could be caused, for example, by stray magnetic fields.

The spectrum also shows characteristics of Mollow gain. The first is that the linewidth of the gain spectrum is similar to the natural linewidth, as mentioned above, which is an expected feature of Mollow gain. The cooling light is also approximately halfway between the gain feature and the absorption feature, which would be expected for Mollow gain. The Rabi frequency for the $|F = 2\rangle \rightarrow |F' = 2\rangle$ transition is calculated to be 5 ± 2 MHz, where the dominant source of error is due to the uncertainty in the cooling-repump ratio. If the gain feature was due to Mollow gain, then it would be expected that the splitting between the absorption feature and the gain feature would be approximately $2\sqrt{\Omega^2 + \Delta^2}$, which for the default power and detuning is 16 ± 2MHz. The measured splitting in the above feature is 19 ± 1 MHz which is comparable to the expected frequency of Mollow gain. However, the expected positions of each of the features are based on the two-level calculation with a single

dressing beam, which is not a good approximation for the MOT with the default parameters. This means a single spectrum is not enough to conclusively distinguish whether Mollow gain or Raman gain is the relevant mechanism. In order to distinguish between Mollow and Raman gain, both gain mechanisms will be calculated numerically, and compared to the experimental results.

4.5 Numerical Calculation of Gain spectra

In order to numerically model the gain spectrum, the model is changed slightly to be an atom interacting with a classical field, rather than a quantum field. This is done in order to limit the size of the Hilbert space, allowing for faster calculation and less memory usage. Experimentally, the pump beams have a large mode volume such that the vacuum Rabi frequency is very small, and the beams are high powered, such that the photon number is much larger than one. The difference between the two models is therefore negligible for the experimental conditions considered here. The Hamiltonian of a two-level atom interacting with a classical field in this model is

$$H = \hbar\omega_0\sigma^\dagger\sigma - \frac{\hbar\Omega}{2}\cos(\omega t)(\sigma^\dagger + \sigma) \tag{4.40}$$

where all the parameters are as above, $\Omega = \frac{2d.E_0}{\hbar}$ is the Rabi frequency of the interaction and E_0 is the amplitude of the electric field. To remove the explicit time dependence of this Hamiltonian, we transform into the interaction picture. We make the transformation

$$H \to U^\dagger H U - H_0 \tag{4.41}$$

where $U = e^{\frac{-iH_0t}{\hbar}}$ and $H_0 = \hbar\omega\sigma^\dagger\sigma$. By Taylor expanding U, and using that $|e\rangle$ and $|g\rangle$ represent a complete basis, we can write $U = |g\rangle\langle g| + e^{-i\omega t}|e\rangle\langle e|$. This commutes with the

first term of the Hamiltonian, and the second term, representing the interaction, becomes

$$H_I = \frac{\hbar\Omega}{2}(\sigma^\dagger(1+e^{2i\omega t}) + \sigma(1+e^{-2i\omega t})) \tag{4.42}$$

We then make the rotating wave approximation to ignore the terms oscillating at twice the optical frequency. The full, semi-classical Hamiltonian becomes

$$H = \hbar\Delta\sigma^\dagger\sigma + \frac{\hbar\Omega}{2}(\sigma^\dagger + \sigma) \tag{4.43}$$

Note the similarity of this Hamiltonian to the full quantum Hamiltonian in Equation 4.13

The time evolution of the density matrix, ρ, for an open quantum system is given by the Lindblad master equation,

$$\dot{\rho} = -\frac{i}{\hbar}[H,\rho] + \sum_n \frac{\gamma_n}{2}(2a_n\rho a_n^\dagger - a_n^\dagger a_n\rho - \rho a_n^\dagger a_n) \tag{4.44}$$

where, γ_n is the energy decay rate and a_n is the collapse operator for a particular decay channel. For a two-level atom interacting with a classical field, there is only one decay channel: spontaneous emission of the atom. Therefore γ_n is just γ, the linewidth of the transition, and a_n is σ. The equilibrium state of the system can be found by setting the right hand side of Equation 4.44 to zero and solving for ρ numerically.

However, a two-level atom model would not be expected to accurately model the experimental conditions that are used in this thesis for two reasons. Firstly, the splitting of the hyperfine levels in potassium is comparable to the detuning of the pump beam, the Rabi frequency of the pump beam, and the linewidth of the transition. This means that other levels would be expected to contribute strongly to the transmission spectrum of the atoms, making a two-level calculation inappropriate. The degenerate Zeeman levels have also been shown to contribute to the absorption spectrum for Mollow gain [60]. The second reason a two-level model is inappropriate is that Raman gain is intrinsically a three-level process, requiring two ground states. A further complication in a potassium-39 MOT is that the re-

pump and cooling beams are of comparable intensities, which mean both are strong enough to dress the atoms and contribute to the gain spectrum. Because of these difficulties, slightly different models were used to simulate Mollow and Raman gain spectrum.

4.6 Numerical Modelling of Raman Gain

In order to model Raman gain, a full six-level calculation was performed. This is required as although the $|F' = 2\rangle$ state dominates the gain mechanism, the other transitions are close enough to have significant effects on the probe spectrum. In particular the $|F = 2\rangle \rightarrow |F' = 3\rangle$ is the largest absorption feature, the $|F' = 2\rangle \rightarrow |F = 1\rangle$ is relatively close to the gain feature, and the $|F = 1\rangle \rightarrow |F' = 0, 1\rangle$, are close to resonance with the repump beam, so significant dressing of these states may occur. One simplification that was made in this model was to replace the cooling beam by an incoherent pumping term from the $|F = 2\rangle$ state to the $|F = 1\rangle$ term, which has the effect of replenishing the $F = 1$ state. This is the expected role of the cooling light in Raman gain mechanism, so if Raman gain is the correct model, the only difference to the gain will be the absence of the Stark shifts due to cooling light in the numerical model. This simplification was made in order to model a pure Raman process, without extra terms from the interaction between the cooling and repump light or any Mollow process from the cooling beam. A similar approximation was made in [19]. The Hamiltonian of the full six-level system is given by

$$\begin{aligned} H = {} & \hbar\omega_{gss} \left|F = 2\right\rangle \left\langle F = 2\right| + \sum_{F'} \hbar\omega_{1,F'} \left|F'\right\rangle \left\langle F'\right| \\ & - \cos(\omega_r t) \sum_{1,F'} \frac{\Omega_{1,F'}}{2} (\left|F = 1\right\rangle \left\langle F'\right| + \left|F'\right\rangle \left\langle F = 1\right|) \\ & - \cos(\omega_p t) \sum_{2,F'} \frac{\Omega_{2,F'}}{2} (\left|F = 2\right\rangle \left\langle F'\right| + \left|F'\right\rangle \left\langle F = 2\right|) \end{aligned} \tag{4.45}$$

where ω_{gss} is the ground state splitting, and $\omega_{1,F'}$ is the resonance frequency $|F = 1\rangle \rightarrow |F'\rangle$ transition, and ω_p and ω_r are the probe and repump frequencies. This Hamiltonian assumes

that the probe and repump beams only interact with one ground state. This assumption is justified as the repump beam is approximately ω_{gss} from resonance with the $|F=2\rangle \rightarrow |F'\rangle$ transitions, which is large compared to any other detunings. The effect of this simplification is to eliminate the Stark shift from the repump on the $|F=2\rangle \rightarrow |F'\rangle$ transitions. The size of this effect is calculated to be well under 1 MHz using the default MOT parameters, so the approximation is reasonable.

Equation 4.45 is then transformed according to Equation 4.41, where now $H_0 = \hbar\omega_r \sum_{F'} |F'\rangle \langle F'| + \hbar(\omega_r - \omega_p) |F=2\rangle \langle F=2|$. This form of H_0 is chosen as it eliminates the time dependence of the Hamiltonian in the rotating wave approximation. The transformed Hamiltonian after making the rotating wave approximation is

$$\begin{aligned} H = {} & \hbar\Delta |F=2\rangle \langle F=2| - \sum_{F'} \hbar\delta_{F'} |F'\rangle \langle F'| \\ & - \sum_{1,F'} \frac{\Omega_{1,F'}}{2} (|F=1\rangle \langle F'| + |F'\rangle \langle F=1|) \\ & - \sum_{2,F'} \frac{\Omega_{2,F'}}{2} (|F=2\rangle \langle F'| + |F'\rangle \langle F=2|), \end{aligned} \tag{4.46}$$

where Δ is the two-photon detuning, given by $\Delta = \omega_p + \omega_{gss} - \omega_r$ and $\delta_{F'}$ is the repump detuning, given by $\omega_r - \omega_e$.

The collapse operators used are also slightly more complicated for the six-level atom due to the presence of two ground states. The $|F'=1,2\rangle$ can both decay into either of the ground states, with a probability given by the branching ratio $b_{FF'}$. The decay rate associated with each decay channel is therefore multiplied by the branching ratio to give, $\gamma_{F,F'} = b_{FF'}\gamma$. The branching ratios for the potassium-39 D2 line are shown in Table 4.3.

The spontaneous emission collapse operators are therefore $a_n = |F\rangle \langle F'|$, with an associated rate $\gamma_n = \gamma_{F,F'}$. Two other collapse operators are introduced. The first introduces dephasing between the ground states and is given by $|F=1\rangle \langle F=1| - |F=2\rangle \langle F=2|$, with an associated rate γ_d. The second replaces the cooling beam and pumps population from

		F'			
		0	1	2	3
F	1	1	$\frac{5}{6}$	$\frac{1}{2}$	0
	2	0	$\frac{1}{6}$	$\frac{1}{2}$	1

Table 4.3: Branching ratios for the D2 line of potassium-39

the $|F = 2\rangle$ state to the $|F = 1\rangle$ state. This is given by $|F = 1\rangle \langle F = 2|$ and has a rate γ_p. The master equation given by Equation 4.44 can then be solved numerically for steady state ($\dot{\rho} = 0$) to give the steady state density matrix, ρ.

In order to turn the density matrix into a transmission spectrum, the gain should be understood as a consequence of the electric susceptibility of the atoms. This can be shown by starting with the wave equation for an electric field E, derived from Maxwell's equations,

$$\frac{\partial^2 E}{\partial t^2} = \frac{1}{\sqrt{\epsilon\mu}} \boldsymbol{\nabla}^2 E. \tag{4.47}$$

where ϵ and μ are the electric permittivity and magnetic permeability respectively. Assuming the magnetic susceptibility is zero, and using that $\epsilon = (1 + \chi)\epsilon_0$, Equation 4.47 becomes

$$\frac{\partial^2 E}{\partial t^2} = \frac{\sqrt{1+\chi}}{c} \boldsymbol{\nabla}^2 E \tag{4.48}$$

where χ is the electric susceptibility. Considering that in a wave equation, the real part of the coefficient of the laplacian term gives the phase velocity of the wave v_p, we define $n_p = \mathrm{Re}[\sqrt{1+\chi}] \approx 1 + \frac{\mathrm{Re}[\chi]}{2}$, such that $v_p = \frac{c}{n_p}$. Assuming the electric field is in the form of a slowly varying envelope, multiplied by a phase factor, the solution to Equation 4.48 can be written

$$E = E_0 e^{i(k(1+\frac{\chi}{2})x - \omega t)}. \tag{4.49}$$

Splitting χ into real and imaginary parts, such that $\chi \equiv \chi' + i\chi''$ where χ' and χ'' are real

gives

$$E = E_0 e^{i(kx-\omega t)} e^{-\frac{\chi'' kx}{2}} e^{\frac{i\chi' kx}{2}}. \tag{4.50}$$

So the real part of χ (and n_p) describes a phase shift, which is equivalent to a change in phase velocity, and the imaginary part describes attenuation and gain. Therefore if the susceptibility of the atoms can be calculated from the density matrix, the absorption and gain immediately follows. The expectation value of the polarisation of an atom is given by $P = e\langle\psi|\, x\,|\psi\rangle$, where ψ is the wave function of the outer electron and x is the position operator, which has odd parity. Eigenstates of the atomic potential have a well defined parity, meaning $\psi^\dagger(x)x\psi(x)$has an odd parity if ψ is an eigenstate. As the expectation value is calculated by integrating this over all space, this means the expectation value of the electric dipole of an eigenstate of the bare atom is 0. In Dirac notation this means if $|\psi\rangle = C_g\,|g\rangle + C_e\,|e\rangle$, where $|g\rangle$ and $|e\rangle$ are eigenstates of the Hamiltonian, then $P = e(C_g C_e\,\langle g|\, x\,|e\rangle + C_g C_e\,\langle e|\, x\,|g\rangle)$. In the density matrix formalism, this is equivalent to $P = 2d_{ge}\rho_{ge}$ where $d_{ge} = \langle g|\, ex\,|e\rangle$. It has been shown in section 4.3 that the Clebsch-Gordan coefficient is proportional to the dipole moment of a transition. Therefore $P \propto C_{G,g,e}\rho_{ge}$. For a multilevel atom, all of the above arguments hold meaning the polarisation of an atom with multiple hyperfine excited states is

$$P \propto \sum_{F'} C_{G,F,F'}\rho_{FF'} \tag{4.51}$$

where F and F' now label the ground and hyperfine excited states respectively. For a given probe field, the polarisation is proportional to the susceptibility, the imaginary part of which gives the absorption coefficient. For an optically thin MOT, the transmission is therefore given by

$$T = 1 - A\sum_{F,F'} C_{G,F,F'}\,\mathrm{Im}\{\rho_n\} \tag{4.52}$$

where A is an overall scaling factor to account for the column density of the atoms seen by the probe beam and all the constants of proportionality lost in the derivation. An ex-

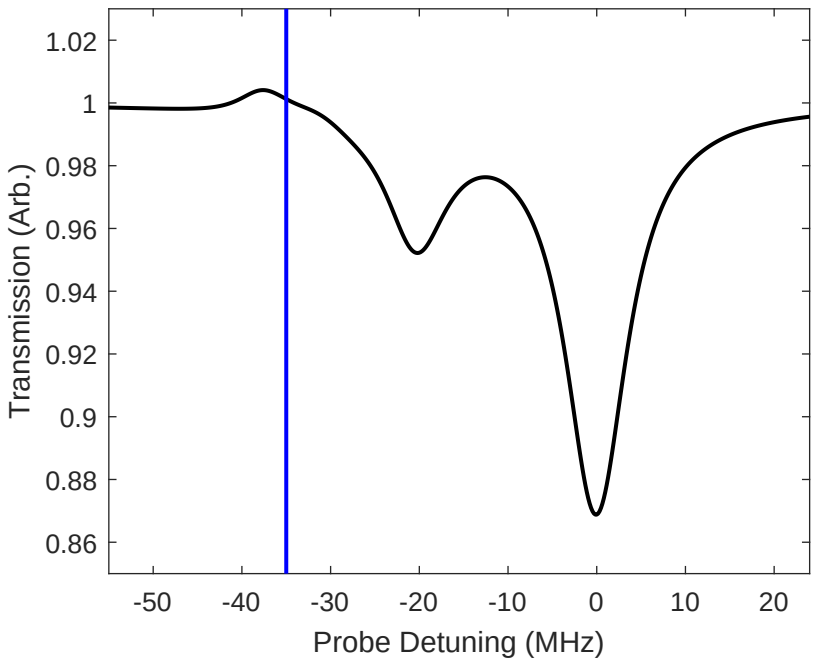

Figure 4.4: Numerically calculated transmission spectrum, using the Raman model. The parameters used for this simulation are default repump frequency and power, with dephasing rates $\gamma_d = 1.5$ MHz and $\gamma_p = 1$MHz. The blue line gives the two-photon detuning, without incorporating the Stark shifts.

ample transmission spectrum, which shows the transmission close to the $|F = 2\rangle \rightarrow |F'\rangle$ is shown in Figure 4.4. This example spectrum uses the normal repump power and detuning and the phenomenological parameters, γ_d and γ_p, were chosen to approximately match the measured probe spectra in terms of populations, relative height of the gain feature, and the linewidths of the absorption features. The dephasing rate, γ_d, is comparable to the broadening expected from the MOT [29], and the pump rate γ_p is similar to the pump rate expected from the cooling beam, given its intensity and detuning. The overall transmission amplitude is arbitrary, and so has been scaled to approximately match the experimental transmission measurement in Figure 4.3. The numerical model for Raman gain therefore suggests that is at least plausible as an explanation for the observed gain.

4.7 Numerical Modelling of Mollow Gain

The Mollow gain spectrum was also calculated numerically in order to see if it is a plausible mechanism for the observed gain. As the Mollow gain only uses one ground state, the Mollow gain spectrum was calculated for a three-level atom, containing the $F = 2$ ground state, and the $F' = 1, 2$ excited states of potassium-39. These are the states that are approximately resonant with the cooling beam of the MOT and have a non-zero Clebsch-Gordan coefficient. It was decided to not include Zeeman sublevels in the model, as this would increase the number of states to 20, which requires more computing power than was available. The three-level Hamiltonian is given by

$$H_{3LA} = \sum_{F'=1,2} \hbar\Delta_{F'} \left|F'\right\rangle \left\langle F'\right| + \hbar\Omega_n(\sigma_n^\dagger + \sigma_n) \tag{4.53}$$

where $\Delta_{F'} = -30.5, -21.1$ for a pump resonant with the $|F' = 3\rangle$ state, and Ω'_F is in the effective Rabi frequency for each transition, discussed in the next section. $\sigma_{F'}$ is shorthand for $|F = 2\rangle \langle F'|$. The collapse operators in the Master equation are the set of $\sigma_{F'}$ with a rate of $\gamma_{F'} = 6.032$ MHz for each F'. As the pump has a similar frequency to the probe, the probe cannot be included in the Hamiltonian as in the Raman model. The transmission spectrum was therefore calculated using the QuTiP function `spectrum_ss()`, which calculated the steady state transmission spectrum by finding the correlation of the atomic raising and lowering operators at different times [61]. This approach had the downside of being very memory intensive, which prevented the $|F' = 3\rangle$ being included, due to memory constraints.

In order to factor in the different Clebsch-Gordan coefficients, two approaches were taken which had a different order of calculating the correlation and the sum. The first approach calculated the correlation of the sum of atomic operators, where each operator was weighted by the Clebsch-Gordon coefficient of the relevant transition. The second approach calculated the sum of the correlation between similar atomic operators, weighted by the square of the relevant Clebsch-Gordon coefficients. These methods gave similar results, and identical

results for low pump powers, so only the result with the correlations calculated first is shown here. A selection of numerically calculated probe spectra for various pump intensities is shown in Figure 4.5.

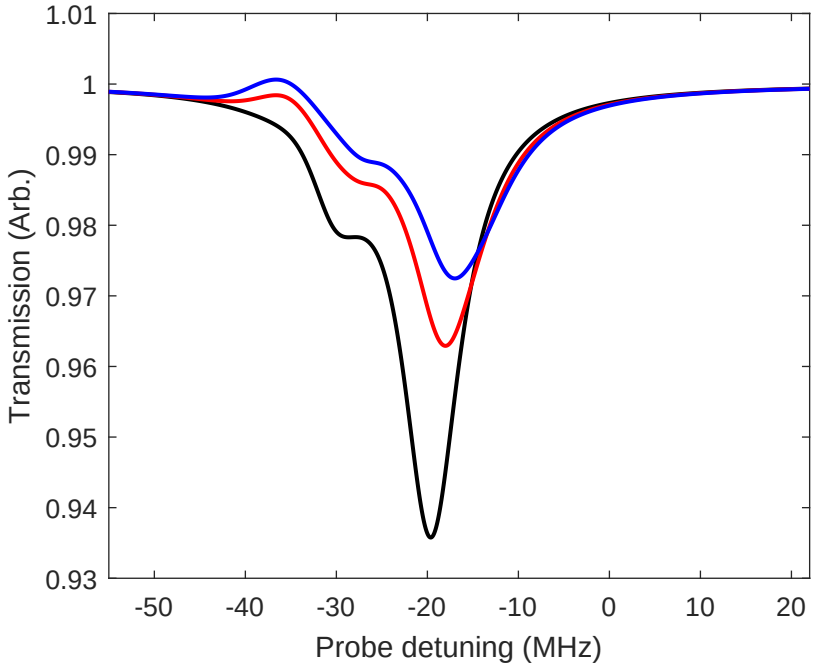

Figure 4.5: Numerically calculated Mollow spectra for various pump powers. The black curve corresponds to a pump intensity of 15 mW/cm^2, which is similar to the experimental conditions. The red and blue curves correspond to a pump intensities of approximately 30 mW/cm^2 and 60 mW/cm^2 respectively. The higher intensity curves resemble the experimental probe spectrum, but are impractical in the experiment. Note the absorption feature from the $|F' = 3\rangle$ feature is absent, because the $|F' = 3\rangle$ level is not included in this model.

The numerical results imply that Raman gain is the more likely model for the observed gain, as although it is possible to produce numerical Mollow spectra that resemble the experimental results in terms of gain linewidth and amplitude, the pump intensity required to do so is approximately 60 mW/cm^2. This is roughly a factor of 4 higher than the practical pump power in the experiment, so the numerical results imply that Mollow gain is an unlikely mechanism for producing the observed features.

4.8 Varying MOT parameters

In order to further investigate the gain mechanism, the MOT parameters were changed. This will allow the MOT parameters to be tuned to maximise or minimise the gain or the gain/atom ratio, which would be useful for preventing lasing while coupling the atoms strongly to the cavity or to allow brighter lasing than observed in Chapter 3. Changing the MOT parameters was expected to modify the MOT in several ways: It changes the total atom number in the MOT, the relative populations in the atomic ground states, and also the gain for each atom in the relevant state. These parameters can all be roughly measured by taking two transmission spectra. The first spectrum should range over the transitions from both ground states. This allows comparisons between the $|F = 1\rangle \rightarrow |F'\rangle$ and $|F = 2\rangle \rightarrow |F'\rangle$ transitions. An example of a probe spectrum like this is shown in Figure 4.6. For each set of parameters, 32 spectra were averaged in order to reduce the effects of fluctuations in the atom number.

The second scan was over only the $|F = 2\rangle \rightarrow |F'\rangle$ manifold, which allows for a more precise measurement of the gain amplitude and frequency. An example of this type of spectrum can be seen in Figure 4.3. To measure the ground state populations, the optical depth of each transition can be calculated from the wide transmission spectra. The optical depth is given by

$$OD_n = -\log(I_n/I_0) \tag{4.54}$$

where I_n is the minimum transmitted intensity for light resonant with transition n, and I_0 is the intensity of non-resonant light. The optical depth of each transition is then weighted by the relevant $1/{C_G}^2$ and the ratio of the two weighted optical depths gives the relative population of the ground states. The sum of the optical depths is proportional to the total atom number. The gain per atom in the relevant state depends on the gain model. For Raman gain the gain peak should be normalised to the absorption of the $|F = 1\rangle \rightarrow |F'\rangle$ transition, as this gain mechanism acts on atoms in the $F = 1$ state. Mollow gain acts on

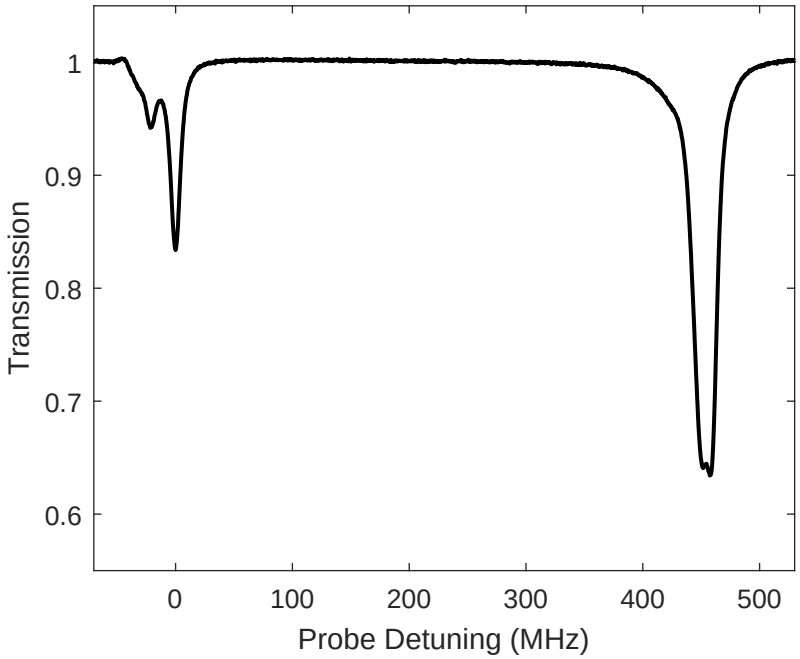

Figure 4.6: Example wide scan spectrum using the default parameters. The left hand transition is the $|F = 2\rangle \rightarrow |F'\rangle$ and the right hand transition is the $|F = 1\rangle \rightarrow |F'\rangle$. The x-axis is referenced to the $|F = 2\rangle \rightarrow |F' = 3\rangle$ transition.

atoms in the $F = 2$ state, and so the gain peak should be normalised to the $|F = 2\rangle \rightarrow |F'\rangle$ if Mollow gain is the dominant mechanism.

Note that changing the Zeeman state populations changes the averaged Clebsch-Gordan coefficient for a given probe polarisation. This means that the populations cannot be calculated precisely in this method, without knowing the exact Zeeman state populations. For the $|F = 2\rangle \rightarrow |F'\rangle$ this problem could be mitigated by measuring the optical depth of the $|F = 2\rangle \rightarrow |F' = 3\rangle$ which has a variation in the Clebsch-Gordan, defined as $({C_{G,max}}^2/{C_{G,min}}^2)$, for linearly polarised light of 1.8. This is the maximum variation, which represents the difference between all of the population being in the most strongly coupled state and all of the population being in the least coupled state. The actual variation is likely to be much smaller than this, as it is unlikely that changing the MOT parameters changes the populations in

such a drastic way. For the $|F = 1\rangle \rightarrow |F'\rangle$, the $|F' = 2\rangle$ and $|F' = 1\rangle$, which dominate the transitions are separated by 1.6γ, meaning the transitions are in an intermediate regime between being resolved and unresolved. This means it is not possible to isolate the individual transitions as for the $|F = 2\rangle \rightarrow |F'\rangle$ transition. Treating the $|F = 1\rangle \rightarrow |F'\rangle$ as a single transition gives a variation in Clebsch-Gordan variation of 1, implying the absorption is independent of the population. However, because the transitions are partially resolved a change in the Zeeman populations can be seen as a change in the relative heights of the two Zeeman peaks. This means that this method is unable to provide precise measurements of the atom number and populations without knowing the precise Zeeman populations. However, it can give reasonable measurements of large changes in the populations. Because of the large intrinsic error in these measurements and to simplify data processing, the total minimum of the $|F = 1\rangle \rightarrow |F'\rangle$ manifold was used to calculate the optical depth. The relative population in the $|F = 1\rangle$ state was then calculated using the sum of the ${C_G}^2$ for each transition multiplied by 2/3, which is a factor which incorporates the decrease in peak absorption caused by the separation of the transitions. The effective Clebsch-Gordan coefficients used were then $\frac{7}{15} = 0.47$ for the $|F = 2\rangle \rightarrow |F' = 3\rangle$ transition, and 0.45 for the $|F = 1\rangle \rightarrow |F'\rangle$ transition. The relative ground state populations of the MOT are therefore approximately just the relative absorption of the $|F = 1\rangle \rightarrow |F'\rangle$ and $|F = 2\rangle \rightarrow |F' = 3\rangle$ transitions.

4.8.1 Repump Frequency Vs Populations

The technically easiest change to the MOT parameters is to change the repump frequency because it can be altered by changing the frequency on the repump AOM, without changing any other parameters. This means the repump frequency can be modified quickly and precisely. The main downside to the method is that changing the AOM frequency changes the efficiency of the AOM and the alignment of the repump beam slightly. This limits the range the AOM can be varied over to approximately 5 MHz (10 MHz change in repump frequency, due to the double pass) before significant changes in the repump power occur.

This was not a problem in practice because the gain and MOT number is very sensitive to the repump frequency, meaning that the frequency range of the repump was limited by the gain disappearing, rather than changes to the repump power.

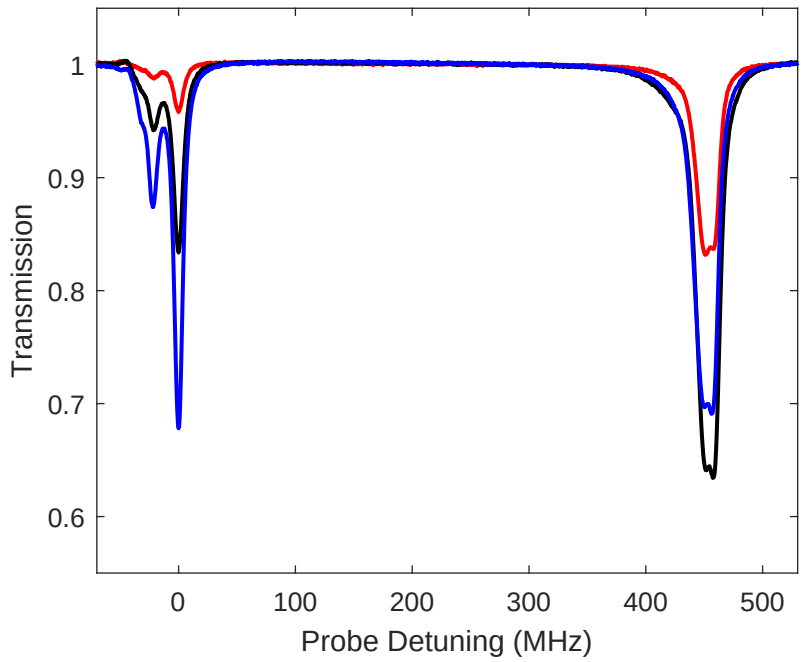

Figure 4.7: Wide probe spectra for various repump frequencies. The detunings of the repump beam from the $|F = 1\rangle \rightarrow |F' = 3\rangle$ transition are -36.7 MHz,-34.7 MHz, and -30.7 MHz for the red, black, and blue curves respectively. The left and transition is the $|F = 1\rangle \rightarrow |F'\rangle$ and the right hand transition is the $|F = 2\rangle \rightarrow |F'\rangle$. The x-axis is referenced to the $|F = 2\rangle \rightarrow |F' = 3\rangle$ transition.

A selection of transmission spectra for various repump frequencies is shown in Figure 4.7 and the ground state populations calculated is shown in Figure 4.8. The three repump frequencies shown span the range of repump frequencies for which gain is visible . When the repump is most red-detuned (red line), most of the population is in the $|F = 1\rangle$ due to inefficient pumping into the $|F = 2\rangle$ state. This leads to low total atom number because the cooling beam addresses relatively few atoms. For higher detunings, the repump beam becomes more efficient at pumping atoms into the $|F = 2\rangle$ state. This leads to a higher

total atom number, and stronger absorption on both transitions. For even higher detunings, where the repump is on resonance with the $|F = 1\rangle \rightarrow |F'\rangle$, the total atom number decreases slightly, as the cooling from the repump beam is reduced, but the absorption from the $|F = 1\rangle \rightarrow |F'\rangle$ transition is maximised, as a large proportion of the atoms are in the $|F = 2\rangle$ state. Note that the relative heights of the two peaks in the $|F = 1\rangle \rightarrow |F'\rangle$ manifold changes for different repump frequencies. This could be either due to changes in the Zeeman state populations, as discussed in Section 4.8, or to saturation of the excited states. The change is small compared to the total absorption, so can be ignored. Over the range of parameters

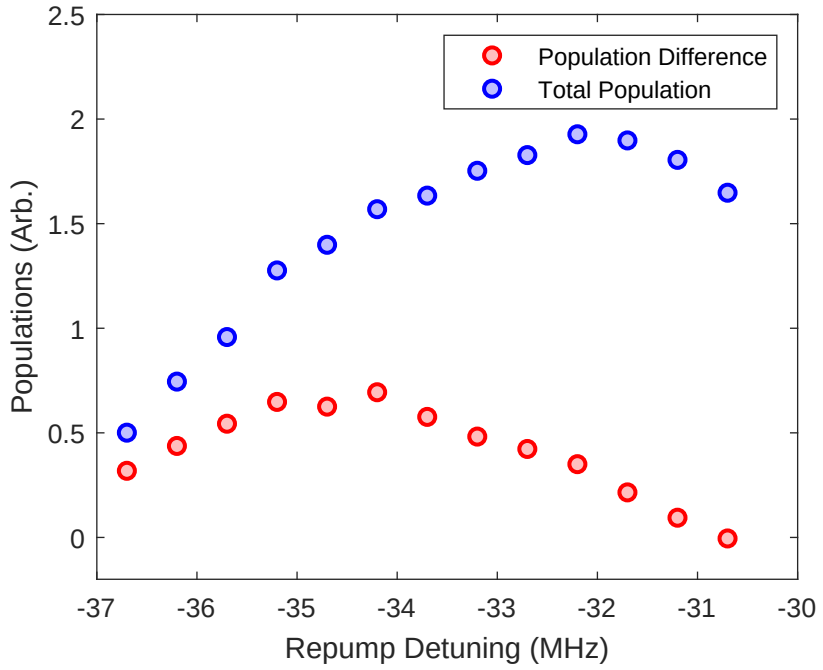

Figure 4.8: Populations in the $|F = 1\rangle$ and $|F = 2\rangle$ states. The red dots show the population difference in the ground states, and the blue dots show the total population, which is proportional to the atom number. The range of the cooling-repump detuning is the same as in Figure 4.7.

shown here, the populations are such that there are never more atoms in the $|F = 2\rangle$ state. At small repump detunings (approximately -31 MHz), the population difference is approximately

0. As the Raman gain amplitude is proportional to the population difference the net gain should be zero if Raman gain is the dominant gain mechanism. For large repump detunings (approximately -35 MHz), the total population difference is maximised, but the total MOT number is significantly reduced. This will give large gain, but relatively small absorption features for larger repump detunings.

However, if Mollow gain was the dominant gain mechanism, then because of the high proportion of atoms in the $|F = 2\rangle$ state, the gain would be maximised when the population difference is small. The blue line in Figure 4.7 shows no gain when the populations are approximately equal, which suggests that Raman gain is the relevant gain mechanism, but the low resolution on these measurements due to the large scan range means that the gain curve cannot be resolved clearly.

4.8.2 Repump Frequency vs Gain

A smaller scan was then taken over the $|F = 2\rangle \rightarrow |F'\rangle$ transition, which allowed the gain feature to be measured more precisely. Each trace produces a spectrum similar to Figure 4.3. These spectra are then combined into a contour plot, shown in Figure 4.9. The cooling detuning has been moved to -31 MHz for this measurement. This reduces the rate of optical pumping into the $|F = 1\rangle$ state, which allows for a wider range of repump detunings to be explored, but means that direct comparison with Figure 4.8 is not valid. However, the general trends of how the gain should appear from Section 4.8.1 will still be valid, with only the precise values changing. This measurement indicates that the gain moves as the repump frequency is changed, and the repump stays approximately on resonance with the two-photon Raman transition. The amplitude of the gain peak also disappears as the repump is moved closer to resonance, which also provides evidence that the gain is caused by the Raman mechanism, as Figure 4.8 shows that moving the repump onto resonance eliminates the population difference, which destroys the gain peak. The repump frequency was varied in the numerical model, described earlier, and a similar contour plot created. This is shown

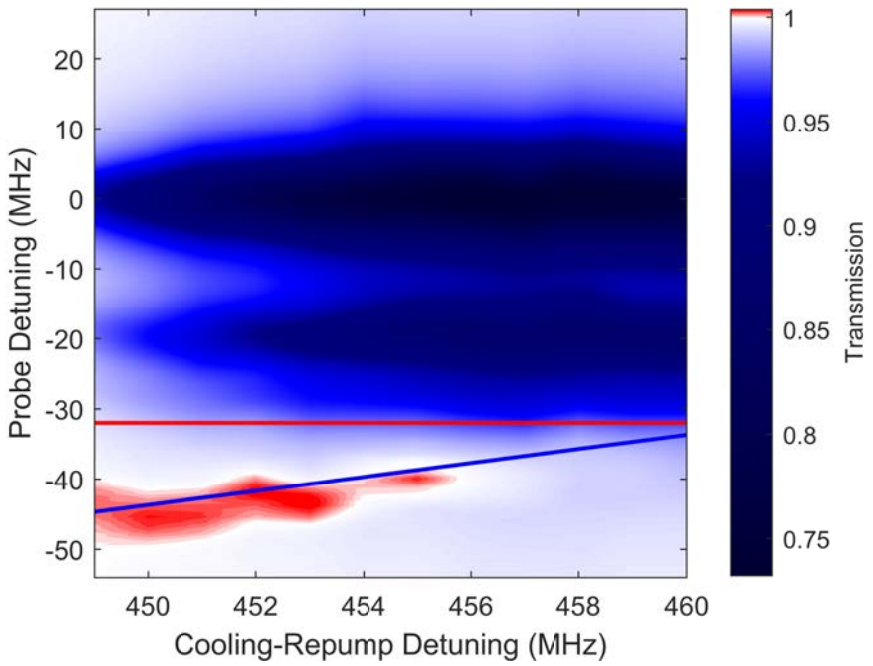

Figure 4.9: Contour plot showing transmission around the $|F = 2\rangle \rightarrow |F'\rangle$ transition as the repump frequency is changed. The two-photon transition associated with the repump frequency is shown by the blue line and the cooling frequency is shown by the red line. Gain is shown in red, and absorption as blue.

in Figure 4.10.

From the contour plots, the numerical model can be seen to match the experimental probe spectrum well. In particular, the amplitude and frequency of the gain peak vary similarly with repump frequency. The main difference between the plots is the decrease in absorption in the experimental figure for low repump frequencies. This can be explained by the total atom number in the MOT reducing when the repumping rate is too low. In the numerical model, there is no modelling of the total MOT number, so this feature isn't present. The difference between the gain feature frequency from the unshifted two photon frequency is also similar between the two figures, supporting the interpretation that this is caused by Stark shifts of the ground states, rather than an experimental error.

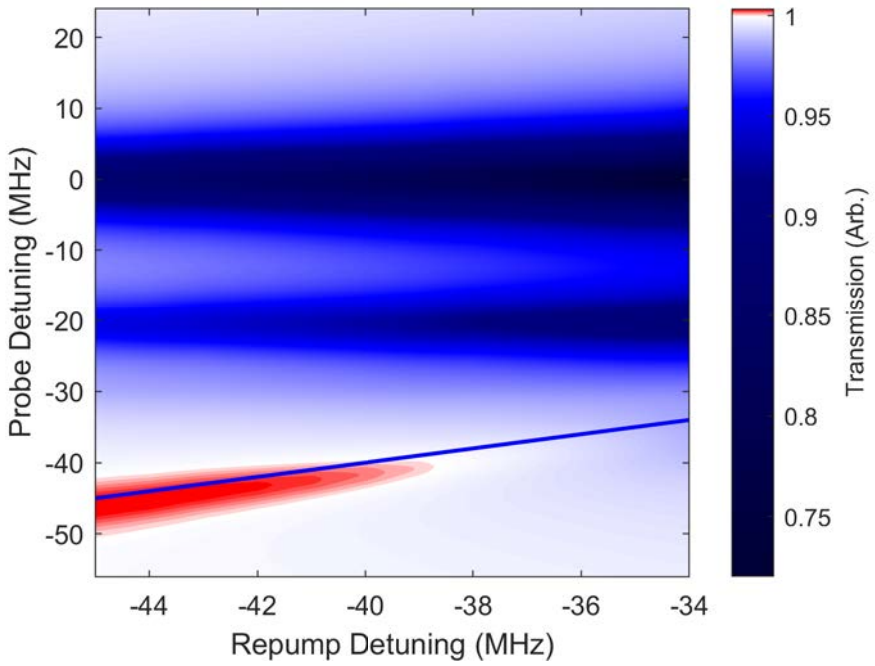

Figure 4.10: Contour plot of the numerical model of Raman Gain, similar to Figure 4.9. The line denoting the cooling frequency is absent, as the numerical model does not include well defined cooling frequency. The parameters used were $\gamma_d = 1.5$, $\gamma_p = 0.4$.

4.8.3 Cooling Frequency vs Gain

Changing the cooling frequency by itself is technically harder than changing the repump frequency. This is because the cooling frequency is changed by the changing the lock point of the MOT laser, from which the repump frequency is also derived. The repump AOM frequency must therefore be adjusted by half the change in the MOT beam frequency in order to keep the repump beam at the same frequency. Figure 4.11 shows that the frequency of the cooling beam does not affect the frequency of the gain feature, which strongly suggests that Mollow gain is not the relevant gain mechanism. This is especially convincing as the cooling beam crosses the $|F = 2\rangle \rightarrow |F' = 2\rangle$ transition. The Mollow gain theory predicts that this would destroy the gain as both dressed states would have equal ground state populations

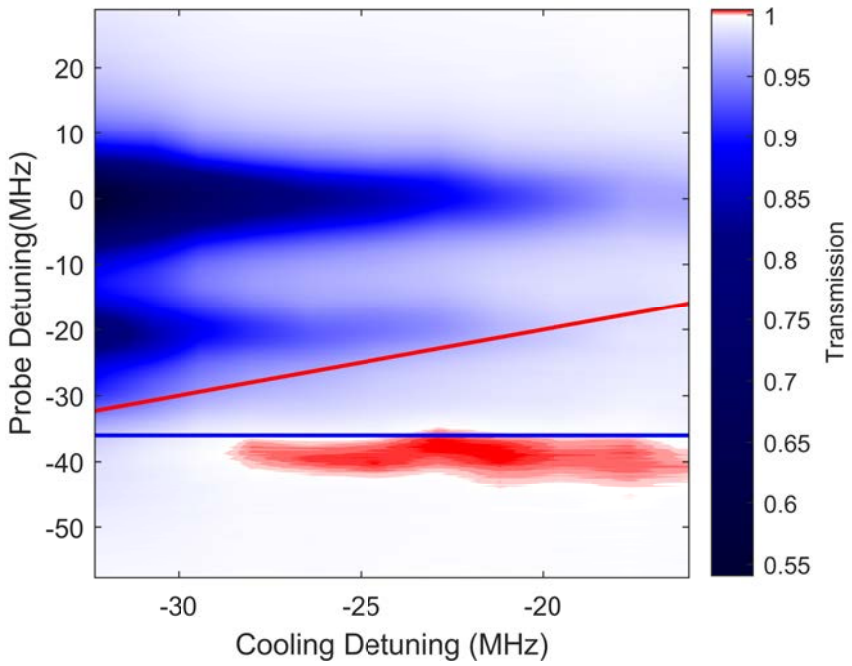

Figure 4.11: Contour plot of transmission spectrum as Cooling frequency is varied. The blue line gives the cooling frequency and the red line gives the two-photon transition frequency without Stark shifts.

according to Equation 4.17. This means that there would be no inversion. The absence of gain at large cooling detunings would be consistent with both Raman and Mollow gain, as the large pump detuning causes a depletion of the $|F = 1\rangle$ state, which destroys the population difference required for Raman gain. For Mollow gain, the large cooling detuning leads to a reduction in the dipole moment between the dressed states, according to Equation 4.25. The absorption features can be seen to be much weaker at small cooling detunings, which is due to a combination of optical pumping into the $|F = 2\rangle$ state, and a reduction in the total atom number due to inefficient cooling and trapping. The gain also decreases for small cooling detuning, due to the reduction in atom number, but is compensated by the increased relative population in the $|F = 1\rangle$ state. Large gain per atom can therefore be created by moving the pump beam on resonance, and the gain can be destroyed by moving the cooling

beam away from resonance.

4.9 Conclusion

A potassium-39 MOT has been shown to exhibit gain with no additional beams at a variety of MOT parameters. The gain mechanism has been demonstrated to be Raman gain between the $F = 1$ and $F = 2$ ground states. The gain frequency is tunable by changing the repump beam frequency within a narrow band, and the amplitude of the gain peak can be changed by altering the populations in the ground states by changing the cooling beam frequency. The gain is noticeably different from normal Raman gain in cold atoms in that the linewidth is comparable to the natural linewidth. This can be attributed to a combination of dephasing between the ground states, and the strong pumping of the ground states in a MOT, which causes an increase in the linewidth due to the ground states short lifetime. The gain mechanism demonstrated here is robust and technically simple, which makes it potentially useful for systems where power, weight or space is constrained. Two applications are demonstrated in this thesis: cold atom lasing is demonstrated in Chapter 3, and an investigation of the second order coherence of a coupled atom-cavity systems is performed in Chapter 5.

CHAPTER 5

SECOND ORDER COHERENCE TIME BELOW THRESHOLD

One of the results from Chapter 3 was that the second order coherence time of the system below threshold was measured to be approximately twice as long as the bare cavity lifetime. The MOT therefore extends the coherence time of the cavity. This has been predicted [62] and observed [63] in lasers operating below threshold as early as 1967. This can be viewed as the gain increasing the effective cavity lifetime, as the cavity lifetime and coherence times have been shown to be identical in the limit of large gain bandwidths. This has previously been observed in fibre based cavity ringdown spectroscopy measurements [64], where cavity ringdown measurements were used to measure gain. Adding gain to a cavity ringdown measurement has also been previously shown to compensate for losses in the fibre, and create a cavity with a higher effective finesse [65], which is useful for cavity ringdown. Previous work has focused on broadband gain media, where dispersive effects from the gain medium have been ignored. In the experiment presented here, the linewidth of the gain feature is comparable to the cavity linewidth, and so dispersive effects may play a role by modifying the group index of the system, which modifies the ringdown behaviour of the system [66, 67], and may also modify the second order coherence time.

To our knowledge, the increased second order coherence time for a coupled gain-cavity system has never been proposed as a mechanism to measure small gain. Using the second order coherence time to measure gain offers several advantages over using a cavity ringdown

approach. The first advantage is that no probe beam is required, which allows for technical simplicity, as well as allowing non-linear probes making it possible to probe gain which saturates at very low intensity. The lack of probe also allows for data to be collected in steady state, whereas a cavity ring down measurement requires rapid switching of the probe beam. The second order coherence time is therefore a potentially useful tool for measuring the gain.

This chapter discusses the theory and experimental results obtained, and demonstrates proof of principle for using the second order coherence of a cavity to measure gain.

5.1 Coherence and Ringdown times for Chaotic Light

Before considering the effects of gain, it is valuable to consider the expected timescales relating to chaotic light. Chaotic light can be described as light emitted by a large number of independent emitters, and includes thermal states [68]. This theory is therefore applicable to the light emitted by a cavity below threshold. The timescale with the most straightforward definition is the ringdown timescale. This is simply the lifetime of a photon. For a cavity, with a Fourier limited linewidth, this is given by $T_{rd} = 1/\kappa$, where κ is the angular FWHM linewidth of the cavity. Another timescale is the first order coherence time, which is the time over which the phase of a light field is unpredictable. If a light beam is split into two arms, one arm is delayed by a time τ, and recombined, the first order coherence time gives the timescale over which the two arms will interfere in a way that is distinct from two independent sources. For a lifetime broadened (spectrally Lorentzian) state, the first order coherence function is given by [68]

$$g^{(1)}(\tau) = e^{-\tau/T_{c,1}} \tag{5.1}$$

where $T_{c,1}$ is the first order coherence time. This is determined by the linewidth and is given by $T_{c,1} = 2/\kappa = 2T_{rd}$. For chaotic light, the second order coherence function, which is

discussed in detail in Chapter 3, is given by [39]

$$g^{(2)}(\tau) = 1 + |g^{(1)}(\tau)|^2, \tag{5.2}$$

which for a lifetime broadened state gives

$$g^{(2)}(\tau) = 1 + e^{-2\tau/T_{c,1}}. \tag{5.3}$$

The second order coherence time is therefore half the first order coherence time, and is the same as the cavity lifetime, which gives the ringdown timescale. This makes sense when viewed from the perspective that the second order coherence time and ringdown time, both pertain to the intensity of the light, whereas the first order ringdown time pertains to the field. Note that these results are only valid for lifetime broadened i.e. spectrally Lorentzian light. If the cavity has a dispersive medium, then the spectral shape may be different, and these results will not necessarily longer hold.

5.2 Coherence and Ringdown times for Broadband Gain

We model the coupled cavity gain system by using the simple model that the cavity lifetime is extended by the gain. The modified energy decay rate is given by $\kappa_G = \kappa - G$, where κ is the bare cavity energy decay rate and G is the angular gain rate. The gain rate is related to the single pass gain by $G = 2\pi \times sc/L$, where L is the cavity length and s is the single pass gain. This can be trivially rearranged to give the relative cavity decay rate as

$$\frac{\kappa_G}{\kappa} = 1 - \frac{G}{\kappa} \tag{5.4}$$

From the definitions of G and κ, the rate equation for the cavity photon number for this system, assuming negligible absorption from the gain medium, is $\dot{N}_p = G\,(N_p + 1) - \kappa N_p$, where each term represents gain, spontaneous emission from the gain medium and cavity

losses respectively. Note that $G = \kappa$ is the lasing threshold, and this theory is only valid below threshold. Solving this in the steady state gives the cavity photon number as $N_p = \frac{G}{\kappa - G} = \kappa T_G - 1$, where $T_G = 1/\kappa_G$. This can be rearranged to give an expression for T_G in terms of the cavity photon number

$$T_G = T_c \left(N_p + 1 \right) \tag{5.5}$$

where T_c is the bare cavity decay time, $T_c = 1/\kappa$. The fractional increase in the cavity lifetime is therefore just the photon number. The photon number is related to the detected photon count rate by

$$R_p = \eta c T_o N_p / L \tag{5.6}$$

where T_o is the transmission of the cavity output mirror, L is the cavity length and η is the detection efficiency. The cavity photon number, and therefore the expected increase in the cavity lifetime, and then be easily measured. If an average of one photon is in the cavity, this would therefore produce a count rate of approximately 6×10^4 in the HBTI using experimental parameters described in Chapter 2.

In order to test this result, the system of cavity with gain was modelled in QuTiP. The Hamiltonian used was that of a bare cavity in the rotating wave approximation, which is simply 0 when there is no probe or additional fields.

The gain is then introduced by including a collapse operator, $a^\dagger$ with a rate G. This models an incoherent gain in the cavity mode. The cavity decay was modelled by including a collapse operator, a, with a rate κ. The steady state solution to the Lindblad master equation is then found, and the correlation given by Equation 3.1 is calculated for different τ. An exponential curve is then fitted to the correlation to extract the coherence time. The photon number can also be calculated from this simulation by calculating $N_p = \mathrm{Tr}\left(a^\dagger a \rho\right)$. All calculations were done in a basis size of 50. This is a compromise between reducing numerical artefacts caused by the finite basis size while keeping computation time to a usable level. In practice,

solving the density matrix, and calculating the correlation was calculated internally by the QuTiP `correlation_3op_1t()` function. A cavity ringdown simulation was also performed, in order to verify that the second order coherence time is the same as the cavity lifetime. For this measurement, the Hamiltonian was modified to be

$$H = \mu(a + a^\dagger) + \hbar\Delta a^\dagger a, \tag{5.7}$$

where μ is a parameter controlling the strength of the probe and Δ is the probe-cavity detuning. The collapse operators are the same for the $g^{(2)}$ simulation. The steady state density matrix was calculated for $\mu > 0$, and this was used as an initial state for the ringdown measurement. μ was then set to 0, and the state evolved according to the master equation. The expectation value for the photon number was then calculated at various times. A single exponential curve was fitted to the photon number vs time, and the ringdown time constant extracted. The ringdown and coherence time simulations were both performed for different G, and the time constants and number of photons were determined. The results of these simulations are shown in Figure 5.1.

This shows that the second order coherence time and the cavity ringdown time match the expected analytic expression, and are identical to one another in the limit of broad gain linewidth, as expected. The deviation from the analytic expression for large G is caused by the number of cavity photons becoming comparable to the size of the Hilbert space used in the simulation. The photon number and coherence time can both be measured experimentally, so Figure 5.1b can be compared directly to the experiment.

5.3 Second Order Coherence Time Measurement

In order to measure the coherence times of the coupled atom cavity system, the MOT power was reduced to below lasing threshold, and the cavity was locked to the gain peak. The gain was then altered by small amounts by changing the MOT beam power, such that the photon

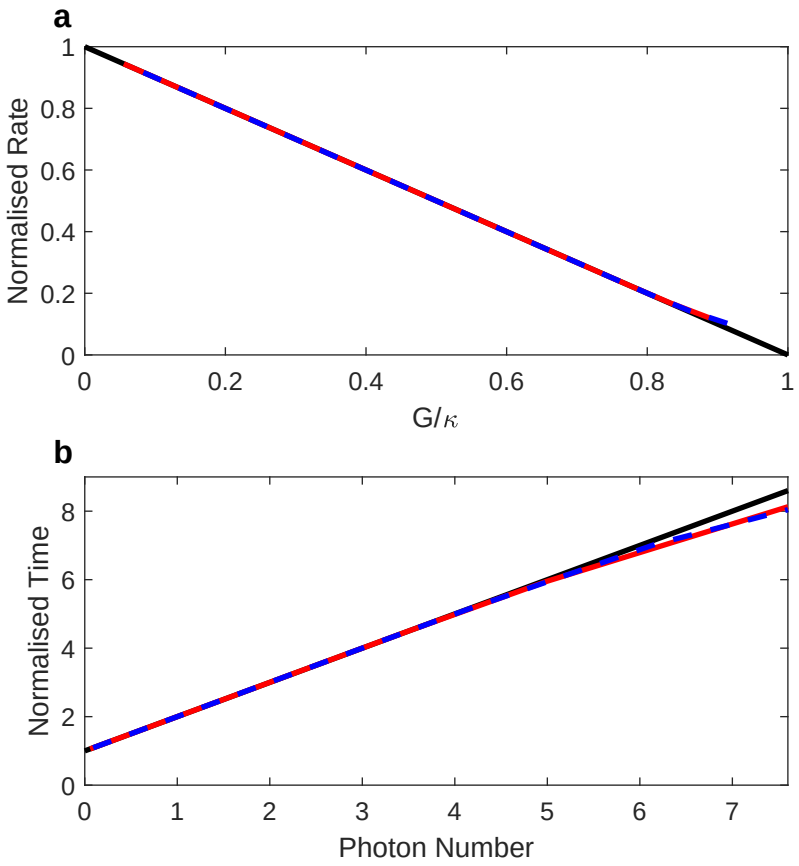

Figure 5.1: **a** shows the simulated cavity ringdown rate (red) and second order coherence decay rate (blue), as a function of the gain rate, G. Both axes are normalised to κ. The black line is the expected analytic relationship. **b** shows the cavity ringdown and coherence times, normalised to the bare cavity ringdown time $1/(2\pi\kappa)$, as a function of the cavity photon number. The colours are the same as in **a**. The numerical result deviates from the expected result as the gain approaches the bare cavity decay rate due to the finite Hilbert space used in the numerical calculation.

count rate ranged between approximately 5×10^3 and 4×10^4 s^{-1} on the HBTI. Data were taken for several minutes for each value of gain. Data were taken for longer for low gain, as the count rate was lower, requiring more photon counts and therefore a longer time to get the same number of coincidence counts. The coherence times were then calculated for each value of gain, in an identical way to in Chapter 3. The average photon count rate across both detectors was also calculated. The coherence time was then plotted against the count rate, to give an experimental version of Figure 5.1b. This method gives Figure 5.2.

The resultant figure shows a clear positive correlation, which is predicted from theory, but the noise on the data is only slightly less than the signal and cannot be fitted well to Equation 5.5. This is because the photon number diverges as G tends to κ, which means any small noise on the gain has a large effect on the photon number when close to threshold. In addition to this, the second order coherence time measurement is dependent on the coincidence count rate, which scales as ${N_p}^2$, whereas the average count rate scales with N_p. This means that for each data point, the coherence time measurement is dominated by times where the photon count rate is at its highest, rather than the average count rate.

In order to reduce the effects of this intensity noise, further post-processing was done on the data. A series of photon timestamps several minutes long was subdivided into regions of 1 ms. This time was chosen as it is longer than the average count rate, without being longer than the timescale of the count rate variation. Each region was further subdivided into 100 subregions. In each subregion a $g^{(2)}(\tau)$ curve was produced, which were averaged across the entire region. The mean count rate was also measured for each region. This was done for the whole data file. Each region was then binned according to the count rate, and the $g^{(2)}(\tau)$ curves for regions in the same bin were averaged. This method effectively uses the natural variation in gain to produce the different count rates, rather than changing the gain explicitly via the MOT beam power. However, the MOT beam power can still be changed to explore different regimes. This is shown in Figure 5.3, with two different MOT beam powers. Note that the detection efficiency was optimised between taking the data represented in Figures

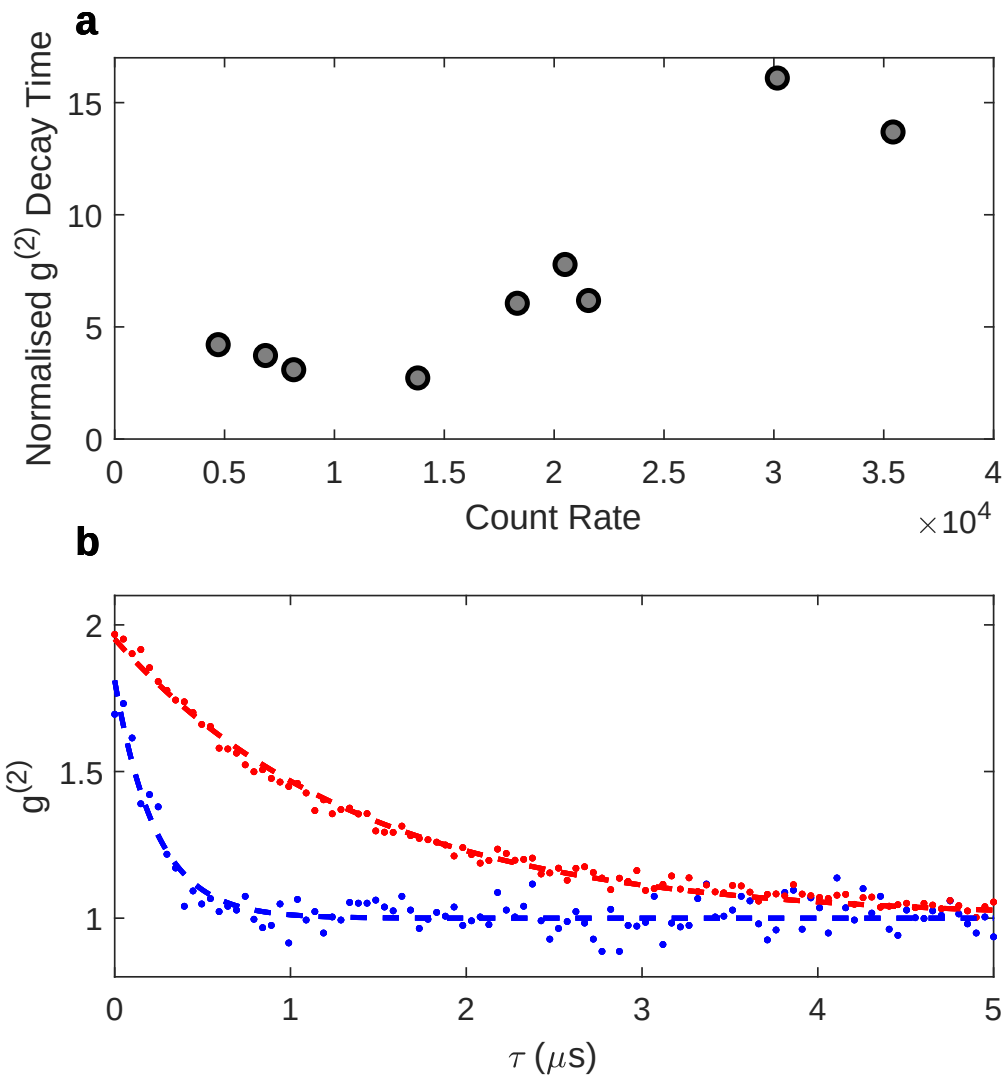

Figure 5.2: **a** shows the normalised second order coherence time vs mean photon count rate. The coherence time is normalised to the bare cavity coherence time, $T_c = 1/(2\pi \times 1.8)$ μs. Each point is calculated from several minutes of photon counts, with different MOT beam powers. **b** shows two examples of the $g^{(2)}$ measurements. Dotted lines show fits to the data used to make **a**. The red and blue data corresponds to the points with the maximum and minimum decay time in **a** respectively.

5.2 and 5.3, so the count rates are not directly comparable.

This method can be seen to significantly reduce the effects of the noise. Both panels show that the decay time is linear with respect to the count rate as expected. In both subfigures the system is below threshold and so the single pass gain is less than the cavity loss of 0.37%. In **b** the second order coherence time is increased by a factor of 100. The second order coherence time is therefore highly sensitive to changes in single pass gain on the order of 0.1%, demonstrating the potential for this system to detect very small gains. Figure 5.3**a** demonstrates the non-zero intercept, which in Equation 5.5 corresponds to the bare cavity coherence time. The fit to the data gives $(1.6 \pm 0.1)T_c$ as the zero count rate decay time, which is significantly longer than the expected value of T_c. The y-intercept of the fit in Figure 5.3b is $(2 \pm 3)T_c$, which is consistent with the intercept measured in **a**. The fitted lines have gradients of $2.4 \pm 0.1 \times 10^{-5}$ s and $6.1 \pm 0.3 \times 10^{-5}$ s, which are significantly different from each other, and significantly larger than the predicted gradient of 1.7×10^{-5} calculated from Equation 5.6.

One possibility for the deviation from the expected result is that the atoms from the MOT are having an effect on the system other than providing gain. It is expected that the main source of variation in the count rate is due to noise on the MOT beams on a timescale of $\sim$ 1ms, as in Figure 3.7b. In this case, the atom number is approximately constant, meaning each point in each panel of Figure 5.3 has the same atom number. The extrapolation to zero count rate therefore does not represent zero net gain from the atoms, as the atoms will contribute some absorption. This absorption also affects the count rate, as the count rate is dependent on the balance of gain and absorption, not only the net gain. Another possible explanation for the discrepancy from theory is that dispersion from the atoms is creating a group index of less than one, which would act to increase the cavity decay time and possibly the second order coherence time [66]. A third possibility is that the presence of the atoms spatially modifies the cavity mode, reducing the detection efficiency of the HBTI. However, this is considered unlikely, as the efficiency would have to be reduced by a factor of around

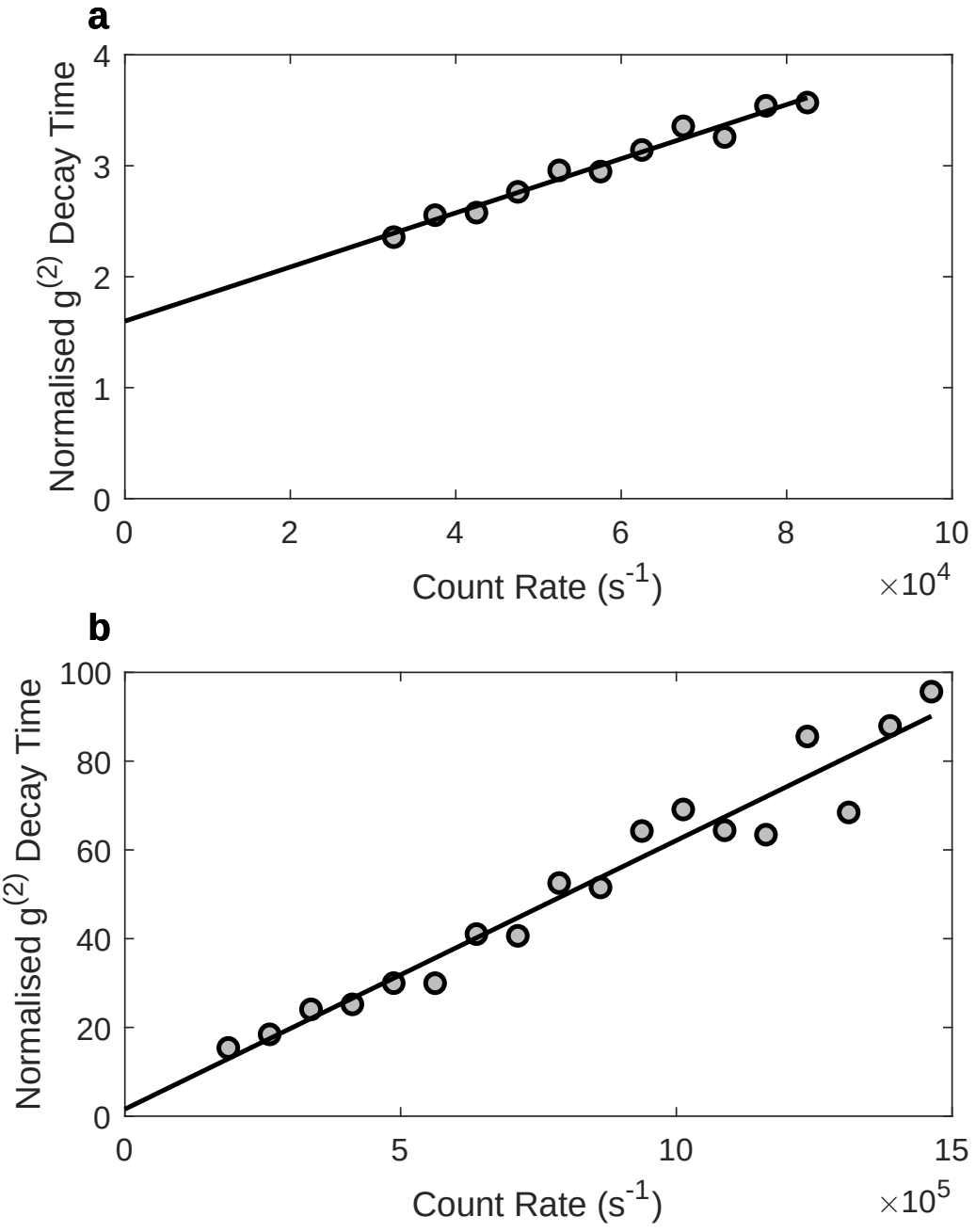

Figure 5.3: Normalised second order coherence time vs count rate after binning according to the count rate. **a** uses a lower MOT beam power, and therefore a lower count rate, than **b**. Points are experimental data and the black lines are unconstrained linear fits.

4, and no modification of the beam shape was observed on the beam profiler, even for large MOTs.

5.4 Cavity Ringdown measurement

A cavity ringdown measurement of the cavity with gain was also performed in order to compare this method of gain detection to existing methods. To make a ringdown measurement, the probe was locked to be approximately resonant with the gain. The cavity was then locked near the probe, and the lock was slowly adjusted to maximise the ringdown time. The probe lock frequency was then adjusted in order to maximise the probe transmission. The ringdown time was relatively insensitive to the adjustment of the probe frequency, but was highly sensitive to the cavity frequency, which was why this method of adjustment was chosen. The probe beam was then abruptly switched off and the power from the cavity mode was measured on the APD. An average of 8192 measurements was used to produce each ringdown trace.

The probe power incident on the cavity was measured to be 20 nW. Assuming perfect mode matching and that the cavity is exactly resonant with the probe, this corresponds to an intensity of approximately 50 $\mathrm{mW/cm^2}$ circulating in the cavity which, for reference, is well above the saturation intensity of the strongest D2 transition which is 1.75 $\mathrm{mW/cm^2}$. The gain feature was therefore saturated, and so the ringdown trace was distorted. In order to fix this, only the tails of the ringdown curve were used to extract the ringdown time constant. The probe power is much lower at these times, so the gain is unsaturated by the probe. The ringdown curves are therefore undistorted at the tails, so a well defined time constant can be found by fitting an exponential to the ringdown curve.

Two measurements were performed using this procedure: The first measurement was taken with the probe and cavity resonant with the gain which should have a longer ringdown time. The second measurement was taken with the probe and cavity approximately 6 MHz red de-

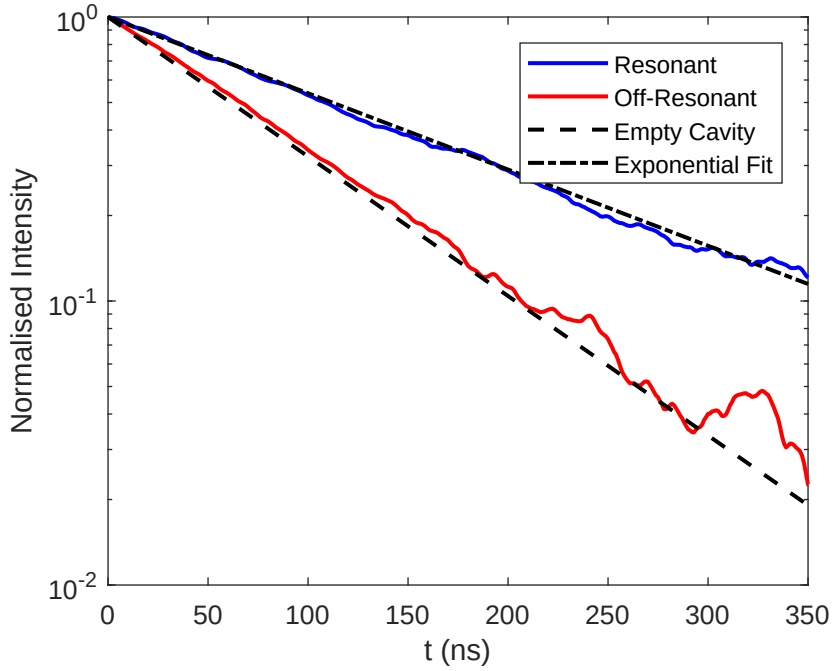

Figure 5.4: The blue curve shows the ringdown curve when the cavity is resonant with the gain. An exponential fit (dashed/dotted line) yields a time constant of 162 ± 1 ns. The red curve is a ringdown measurement where the cavity has been red-detuned by 6.6 MHz. This can be seen to be consistent with the theoretical empty cavity ringdown trace (dashed line) which has a time constant of 88.4 ns.

tuned of the gain peak. The second measurement should have a ringdown time corresponding to the bare cavity lifetime, as the transmission through the MOT is approximately 1 at this frequency. These measurements are shown in Figure 5.4.

The ringdown measurements demonstrate that the gain increased the cavity ringdown time as well as the second order coherence time. Figure 5.4 shows the highest obtained increase of the ringdown time, which is approximately doubled from the empty cavity time, confirming previous results [65], which show that gain can increase the ringdown time, and could be used for spectroscopy of gain. However, the ringdown time is increased by a very small factor when compared to Figure 5.3, where it is increased by a factor of around 100. One reason for this could be that the probe is strong enough to perturb the gain, and therefore limit

the gain rate to approximately $\kappa/2$, which would produces this result. However, this would be surprising as the data shown in Figure 5.4 is taken from the tails of the ringdown curve, where the probe power is very weak. For this to be the cause of discrepancy the saturation effects would therefore have to disappear on a timescale longer than the ringdown time. This timescale is determined by the rate of optical pumping between the ground states caused by the MOT beams. The numerical simulations in Chapter 4 suggest that the pump rate is of the order of 1 MHz, which is slower than the ringdown rate, suggesting that saturation effects could play a role. Future ringdown measurements should therefore use a lower probe power in order to reduce saturation effects. However, this clearly demonstrates the advantage of using the second order coherence time to detect gain as compared to a cavity ringdown technique.

5.5 Conclusion

The second order coherence time has been shown to be increased by the presence of gain. The small gain measured by the second order coherence time demonstrates its potential as a way to measure very small gains. However, post selection of data is currently required to achieve better results than ring-down spectroscopy, where no post selection is performed. In order to measure gain directly using the second order coherence time, the cause of the divergence from the expected result needs to be determined and quantified. This will require work to be done on stabilising the atom number, and finding a method simultaneously independently measuring the gain. Doing this requires either stabilisation of the probe and MOT beam powers, to allow the very small gains to be measured, or alternatively using a lower finesse cavity and an alternative gain medium, in order to use a higher, more easily measured gain.

CHAPTER 6

CONCLUSION AND OUTLOOK

This thesis has described the investigation of a coupled atom-ring cavity system, where the cavity is tuned to be resonant with an atomic gain feature. Chapter 3 demonstrated that the system lases into both directions of the ring cavity. Effects particular to the ring cavity geometry have been demonstrated and investigated for the first time in a cold atom laser, namely directional bistability and non-reciprocity. The gain feature responsible for lasing has been investigated in detail in Chapter 4. The gain mechanism has been shown to be Raman gain between hyperfine ground states, which has never been seen in a MOT operating in the default conditions with no additional beams. This is attributed to the unusual operating conditions of a potassium-39 MOT, which is a consequence of the small hyperfine splitting of potassium-39. Chapter 5 shows the effect of gain on the second order coherence time of the cavity. This has been demonstrated to increase by a factor of 100 with a single pass gain of less than 0.37%, indicating the potential for this method for detecting very weak gain features.

Current work is focused on using two repump beams several MHz detuned from one another to produce a gain doublet. According to the Kramers-Kronig relations, this can lead to group velocities of greater than c in the centre of the doublet, which is termed fast light [69, 70]. The calculated complex susceptibility and group index associated with a gain doublet is shown in Figure 6.1. The gain doublet consists of two Lorentzian gain features

separated by $2\gamma_{Gain}$, where γ_{Gain} is the FWHM linewidth of the gain feature. The group index can be seen to be less than one in the centre of the doublet, where the imaginary part of the susceptibility is negative, indicating gain. This system can therefore be used to produce a fast light laser. The dynamics of the fast light laser could then be studied using this set up.

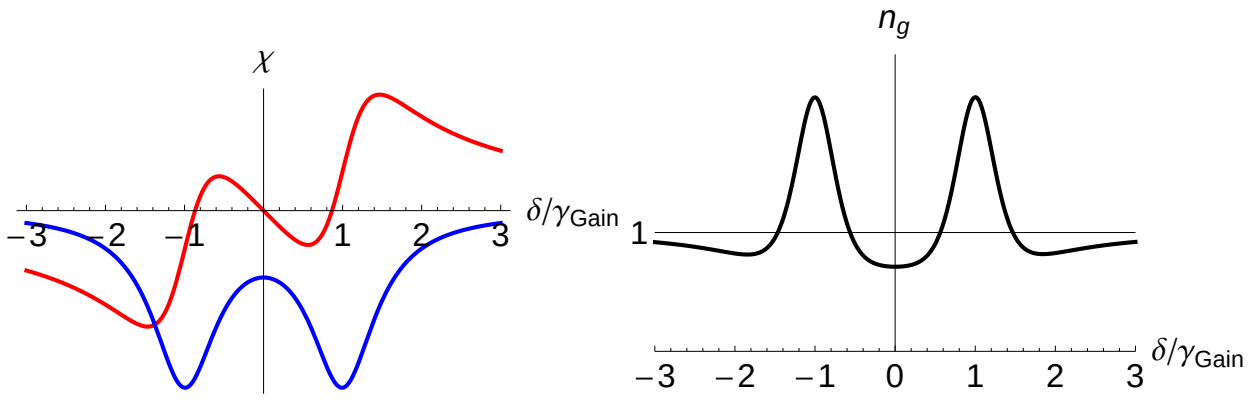

(a) Susceptibility (b) Group index

Figure 6.1: Electric Susceptibility and group index for gain doublet. The real part of the susceptibility is shown in red and the imaginary part is shown in blue. The group index in the centre of the doublet is less than 1, which indicates fast light.

Another possible avenue of future work is to use two far detuned beams to produce the Raman gain doublet, rather than a split repump. This could allow a narrower, more controllable gain feature, which would allow a higher group velocity to be reached in a fast light laser. This fast light laser could be used as an active ring laser gyroscope, where the fast light medium could enhance the sensitivity of the system to rotation by several orders of magnitude [71].

Other possible future work involves further investigating the second order coherence as a method of detecting gain. This work could use a lower finesse cavity, or a more stable gain medium to allow for independent measurement of the gain, which would allow the effects of dispersion and absorption to be studied. This would allow progress to be made towards a workable gain measurement device.

LIST OF REFERENCES

[1] A. L. Schawlow and C. H. Townes. Infrared and optical masers. *Phys. Rev.*, 112:1940–1949, Dec 1958.

[2] T. H. Maiman. Stimulated optical radiation in ruby. *Nature*, 187(4736):493–494, 1960.

[3] Howard M Wiseman. How many principles does it take to change a light bulb... into a laser? *Physica Scripta*, 91(3):033001, feb 2016.

[4] P. P. Sorokin and J. R. Lankard. Stimulated emission observed from an organic dye, chloro-aluminum phthalocyanine. *IBM Journal of Research and Development*, 10(2):162–163, March 1966.

[5] B. H. Soffer and B. B. McFarland. Continuously tunable, narrowband organic dye lasers. *Applied Physics Letters*, 10(10):266–267, 1967.

[6] P. Runge and R. Rosenberg. Unconfined flowing-dye films for cw dye lasers. *IEEE Journal of Quantum Electronics*, 8(12):910–911, December 1972.

[7] F S Ujager, S M H Zaidi, and U Younis. A review of semiconductor lasers for optical communications. In *7th International Symposium on High-capacity Optical Networks and Enabling Technologies*, pages 107–111. IEEE, 2010.

[8] Xuanwei Ong, Min Zhi, Shashank Gupta, and Yinthai Chan. Wet-chemically synthesized colloidal semiconductor nanostructures as optical gain media. *ChemPhysChem*, 17(5):582–597, 2016.

[9] Demetrious T. Kutzke, Owen Wolfe, Simon M. Rochester, Dmitry Budker, Irina Novikova, and Eugeniy E. Mikhailov. Tailorable dispersion in a four-wave mixing laser. *Opt. Lett.*, 42(14):2846–2849, Jul 2017.

[10] J. W. R. Tabosa, G. Chen, Z. Hu, R. B. Lee, and H. J. Kimble. Nonlinear spectroscopy of cold atoms in a spontaneous-force optical trap. *Phys. Rev. Lett.*, 66:3245–3248, Jun 1991.

[11] D Grison, B Lounis, C Salomon, J. Y Courtois, and G Grynberg. Raman spectroscopy of cesium atoms in a laser trap. *Europhysics Letters (EPL)*, 15(2):149–154, may 1991.

[12] B. R. Mollow. Stimulated emission and absorption near resonance for driven systems. *Phys. Rev. A*, 5:2217–2222, May 1972.

[13] F. Y. Wu, S. Ezekiel, M. Ducloy, and B. R. Mollow. Observation of amplification in a strongly driven two-level atomic system at optical frequencies. *Phys. Rev. Lett.*, 38:1077–1080, May 1977.

[14] L Hilico, C Fabre, and E Giacobino. Operation of a "cold-atom laser" in a magneto-optical trap. *Europhysics Letters (EPL)*, 18(8):685–688, apr 1992.

[15] William Guerin, Franck Michaud, and Robin Kaiser. Mechanisms for lasing with cold atoms as the gain medium. *Phys. Rev. Lett.*, 101:093002, Aug 2008.

[16] Hannes Gothe, Dmitriy Sholokhov, Anna Breunig, Martin Steinel, and Jürgen Eschner. Continuous-wave virtual-state lasing from cold ytterbium atoms. *Phys. Rev. A*, 99:013415, Jan 2019.

[17] Q. Baudouin, N. Mercadier, V. Guarrera, W. Guerin, and R. Kaiser. A cold-atom random laser. *Nature Physics*, 9:357 EP –, May 2013.

[18] Justin G. Bohnet, Zilong Chen, Joshua M. Weiner, Dominic Meiser, Murray J. Holland, and James K. Thompson. A steady-state superradiant laser with less than one intracavity photon. *Nature*, 484:78 EP –, Apr 2012.

[19] Geert Vrijsen, Onur Hosten, Jongmin Lee, Simon Bernon, and Mark A. Kasevich. Raman lasing with a cold atom gain medium in a high-finesse optical cavity. *Phys. Rev. Lett.*, 107:063904, Aug 2011.

[20] D. Kruse, C. von Cube, C. Zimmermann, and Ph. W. Courteille. Observation of lasing mediated by collective atomic recoil. *Phys. Rev. Lett.*, 91:183601, Oct 2003.

[21] Rajarshi Roy and L. Mandel. Optical bistability and first order phase transition in a ring dye laser. *Optics Communications*, 34(1):133 – 136, 1980.

[22] Nikolai V Kravtsov and N N Kravtsov. Nonreciprocal effects in ring lasers. *Quantum Electronics*, 29(5):378, 1999.

[23] W. W. Chow, J. Gea-Banacloche, L. M. Pedrotti, V. E. Sanders, W. Schleich, and M. O. Scully. The ring laser gyro. *Rev. Mod. Phys.*, 57:61–104, Jan 1985.

[24] S Merlo, M Norgia, and S Donati. *Fibre Gyroscope Principles*. John Wiley & Sons Ltd, 2002.

[25] M. S. Shahriar, G. S. Pati, R. Tripathi, V. Gopal, M. Messall, and K. Salit. Ultrahigh enhancement in absolute and relative rotation sensing using fast and slow light. *Phys. Rev. A*, 75:053807, May 2007.

[26] David D. Smith, Hongrok Chang, L. Arissian, and J. C. Diels. Dispersion-enhanced laser gyroscope. *Phys. Rev. A*, 78:053824, Nov 2008.

[27] R Culver, A Lampis, B Megyeri, K Pahwa, L Mudarikwa, M Holynski, Ph W Courteille, and J Goldwin. Collective strong coupling of cold potassium atoms in a ring cavity. *New Journal of Physics*, 18(11):113043, 2016.

[28] Balazs Megyeri. *A cold atom ring laser*. PhD thesis, University of Birmingham, 2019.

[29] Andreas Lampis. *Coherent light-matter interactions with potassium atoms*. PhD thesis, University of Birmingham, 2018.

[30] Robert Culver. *Collective strong coupling of cold potassium atoms in an optical ring cavity*. PhD thesis, University of Birmingham, 2017.

[31] Lawrence Mudarikwa. *Cold atoms in a ring cavity*. PhD thesis, University of Birmingham, 2015.

[32] Komal Pahwa. *Magneto optical trapping of potassium-39 in a ring cavity*. PhD thesis, University of Birmingham, 2014.

[33] Oleg Chubar, Pascal Elleaume, and Joel Chavanne. A three-dimensional magnetostatics computer code for insertion devices. *Journal of Synchrotron Radiation*, 5(3):481–484, May 1998.

[34] G. Ritt, G. Cennini, C. Geckeler, and M. Weitz. Laser frequency offset locking using a side of filter technique. *Applied Physics B*, 79(3):363–365, Aug 2004.

[35] Hua Luo, Kai Li, Dongfang Zhang, Tianyou Gao, and Kaijun Jiang. Multiple side-band generation for two-frequency components injected into a tapered amplifier. *Opt. Lett.*, 38(7):1161–1163, Apr 2013.

[36] Andreas Lampis, Robert Culver, Balázs Megyeri, and Jon Goldwin. Coherent control of group index and magneto-optical anisotropy in a multilevel atomic vapor. *Opt. Express*, 24(14):15494–15505, Jul 2016.

[37] Simin Feng and Herbert G. Winful. Physical origin of the gouy phase shift. *Opt. Lett.*, 26(8):485–487, Apr 2001.

[38] B. Megyeri, G. Harvie, A. Lampis, and J. Goldwin. Directional bistability and nonreciprocal lasing with cold atoms in a ring cavity. *Phys. Rev. Lett.*, 121:163603, Oct 2018.

[39] Christopher Gerry and Peter Knight. *Quantum coherence functions*, page 115134. Cambridge University Press, 2004.

[40] Marlan O. Scully and M. Suhail Zubairy. *Quantum theory of the laser density operator approach*, page 327361. Cambridge University Press, 1997.

[41] J. McKeever, A. Boca, A. D. Boozer, J. R. Buck, and H. J. Kimble. Experimental realization of a one-atom laser in the regime of strong coupling. *Nature*, 425:268 EP –, Sep 2003.

[42] Andreas Steffen, Wolfgang Alt, Maximilian Genske, Dieter Meschede, Carsten Robens, and Andrea Alberti. Note: In situ measurement of vacuum window birefringence by atomic spectroscopy. *Review of Scientific Instruments*, 84(12):126103, 2013.

[43] Surendra Singh and L. Mandel. Mode competition in a homogeneously broadened ring laser. *Phys. Rev. A*, 20:2459–2463, Dec 1979.

[44] Murray Sargent. *Laser physics / Murray Sargent III, Marlan O. Scully, Willis E. Lamb, Jr.* Addison-Wesley, Reading, Mass. ; London (etc.), 1974.

[45] P. Lett and L. Mandel. Investigation of time-dependent correlation properties of the bidirectional dye ring laser. *J. Opt. Soc. Am. B*, 2(10):1615–1625, Oct 1985.

[46] H. A. Haus. Mode-locking of lasers. *IEEE Journal of Selected Topics in Quantum Electronics*, 6(6):1173–1185, Nov 2000.

[47] S. Beri, L. Gelens, M. Mestre, G. Van der Sande, G. Verschaffelt, A. Scirè, G. Mezosi, M. Sorel, and J. Danckaert. Topological insight into the non-arrhenius mode hopping of semiconductor ring lasers. *Phys. Rev. Lett.*, 101:093903, Aug 2008.

[48] Guy Van der Sande, Lendert Gelens, Philippe Tassin, Alessandro Scir, and Jan Danckaert. Two-dimensional phase-space analysis and bifurcation study of the dynamical behaviour of a semiconductor ring laser. *Journal of Physics B Atomic Molecular and Optical Physics*, 41:095402, 04 2008.

[49] Nikolai V Kravtsov and O E Naniĭ. High-stability single-frequency solid-state lasers. *Quantum Electronics*, 23(4):272–291, apr 1993.

[50] Bao Cheng Yu Jiang Yanan and Liu Weimin. A non-reciprocal optical effect in optical gyroscope. *Optica Applicata*, 14:217–230, 1984.

[51] Takuro Ideguchi, Tasuku Nakamura, Yohei Kobayashi, and Keisuke Goda. Kerr-lens mode-locked bidirectional dual-comb ring laser for broadband dual-comb spectroscopy. *Optica*, 3(7):748–753, Jul 2016.

[52] F. Y. Wu, S. Ezekiel, M. Ducloy, and B. R. Mollow. Observation of amplification in a strongly driven two-level atomic system at optical frequencies. *Phys. Rev. Lett.*, 38:1077–1080, May 1977.

[53] Masaharu Mitsunaga, Tetsuya Mukai, Kimitaka Watanabe, and Takaaki Mukai. Dressed-atom spectroscopy of cold cs atoms. *J. Opt. Soc. Am. B*, 13(12):2696–2700, Dec 1996.

[54] Rahul Sawant and S. A. Rangwala. Lasing by driven atoms-cavity system in collective strong coupling regime. *Scientific Reports*, 7(1):11432, 2017.

[55] Graeme Harvie, Adam Butcher, and Jon Goldwin. In situ raman gain between hyperfine ground states in a potassium magneto-optical trap. *Phys. Rev. A*, 100:033408, Sep 2019.

[56] Bich Ha Nguyen. Lamb and ac stark shifts in cavity quantum electrodynamics. *Advances in Natural Sciences: Nanoscience and Nanotechnology*, 1(3):035008, nov 2010.

[57] T.G. Tieke. Propterties of potassium v1.02. Available online at http://www.tobiastiecke.nl/archive/PotassiumProperties.pdf, 2011.

[58] Daniel A. Steck. Rubidium 85 D line Data. Available online at http://steck.us/alkalidata (Revision 2.1.4), December 2010.

[59] O. S. Mishina, M. Scherman, P. Lombardi, J. Ortalo, D. Felinto, A. S. Sheremet, A. Bramati, D. V. Kupriyanov, J. Laurat, and E. Giacobino. Electromagnetically induced transparency in an inhomogeneously broadened Λ transition with multiple excited levels. *Phys. Rev. A*, 83:053809, May 2011.

[60] A Lipsich, S Barreiro, Alexander Akulshin, and A Lezama. Absorption spectra of driven degenerate two-level atomic systems. *Physical Review A*, 61:53803–, 05 2000.

[61] Qutip function library. `http://qutip.org/docs/3.1.0/apidoc/functions.html#qutip.correlation.spectrum_ss`. Accessed: 2019-07-09.

[62] M. Lax and W. Louisell. Quantum noise ix: Quantum fokker-planck solution for laser noise. *IEEE Journal of Quantum Electronics*, 3(2):47–58, February 1967.

[63] F. Davidson and L. Mandel. Correlation measurements of laser beam fluctuations near threshold. *Physics Letters A*, 25(9):700 – 701, 1967.

[64] Florian V. Englich, Yabai He, and Brian J. Orr. Stimulated-raman-gain cavity-ringdown spectroscopy for high-resolution gas sensing. In *Conference on Lasers and Electro-Optics/Quantum Electronics and Laser Science and Photonic Applications Systems Technologies*, page CTuY3. Optical Society of America, 2005.

[65] Susana Silva, Regina Magalhães, Rosa Ana Pérez-Herrera, Manuel Lopez-Amo, M. B. Marques, and O. Frazão. Fiber cavity ring down and gain amplification effect. *Photonic Sensors*, 6(4):324–327, Dec 2016.

[66] T. Lauprêtre, C. Proux, R. Ghosh, S. Schwartz, F. Goldfarb, and F. Bretenaker. Photon lifetime in a cavity containing a slow-light medium. *Opt. Lett.*, 36(9):1551–1553, May 2011.

[67] T Lauprêtre, S Schwartz, R Ghosh, I Carusotto, F Goldfarb, and F Bretenaker. Anomalous ring-down effects and breakdown of the decay rate concept in optical cavities with negative group delay. *New Journal of Physics*, 14(4):043012, apr 2012.

[68] R. Loudon. *The Quantum Theory of Light*. Clarendon Press, 1983.

[69] Aephraim M. Steinberg and Raymond Y. Chiao. Dispersionless, highly superluminal propagation in a medium with a gain doublet. *Phys. Rev. A*, 49:2071–2075, Mar 1994.

[70] L. J. Wang, A. Kuzmich, and A. Dogariu. Gain-assisted superluminal light propagation. *Nature*, 406(6793):277–279, 2000.

[71] H. N. Yum, M. Salit, J. Yablon, K. Salit, Y. Wang, and M. S. Shahriar. Superluminal ring laser for hypersensitive sensing. *Opt. Express*, 18(17):17658–17665, Aug 2010.